©Copyright 2026
Pattarapon Moonkaen

Development and Application of Diffusion Monte Carlo Methods to Study Molecular Vibrations

Pattarapon Moonkaen

A dissertation
submitted in partial fulfillment of the
requirements for the degree of

Doctor of Philosophy

University of Washington

2026

Reading Committee:

Anne McCoy, Chair

Stefan Stoll

Sotiris Xantheas

Program Authorized to Offer Degree:

Chemistry

University of Washington

Abstract

Development and Application of Diffusion Monte Carlo Methods to Study Molecular Vibrations

Pattarapon Moonkaen

Chair of the Supervisory Committee:
Professor Anne McCoy
Chemistry

Understanding the vibrational structure of molecules that exhibit large-amplitude motion remains a central challenge in theoretical spectroscopy. In such systems, the vibrational wave function is often highly delocalized, the harmonic approximation breaks down, and strong coupling among vibrational coordinates complicates both the calculation and the interpretation of the results. These challenges are especially pronounced in fluxional molecular ions such as $C_2H_5^+$ and CH_5^+, where anharmonicity, isotopic substitution, and hydrogen scrambling strongly influence the observed spectra. This dissertation uses diffusion Monte Carlo (DMC) to address these challenges, while also extending the methodology so that it can provide broader access to excited-state properties and spectroscopic observables.

To begin, the theoretical foundations of diffusion Monte Carlo and several of its extensions are reviewed, including guided DMC, fixed-node approaches for excited states, rigid-body formulations, and treatments involving multiple potential energy surfaces. Particular attention is given to the theory and its connection to the algorithm.

The first application focuses on the ethyl cation, $H^+(C_2H_4)$, and its deuterated analogues. DMC calculations show that the ground-state wave function is localized near the nonclassical bridged structure where the proton is equidistant from the two carbon atoms, although the motion of the bridging proton remains large in amplitude. Fixed-node DMC calculations of

excited states are used to examine effects of isotopic substitution on the proton-transfer and CH stretching vibrations, clarifying how deuteration changes both the vibrational frequencies and the extent of delocalization associated with the bridging proton.

The second part of this work develops approaches for evaluating infrared intensities within the guided DMC framework. Trial-wave-function and descendant-weighting approaches are developed for calculating transition dipole matrix elements and are applied to model systems, water, $H_3O_2^-$, and $H_5O_2^+$. These calculations show that trial-wave-function approaches provide useful lower-cost approximations while keeping the accuracy of the descendant-weighting approach and help reveal how vibrational couplings are reflected in transition intensities.

The third part presents a guided DMC formulation in internal coordinates for ground and excited vibrational states. This approach extends DMC to coordinate representations that more directly reflect the underlying nuclear motion and is designed for cases in which the coordinate dependence of the effective masses can be treated locally. Applications to water show good agreement with Cartesian-coordinate DMC and converged variational calculations, while also demonstrating that the method can be applied to excited states whose nodal surfaces are not determined by symmetry.

The final application addresses the CH stretching spectra of CH_5^+ and CH_4D^+, systems whose flat potential energy surfaces and highly delocalized ground-state wave functions have made their spectra difficult to interpret. Structures sampled from the DMC ground-state probability density are used together with reduced spectral models to describe the CH stretching region. These calculations reproduce the main features of the reported spectra and suggest that isomerization of CH_5^+ is more restricted in helium droplets than in the gas phase.

Taken together, the results presented in this dissertation demonstrate that diffusion Monte Carlo can serve not only as a tool for evaluating vibrational energies and wave functions, but also as a flexible framework for probing excited states, transition intensities, and

the spectroscopic consequences of fluxional motion. By combining methodological development with applications to challenging molecular ions, this work expands the scope of DMC for vibrational spectroscopy and provides new insight into how anharmonicity, delocalization, and isotopic substitution shape molecular structure and spectra.

TABLE OF CONTENTS

LIST OF FIGURES

LIST OF TABLES

ACKNOWLEDGMENTS

Pursuing a Ph.D. is no easy feat, and along the way I have been fortunate to receive support from many people whom I would like to acknowledge.

First, I would like to thank my advisor, Dr. Anne McCoy. This thesis, and my Ph.D. journey as a whole, would not have been possible without you. Thank you for always seeming to know exactly how to deal with a 'lazy' person like me and for guiding me through not only academic challenges, but life in general as well. You have inspired me to always try to do my best in everything I do, and I will carry that with me moving forward. I would also like to thank my committee members, Dr. Sotiris Xantheas, Dr. Stefan Stoll, and Dr. Ting Cao for their advice and support over the past few years.

I would also like to thank the members of the McCoy group for always being there for me, especially when I could not figure out what was wrong with my code. In particular, I would like to thank Dr. Ryan DiRisio, Dr. Mark Boyer, Dr. Rachel Huchmala, and Dr. Jacob Finney for being mentors during the first few years of my Ph.D. I would also like to thank Yarra Hassan, Greta Jacobson, Chenrui Shao, and Amanda Nilsen for all of the support, the fun times, and the serious times we shared over the years. I would also like to thank Michael Rosen, Dan Lotan, Andrew Webb, Raghavi Kantharuban, and Tanya Bakalov. I hope you are all enjoying research and not letting it stress you too much. I would also like to thank the Xantheas group, especially Dr. Garrett Santis and Madisen Hallsten. I wish you all the best in whatever comes next.

I would like to thank my family for supporting me throughout this journey. I am especially grateful to my parents, Nipaporn Wachirachai and Theeraphol Moonkaen, who have taught me many important life lessons, especially how to deal with stress during the lowest points

of my Ph.D. I would also like to thank my sister, Pakaporn Moonkaen, who was pursuing her B.Ed. in English and graduating in the same year as me. Thank you for always cheering me up over the years. I would also like to thank my aunt, Montida Wachirachai, who not only helped raise me when I was in primary school, but also always checked in to see how I was doing.

I would also like to thank all of my friends who supported me throughout my Ph.D. I especially want to thank my Thai friends at the University of Washington, including Nonthakit Chaiwong, Sawatdiwat Poonsawat, Teerapat Jenrungrot, Dr. Natchanon Suaysom, Panutad Kuwijitsuwan, and Sirapop Theeranantachai, for all the video game time we shared over the years. Thank you for all the fun times here at UW. All the gaming breaks may not have helped my Ph.D. progress, but I definitely could not have finished it without your support. I also want to thank my lifelong friends, Tanapat Tanadka, Supawit Kittipadakul, and Nanna Solvang. Thank you for checking in on me from time to time and for always being a safe space where I could truly be myself. Lastly, I would like to thank all of the friends I made in Final Fantasy XIV over the past few years. You made my happy days even happier and my difficult days much more bearable.

DEDICATION

to my parents and sister who always believe in me in no matter what I do

Chapter 1

INTRODUCTION

1.1 Fluxional Molecular Ions and Challenges in Vibrational Description

Molecular vibrations provide an important connection between molecular structure, energetics, and spectroscopy. Because vibrational frequencies and intensities are sensitive to bonding, geometry, and intermolecular interactions, vibrational spectroscopy has become one of the most widely used tools for characterizing chemical systems. From a theoretical perspective, calculations of vibrational energies and wave functions make it possible to interpret observed spectra and to understand how nuclear motion reflects the underlying potential energy surface. For many small and relatively rigid molecules, this description can be developed in terms of small displacements about a single equilibrium geometry, and the harmonic approximation provides a useful starting point for understanding the vibrational structure.

This simple picture becomes less effective for systems in which the nuclear motion is strongly anharmonic or extends over multiple regions of configuration space. In such cases, the vibrational wave function can no longer be viewed as localized near a single minimum, and the motion may instead involve large-amplitude rearrangements that connect several energetically accessible structures. The resulting vibrational dynamics are often shaped by strong coupling among coordinates, and the interpretation of the corresponding spectra becomes considerably more difficult. These challenges are especially pronounced in molecular ions and clusters that exhibit fluxional behavior, where the nuclei undergo rearrangements that continuously interconvert among closely related configurations.

Such behavior is exemplified by small carbocations, including the methanium ion, CH_5^+, and the ethyl cation, $C_2H_5^+$. Despite their small size, these systems exhibit highly flux-

ional behavior in which hydrogen atoms undergo rearrangements among energetically similar structures. In the case of CH_5^+,[10–12] the absence of a well-defined equilibrium geometry and the presence of low barriers to hydrogen scrambling lead to a highly delocalized vibrational wave function where each hydrogen can be anywhere around the carbon atom. Similarly, for $C_2H_5^+$,[2,3,13] the motion of the bridging proton has a large amplitude, and vibrational excitation can drive the ion toward structures with more classical character of CH_3^+-CH_2.

These characteristics present significant challenges for both theoretical and experimental studies. From a theoretical perspective, the breakdown of the harmonic approximation and the strong coupling between degrees of freedom require methods that can accurately describe the full-dimensional vibrational problem. At the same time, the choice of coordinate system becomes non-trivial, as different representations may emphasize or obscure the underlying motion. From an experimental standpoint, the interpretation of spectroscopic measurements is complicated by the absence of well-defined vibrational modes and by the broad, often overlapping spectral features that arise from the underlying anharmonic dynamics.

In addition to their intrinsic theoretical interest, these fluxional molecular ions are also of potential relevance in astrochemical contexts. For example, CH_5^+ has long attracted attention because of its possible astrochemical significance, and the interpretation of its spectrum remains an open challenge.[14–16]

Taken together, these considerations highlight the need for computational approaches that can describe highly anharmonic, strongly coupled vibrational motion and provide access to both energies and spectroscopic observables. The development and application of such methods are therefore essential for advancing our understanding of fluxional molecular ions and related systems.

1.2 Computational Methods and Diffusion Monte Carlo

The accurate description of vibrational structure for systems that exhibit strong anharmonicity and undergo large-amplitude motion presents a significant challenge for theoretical methods. A variety of approaches have been developed to address vibrational problems, in-

cluding vibrational perturbation theory (VPT),[17,18] vibrational self-consistent field (VSCF) methods,[19] vibrational configuration interaction (VCI),[20] and discrete variable representation (DVR) techniques.[21] These methods can provide highly accurate results for small systems when the vibrational motion can be described in terms of a well-defined set of coordinates and when the coupling between modes is not too strong. However, their application becomes increasingly difficult as the dimensionality of the system increases or when the vibrational motion involves multiple coupled degrees of freedom.

In particular, for fluxional ions such as CH_5^+ and $C_2H_5^+$, the absence of a single well-defined equilibrium geometry and the presence of large-amplitude motion complicate the construction of an appropriate coordinate system or basis. Methods that rely on expansions about a reference structure or on separable representations of the vibrational wave function may require a large number of basis functions to achieve convergence, making such calculations computationally demanding. In addition, the accurate treatment of highly anharmonic motion and the evaluation of spectroscopic observables, such as transition intensities, further increase the complexity of these approaches.

Diffusion Monte Carlo (DMC)[22–24] provides an alternative framework for solving the vibrational Schrödinger equation that avoids many of these limitations. In DMC, the ground-state wave function is obtained through a stochastic propagation of replicas of the molecules of interest in imaginary time, allowing the method to naturally incorporate anharmonicity and mode coupling without the need for an explicit basis set. As a result, DMC is well-suited for studying high-dimensional systems and for describing delocalized nuclear motion.

1.3 Extensions and Developments in Diffusion Monte Carlo for Vibrational Problems

While diffusion Monte Carlo provides a powerful framework for obtaining ground-state vibrational energies and wave functions, additional developments are required in order to make the method broadly applicable to the study of vibrational structure and spectroscopy. In particular, access to excited states, the evaluation of molecular properties, and the choice

of coordinate representation all play important roles in determining the usefulness of the method for complex molecular systems.

One of the main limitations of DMC is that it is inherently a ground-state method. Several approaches have been developed to extend DMC to the study of excited states, including fixed-node implementations in which the nodal surface of the wave function is imposed as a constraint.[25,26] In these approaches, the accuracy of the resulting excited-state energies depends on the quality of the nodal surface, which is often not known *a priori*. As a result, the construction and validation of appropriate nodal constraints remain important considerations when applying DMC to excited-state problems.

In addition to the calculation of energies, there is a need to evaluate molecular properties that depend explicitly on the vibrational wave function. Techniques such as descendant weighting provide a means of extracting expectation values from DMC simulations and can be used to evaluate quantities such as probability distributions and spectroscopic observables.[24] However, the accuracy of these quantities depends sensitively on the quality of the sampled wave function and on the efficiency with which the relevant regions of configuration space are explored.

Another important aspect of DMC simulations is the choice of coordinate representation. In full-dimensional DMC, the choice of coordinates is generally less critical than in basis set approaches, since the method does not rely on an explicit basis expansion of the wave function. However, the coordinate representation becomes important when one wishes to perform reduced-dimensional calculations or to describe the nuclear motion in a way that more directly reflects the relevant dynamics.[27–29] In such cases, internal coordinates can provide a more physically meaningful description of the motion and offer greater flexibility in the construction of reduced-dimensional Hamiltonians. The development of DMC approaches that operate directly in internal coordinates therefore represents an important step toward extending the method to these types of applications.

The work presented in this thesis addresses several of these challenges. In particular, methods for evaluating infrared intensities within the DMC framework are developed,

providing access to spectroscopic observables beyond vibrational energies. In addition, an internal-coordinate formulation of DMC is introduced to extend the method to calculations in reduced dimensionality and to provide a representation that more directly reflects the underlying motion. These developments are combined with applications to fluxional molecular ions, including $C_2H_5^+$ and CH_5^+, where the interplay between anharmonicity, delocalization, and spectroscopic observables is of central importance.

1.4 Scope and Organization of This Thesis

This thesis focuses on both the development of methods within the diffusion Monte Carlo framework and their application to the study of fluxional molecular ions. The methodological developments are aimed at extending the capabilities of DMC to access spectroscopic observables and to provide more efficient descriptions of nuclear motion in systems that exhibit strong anharmonicity and large-amplitude dynamics. These developments are applied to molecular systems for which such features play a central role, allowing for a detailed investigation of their vibrational structure.

The organization of this thesis is as follows. Chapter 2 provides an overview of the theoretical foundation of diffusion Monte Carlo and summarizes relevant developments from prior work. Chapter 3 presents an application of DMC to the study of the vibrational structure of $C_2H_5^+$, with an emphasis on the effects of deuteration. Chapter 4 introduces a methodology for evaluating infrared intensities within the DMC framework, enabling the calculation of spectroscopic observables beyond vibrational energies. Chapter 5 describes the development of an internal-coordinate formulation of DMC, which is designed to improve the treatment of systems with complex nuclear motion. Finally, Chapter 6 applies these approaches to the study of CH_5^+, providing further insight into the vibrational dynamics and spectroscopic properties of this fluxional molecular ion.

Chapter 2

THEORY AND ALGORITHM OF DIFFUSION MONTE CARLO

This chapter focuses on the diffusion Monte Carlo (DMC) algorithm and its connection to the underlying theory prior to the work of this thesis. While a detailed summary of the theory is provided, aspects such as the choice of parameters, and the advantages and disadvantages of each algorithm are not discussed here. The reader is instead referred to our group's other publications. Most of the algorithms presented here are implemented in PyVibDMC,[30] an open-source Python package developed by our group.

2.1 Unguided DMC

The diffusion Monte Carlo approach[22–24,31–33] is based on the solution to the time-dependent Schrödinger equation

$$i\hbar\frac{\mathrm{d}\Psi}{\mathrm{d}t} = \hat{H}\Psi \tag{2.1}$$

Propagating the solution into the imaginary time by substituting the time variable t with $\tau = it/\hbar$, we obtain the working equation

$$\frac{\mathrm{d}\Psi}{\mathrm{d}\tau} = -\hat{H}\Psi = -(\hat{T} + \hat{V})\Psi \tag{2.2}$$

where $\hat{H}$ is the Hamiltonian operator, $\hat{T}$ is the kinetic energy operator, and $\hat{V}$ is the potential energy operator.

The general solution to Eq. (2.2) is

$$|\Psi(\tau)\rangle = \sum_n c_n(\tau = 0)e^{-E_n\tau}\,|\varphi_n\rangle \tag{2.3}$$

where E_n and $|\varphi_n\rangle$ are the energy and corresponding eigenstates of the Hamiltonian. Shifting the energies by E_{ref}, our simulation parameter,

$$e^{E_{\text{ref}}} |\Psi(\tau)\rangle = \sum_n c_n(\tau = 0) e^{-(E_n - E_{\text{ref}})\tau} |\varphi_n\rangle \tag{2.4}$$

By propagating the wave function in the limit $\tau \to \infty$, we observe that the term $e^{-(E_n - E_{\text{ref}})\tau}$ is dominated by the state with the lowest energy, i.e., the ground state. That is,

$$\lim_{\tau \to \infty} |\Psi(\tau)\rangle \propto c_0(\tau = 0) e^{-(E_0 - E_{\text{ref}})\tau} |\varphi_0\rangle \tag{2.5}$$

We note that if $e^{(E_{\text{ref}} - E_0)\tau} = 1$ then $E_{\text{ref}} = E_0$ and the amplitude of the wave function remains constant. Therefore, we use the requirement that the wave-function amplitude remain constant to determine E_{ref}, which converges to the ground-state energy. This motivates propagating the wave function in imaginary time, as propagating the simulation in imaginary time leads to the ground-state solution.

Representing Eq. (2.2) as a propagator with the shifted energy, we obtain

$$|\Psi(\tau)\rangle = e^{-(\hat{T} + \hat{V} - E_{\text{ref}})} \Psi(0) \tag{2.6}$$

Splitting the propagation into a series of short time steps, $\Delta\tau$, and approximating the propagator by separating the kinetic and potential energy operators, we obtain

$$|\Psi(\tau + \Delta\tau)\rangle \approx e^{-(\hat{V} - E_{\text{ref}})\Delta\tau} e^{-\hat{T}\Delta\tau} |\Psi(\tau)\rangle \tag{2.7}$$

We then represent the wave function as an ensemble of localized functions,

$$\Psi(\mathbf{x}, \tau) = \sum_k W_k(\tau) \text{g}(\mathbf{x} - \mathbf{x}_k) \tag{2.8}$$

where $\mathbf{x}_k$ represents the Cartesian coordinates of the molecular structure in $3N$ dimensions,

where N is the number of atoms. The function $\mathrm{g}(\mathbf{x}-\mathbf{x}_k)$ is a localized function centered at $\mathbf{x}_k$, called a walker, and W_k represents the weight of the k^{th} walker.

To derive the kinetic-energy propagation step, the localized function is represented as a Gaussian with infinitesimal width, giving

$$e^{-\hat{T}\Delta\tau}\mathrm{g}(\mathbf{x}_k) = \left(\prod_{j=1}^{N}\frac{m_j}{2\pi\hbar^2\Delta\tau}\right)^{\frac{3}{2}}\exp\left(-\sum_{j=1}^{N}\frac{m_j\|\vec{x}_j-\vec{x}_{j,k}\|^2}{2\hbar^2\Delta\tau}\right) \tag{2.9}$$

where j indexes the summation over all atoms. This results in a $3N$-dimensional Gaussian function with a width of $\sigma_{j,k}=\sqrt{\hbar^2\Delta\tau/m_{j,k}}$ in each dimension. To maintain the localized form of the walkers, we sample from this Gaussian distribution to update $\mathbf{x}_k$.

The propagation of the potential energy operator results in

$$e^{-(\hat{V}-E_{\text{ref}})\Delta\tau}\mathrm{g}(\mathbf{x}_k) = e^{-(V(\mathbf{x}_k)-E_{\text{ref}})\Delta\tau}\mathrm{g}(\mathbf{x}_k) = C_k\cdot\mathrm{g}(\mathbf{x}_k) \tag{2.10}$$

The result is a scalar multiplier to the weights of the walker, defined here as C_k. There are two ways to incorporate this scalar factor: discrete weighting and continuous weighting.

1. Discrete Weighting: This method assumes that all walkers have equal weights, i.e., $W_k=1$. The scalar multiplier C_k is then used to determine the number of walkers at that position. Specifically, the integer part, $\lfloor C_k\rfloor$, gives the number of walkers placed at $\mathbf{x}_k$, and the fractional part, $C_k-\lfloor C_k\rfloor$, determines the probability of an additional walker at the same position. The advantage of this method is that having equal weights leads to efficient sampling. However, the ensemble size fluctuates.

2. Continuous Weighting: In this method, each walker carries a different weight, and the scalar multiplier is applied directly to the weights,

$$W_k(\tau+\Delta\tau) = C_k\,W_k(\tau). \tag{2.11}$$

However, using this method directly can lead to a situation where most of the total weight is carried by only a few walkers. To address this, we impose an allowed range of weights. If a walker's weight falls outside this range, the walker with the highest weight is duplicated at the same position and both the original walker and the new walker have a weight that is half of its original weight. The walker with the lowest weight is then removed. This procedure is repeated until all walkers fall within the allowed range. While this approach may introduce some numerical instability and require careful consideration of the allowed range of the weights, it keeps the ensemble size constant, which is advantageous for parallelized implementation of the DMC algorithm.

Lastly, at the beginning of the simulation and at the end of each time step, we update E_{ref},[31]

$$E_{\text{ref}}(\tau) = \overline{V}(\tau) - \alpha \frac{\sum_k W_k(\tau) - \sum_k W_k(0)}{\sum_k W_k(0)} \tag{2.12}$$

where $\overline{V}$ is the average potential energy over the walker coordinates, $\sum_k W_k(\tau)$ is the total weight at time τ, and α is a simulation parameter. We find $\alpha = 0.5/\Delta\tau$ to be an effective choice.[34,35] At the beginning of the simulation, the second term is zero, and E_{ref} is simply the average potential energy. The second term ensures that the total weight of the walkers, which represents the amplitude of the wave function, remains approximately constant.

We can obtain several quantities from the DMC simulation. The first is the zero-point energy (ZPE). As discussed above, E_{ref} converges to the ground-state energy when the amplitude of the wave function remains constant. Therefore, the ZPE can be obtained by time-averaging E_{ref} after the ensemble of walkers has equilibrated. We can also obtain the probability amplitude, Ψ^2, as well as expectation values of multiplicative operators, $\langle\Psi|\hat{O}|\Psi\rangle$. To do this, we collect snapshots of the wave function by recording the positions and weights of all walkers. However, since the ensemble of walkers represents Ψ, we require an additional representation of the wave function to obtain Ψ^2. This is done through descendant weighting, which utilizes the fact that the value of the wave function at a walker's geometry is proportional to the sum of the weights of its descendant walkers after propagation for a

specified time. The details of this approach is shown towards the end of the next section.

In summary, the algorithm for simulating DMC can be shown as a pseudo-code below:

```
1. Calculate E_ref in the beginning of the simulation
2. FOR delta_tau from 1 to end
    2.1 Move the walkers (Eq 2.9)
    2.2 Update the weights of the walkers (Eq 2.10,2.11)
    2.3 Add/Remove walkers according to either discrete or continuous weighting
    2.4 Update E_ref (Eq 2.12)
    2.5 Collect data when applicable
```

2.2 Guided DMC

In guided DMC,[36,37] the collection of walkers represents the product of the wave function, Ψ, and a guiding function, ϕ (sometimes called a trial wave function),

$$f(\mathbf{x}) = \Psi(\mathbf{x}, \tau) \cdot \phi(\mathbf{x}) = \sum_k W_k(\tau) \mathrm{g}(\mathbf{x} - \mathbf{x}_k) \tag{2.13}$$

where the trial wave function is a good approximation to the wave function often obtained from the reduced-dimensional calculation. The guiding functions help guide the walkers into the relevant region and reduces the amount of walkers needed for accurate simulations.

Substituting $\Psi = f/\phi$ into the imaginary-time Schrödinger equation (Eq. (2.2)), we obtain

$$\frac{\mathrm{d}f}{\mathrm{d}\tau} = \sum_{j=1}^{N} \left[\frac{\hbar^2}{2m_j} \vec{\nabla}_j^2 - \vec{\nabla}_j \cdot \vec{D}_j(\mathbf{x}) \right] f(\mathbf{x}) - (E_L(\mathbf{x}) - E_{\mathrm{ref}}) f(\mathbf{x}) \tag{2.14}$$

where

$$E_L(\mathbf{x}) = \frac{\hat{H}\phi(\mathbf{x})}{\phi(\mathbf{x})} \tag{2.15}$$

is the local energy, and

$$\vec{D}_j(\mathbf{x}) = \frac{\hbar^2}{m_j} \frac{1}{\phi(\mathbf{x})} \vec{\nabla}_j \phi(\mathbf{x}) \tag{2.16}$$

provides the drift term for the jth atom.

Representing Eq. (2.14) in propagator form, splitting the propagation into a series of time steps with length, $\Delta\tau$, and separating the multiplicative and differential operators, we obtain

$$f(\tau+\Delta\tau) = e^{-(E_L-E_{\mathrm{ref}})\Delta\tau} e^{-\sum_{j=1}^{N}\left[\frac{\hbar^2}{2m_j}\vec{\nabla}_j^2-\vec{\nabla}_j\cdot\vec{D}_j(\mathbf{x})\right]\Delta\tau} f(\tau) \tag{2.17}$$

If the walker is represented by a Gaussian function with infinitesimal width, the first part of the propagator gives

$$e^{-\sum_{j=1}^{N}\left[\frac{\hbar^2}{2m_j}\vec{\nabla}_j^2-\vec{\nabla}_j\cdot\vec{D}_j(\mathbf{x})\right]\Delta\tau}\mathrm{g}(\mathbf{x}_k) = \left(\prod_{j=1}^{N}\frac{m_j}{2\pi\hbar^2\Delta\tau}\right)^{\frac{3}{2}}\exp\left(-\sum_{j=1}^{N}\frac{m_j\|\vec{x}_j-\vec{x}_{j,k}-\vec{D}_j(\mathbf{x}_k)\Delta\tau\|^2}{2\hbar^2\Delta\tau}\right) \tag{2.18}$$

This gives a similar $3N$-dimensional Gaussian function to the unguided DMC, but the center of the Gaussian is shifted by the drift term. Since the drift term depends on the coordinates, the value of the drift term at the beginning and the end of the move is not necessarily the same. This poses a problem because the simulation does not satisfy microscopic reversibility, which should hold in the small-time-step limit.

To solve this problem, we define

$$\mathbf{x}_k' = \mathbf{x}_k + \mathbf{D}_k(\mathbf{x}_k) + \delta_{\mathbf{k}} \tag{2.19}$$

where δ_k is the displacement randomly chosen from the Gaussian distribution, $\mathbf{x}_k$ is the starting geometry, and $\mathbf{x}_k'$ is the geometry after displacement. With this, we can calculate δ_k' from

$$\mathbf{x}_k = \mathbf{x}' + \mathbf{D}_k(\mathbf{x}_k') + \delta_k' \tag{2.20}$$

which is the displacement required to move from $\mathbf{x}'$ to $\mathbf{x}$. From these definitions, we can find

the relative probability of the reverse move to the forward move:

$$P_k = \frac{\mathcal{P}(\mathbf{x}'_k \to \mathbf{x}_k)}{\mathcal{P}(\mathbf{x}_k \to \mathbf{x}'_k)} = \frac{\phi^2(\mathbf{x}'_k)}{\phi^2(\mathbf{x}_k)} \prod_{j=1}^{N} \exp\left[-\left(\left\| \vec{\delta}'_{j,k} \right\|^2 - \left\| \vec{\delta}_{j,k} \right\|^2 \right) / 2\sigma_j^2 \right] \tag{2.21}$$

We see that the probability has two components: the ratio of the amplitudes from the guiding function, and the ratio of the probabilities arising from the Gaussian propagation. We then use this probability to determine whether to accept or reject the move. If the move is rejected, the walker remains at the same position, $\mathbf{x}_k$. Note that P_k can be greater than 1, in which case the move is accepted.[24,36]

The other part of the propagator is

$$e^{-(E_L(\mathbf{x}_k) - E_{\text{ref}})\Delta\tau} \mathrm{g}(\mathbf{x}_k) = C_k \cdot \mathrm{g}(\mathbf{x}_k) \tag{2.22}$$

This is similar to the potential-energy propagation step of the unguided DMC, where the propagator is a scalar. The only difference is that the potential is replaced by the local energy. We can use the same techniques as described in unguided DMC here.

Lastly, E_{ref} is updated in the same way as in unguided DMC, and it still represents the zero-point energy of the system. To obtain the probability amplitude, note that in guided DMC the walkers sample the product, $f(\mathbf{x}) = \Psi(\mathbf{x})\phi(\mathbf{x})$. Therefore, to recover Ψ^2, we need a quantity proportional to Ψ/ϕ. This can be obtained through descendant weighting.[23,24]

To see this, we consider the distribution at $\tau = 0$ localized at a point $\mathbf{x}'$,

$$f_{\mathbf{x}'}(\mathbf{x}, 0) = \Psi(\mathbf{x}, 0)\phi(\mathbf{x}) = \mathrm{g}(\mathbf{x} - \mathbf{x}') \tag{2.23}$$

We expand $\Psi(\mathbf{x}, 0)$ in the eigenstates of the Hamiltonian,

$$\mathrm{g}(\mathbf{x} - \mathbf{x}') = \phi(\mathbf{x}) \sum_n c_n \varphi_n(\mathbf{x}) \tag{2.24}$$

Multiplying both sides by $\varphi_n(\mathbf{x})/\phi(\mathbf{x})$ and integrating over $\mathbf{x}$ gives

$$c_n = \frac{\varphi_n(\mathbf{x}')}{\phi(\mathbf{x}')} \tag{2.25}$$

Propagating to long imaginary time, only the ground-state contribution remains,

$$f_{\mathbf{x}'}(\mathbf{x}, \tau) = c_0\, \phi(\mathbf{x})\varphi_0(\mathbf{x})e^{-(E_0 - E_{\text{ref}})\tau} \tag{2.26}$$

At large τ, since $\Psi = \varphi_0$, we substitute and integrate over $\mathbf{x}$ to obtain

$$P(\mathbf{x}') = \int f_{\mathbf{x}'}(\mathbf{x})\, \mathrm{d}\mathbf{x} = \left(\frac{\Psi(\mathbf{x}')}{\phi(\mathbf{x}')}\right) e^{-(E_0 - E_{\text{ref}})\tau} \langle \phi | \Psi \rangle \tag{2.27}$$

Rearranging this expression, we obtain

$$\frac{\Psi(\mathbf{x}')}{\phi(\mathbf{x}')} \propto P(\mathbf{x}') \tag{2.28}$$

Therefore, the descendant population associated with a walker is proportional to Ψ/ϕ. In practice, this is evaluated by tracking the descendants of each walker over a projection time τ_{DW}, leading to

$$P(\mathbf{x}_j) \propto \frac{w_j(\tau + \tau_{\text{DW}})}{w_j(\tau)} \tag{2.29}$$

where w_j is the weight associated with walker j. This provides an estimator for Ψ/ϕ, and thus allows the reconstruction of Ψ^2.

We note that if the trial wavefunction, ϕ is a constant. The algorithm would be exactly the same as unguided DMC as described in the previous section. We also see that from the derivation of descendant weighting, for the unguided DMC case, the descendant weighting provides an estimator for Ψ which is needed to calculate Ψ^2 in unguided DMC case.

In summary, the algorithm for guided DMC can be shown as a pseudo-code below:

```
1. Calculate E_ref in the beginning of the simulation
```

```
2. FOR delta_tau from 1 to end
    2.1 Calculate the drift term and local energy (Eq. 2.15, 2.16)
    2.2 Diffuse the walkers with the drift term (Eq. 2.18)
    2.3 Calculate the acceptance probability, P_k (Eq. 2.21)
    2.4 Accept or reject the move
    2.5 Update the weights of the walkers using the local energy (Eq. 2.22)
    2.6 Add/Remove walkers according to either discrete or continuous weighting
    2.7 Update E_ref (Eq. 2.12)
    2.8 Collect data when applicable
```

2.3 Rigid-body DMC

In rigid-body DMC,[26,38] one or more of the distances between atoms and a chosen reference point are constrained so that they remain fixed throughout the simulation. This modifies the kinetic energy operator in the Hamiltonian because the constrained atoms no longer undergo translation in Cartesian coordinates. Instead, their motion is described as rotation around the reference point.

The propagation of the wave function follows the same imaginary-time Schrödinger equation and short-time approximation as in Section 2.2 (Eq. (2.2) and Eq. (2.7)). As in unguided DMC, the propagation of the potential energy operator, the update of the walker weights, and the evaluation of E_{ref} remain unchanged. The only modification arises from the kinetic energy propagator, where the Cartesian diffusion described in Eq. 2.9 is replaced by rotational diffusion that preserves the constrained distances.

For a constrained atom j in walker k, its position relative to the reference point is denoted as $\mathbf{r}_{j,k}$, and the constraint is

$$\|\mathbf{r}_{j,k}\| = \text{constant} \tag{2.30}$$

Thus, diffusion in Cartesian space is replaced by rotational motion that preserves $r_{j,k}$. The kinetic energy operator for this constrained motion can be interpreted in terms of rotational

degrees of freedom, with an associated moment of inertia

$$I_{j,k} = m_j \|\mathbf{r}_{j,k}\|^2 \tag{2.31}$$

The short-time propagator for the kinetic energy is then represented by sampling small rotational displacements. For each constrained atom, three angular displacements are sampled,

$$\boldsymbol{\theta}_{j,k} = \begin{pmatrix} \theta_{x,j,k} \\ \theta_{y,j,k} \\ \theta_{z,j,k} \end{pmatrix} \tag{2.32}$$

where each component is sampled from a Gaussian distribution with width

$$\sigma_{\theta,j,k} = \sqrt{\frac{\Delta\tau}{I_{j,k}}} \tag{2.33}$$

These angular displacements define a rotation matrix. In this work, the rotation is constructed as successive rotations about the Cartesian axes,

$$\mathbf{R}_{j,k} = \mathbf{R}_z(\theta_{z,j,k})\mathbf{R}_y(\theta_{y,j,k})\mathbf{R}_x(\theta_{x,j,k}) \tag{2.34}$$

The updated coordinate of the atom is then

$$\mathbf{r}'_{j,k} = \mathbf{R}_{j,k}\mathbf{r}_{j,k} \tag{2.35}$$

Since $\mathbf{R}_{j,k}$ is an orthogonal matrix, this transformation preserves the constraint,

$$\|\mathbf{r}'_{j,k}\| = \|\mathbf{r}_{j,k}\| \tag{2.36}$$

so the distance between the atom and the reference point remains fixed after the move.

This procedure replaces the Cartesian diffusion step in Eq. 2.9 for all constrained atoms.

For unconstrained atoms, the standard Cartesian diffusion is still applied.

In summary, the algorithm for rigid-body DMC is

```
1. Calculate E_ref in the beginning of the simulation
2. FOR delta_tau from 1 to end
    2.1 For each constrained atom, compute I (Eq. 2.31)
    2.2 Sample rotational displacements (Eq. 2.32, 2.33)
    2.3 Construct rotation matrix (Eq. 2.34)
    2.4 Rotate constrained atoms (Eq. 2.35)
    2.5 Diffuse unconstrained atoms (Eq. 2.9)
    2.6 Evaluate the potential energy
    2.7 Update the weights of the walkers (Eq. 2.10, 2.11)
    2.8 Add/Remove walkers according to either discrete or continuous weighting
    2.9 Update E_ref (Eq. 2.12)
    2.10 Collect data when applicable
```

2.4 DMC with multiple potential energy surfaces

Sometimes, the electronic states of the molecules are close to each other that it would be beneficial to include potential energy surfaces for multiple electronic states. For that, we can have DMC is performed on multiple potential energy surfaces,[39,40] and the potential is represented as

$$\hat{V} = \sum_{a,b} |e_a\rangle \, V_{ab} \, \langle e_b| \tag{2.37}$$

With this formulation, we can also represent the wave function for multiple states as

$$|\Psi\rangle = \sum_k \mathrm{g}(\mathbf{x} - \mathbf{x}_k) \begin{pmatrix} W_k^{(1)} \, |\psi_k^{(1)}\rangle \\ W_k^{(2)} \, |\psi_k^{(2)}\rangle \\ \vdots \\ W_k^{(n)} \, |\psi_k^{(n)}\rangle \end{pmatrix} \tag{2.38}$$

where $|\psi_k^{(n)}\rangle = \sum_a c_{k,a}^{(n)} |e_a\rangle$, and $|e_a\rangle$ is a diabatic state corresponding to each potential.

With this new potential and wave function, we propagate the system in imaginary time using the same procedure as in standard DMC (Eq. (2.7)). The propagation of the kinetic energy is unchanged, as it updates the walker positions ($\mathbf{x}_k$) according to Eq. (2.9). The next step is the propagation of the potential, which affects the wave function in two ways: the coefficients $c_{k,a}^{(n)}$ and the weights $W_k^{(n)}$. The change in the coefficients arises from applying the potential operator to each state in the wave function,

$$|\psi_k^{(n)}(\tau + \Delta\tau)\rangle = e^{-\hat{V}\Delta\tau} |\psi_k^{(n)}(\tau)\rangle \tag{2.39}$$

This can be done exactly by first determining the eigenstates of $\hat{V}$, and then converting the wavefunction into the basis constructed from eigenstates of $\hat{V}$. Next, we can apply the operator $e^{-\hat{V}\Delta\tau}$ in this basis which is equivalent to applying $e^{-\lambda_n\Delta\tau}$ to each of the eigenstate with λ_n being the corresponding eigenvalue. Lastly, we convert the wave function back to the $\{|e_a\rangle\}$ basis. However, in previous studies, due to computational limitation, an approximation is used instead. From Eq. (2.39), we can substitute $|\psi_k^{(n)}\rangle = \sum_a c_{k,a}^{(n)} |e_a\rangle$ and approximating the matrix exponential to the first order (since $\Delta\tau$ is small),

$$\sum_a c_{k,a}^{(n)}(\tau + \Delta\tau) |e_a\rangle \approx \left(1 - \Delta\tau \sum_{b,c} |e_b\rangle V_{bc}(\mathbf{x}_k) \langle e_c|\right) \sum_d c_{k,d}^{(n)}(\tau) |e_d\rangle \tag{2.40}$$

which leads to

$$c_{k,a}^{(n)}(\tau + \Delta\tau) = c_{k,a}^{(n)}(\tau) - \Delta\tau \sum_b V_{ab}(\mathbf{x}_k) c_{k,b}^{(n)}(\tau) \tag{2.41}$$

Before considering the contribution of the potential energy propagator to the weights, we need to ensure that the multiple states in the wave function remain orthonormal. This is done using the modified Gram-Schmidt method, where the projection of the lower-energy

states is subtracted from the higher-energy states,

$$\mathbf{c}_k^{(n),\mathrm{UN}}(\tau+\Delta\tau) = \mathbf{c}_k^{(n)}(\tau) - \sum_{m<n} \langle \mathbf{c}_k^{(n)}(\tau), \mathbf{c}_k^{(m)}(\tau)\rangle \, \mathbf{c}_k^{(m)}(\tau) \tag{2.42}$$

This makes the wave functions orthogonal to each other, but they are not normalized, as indicated by the superscript UN. Therefore, we renormalize the wave functions,

$$\mathbf{c}_k^{(n)}(\tau+\Delta\tau) = \mathbf{c}_k^{(n),\mathrm{UN}}(\tau+\Delta\tau)/\|\mathbf{c}_k^{(n),\mathrm{UN}}(\tau+\Delta\tau)\| \tag{2.43}$$

Next, we consider the contribution of the potential energy operator to the weights. This is done through the difference between the expectation value of the potential energy and E_{ref}, similar to standard DMC. The expectation value of the potential is evaluated as

$$V_k^{(n)}(\tau) = \langle \psi_k^{(n)} | \hat{V} | \psi_k^{(n)} \rangle = \sum_{a,b} c_{k,a}^{(n)} c_{k,b}^{(n)} V_{ab}(\mathbf{x}_k) \tag{2.44}$$

This $V_k^{(n)}$ is then used to update the weights in the same way as in unguided DMC,

$$W_k^{(n)}(\tau+\Delta\tau) = e^{-(V_k^{(n)} - E_{\mathrm{ref}}^{(n)})\Delta\tau} \cdot W_k^{(n)}(\tau) \tag{2.45}$$

Now, we must address the issue that a small number of walkers may carry most of the total weight, similar to the unguided case. This can be resolved using the continuous weighting scheme. However, we now need to consider multiple weights corresponding to different states, since all states share the same walker positions. We find that in order to make sure that the walker is not removed if it is significant in at least one of the states, the maximum value of the weights across the states is used to determine whether or not the walker got removed, i.e. we determine whether $\max_n W_k^{(n)}$ is in the allowed range or not.

Lastly, E_{ref} is updated in the same way as in Eq. (2.12). The only difference is that we now have a separate E_{ref} for each state of the wave function.

In summary, the algorithm for DMC with multiple potential energy surfaces can be shown

as a pseudo-code below:

```
1. Calculate E_ref for each state in the beginning of the simulation
2. FOR delta_tau from 1 to end
    2.1 Diffuse the walker positions (Eq. 2.9)
    2.2 Evaluate V[jk] at the new walker position
    2.3 Update the coefficients c[k,a,n] (Eq. 2.41)
    2.4 Orthogonalize the wave functions (Eq. 2.42)
    2.5 Normalize the wave functions (Eq. 2.43)
    2.6 Evaluate the expectation value of the potential, V_bar (Eq. 2.44)
    2.7 Update the weights of the walkers for each state (Eq. 2.45)
    2.8 Add/Remove walkers according to continuous weighting using max W_k
    2.9 Update E_ref for each state (Eq. 2.11)
    2.10 Collect data when applicable
```

2.5 Fixed-node DMC

One of the main drawbacks of the DMC is that it is a ground-state method meaning that we can only obtain ground-state information. However, in order to analyze the vibration of molecules, especially for spectroscopy, it is useful to also obtain excited-state information. One of the ways to obtain excited-states for DMC is to use the fixed-node approach. The idea of fixed-node DMC[25,26,41] is based on the assumption that if the location of the node is known, we can consider the wave function on each side of the node separately. Since Schrödinger's equation is locally satisfied, the ground-state wave functions on each side of the node combine to form the excited-state wave function of the full potential. With this, we can construct a simulation in which the walkers are constrained to remain on one side of the node by raising the potential on the other side of the node, so that all the walkers will be removed if they are in this region.

The main consideration then becomes where to place the node. First, we need to identify

the coordinate, or set of coordinates, that defines the nodal surface. In many cases, this coordinate can be constructed as a linear combination of local-mode coordinates. For example, the asymmetric stretch of water can be described using the difference between the two OH bond lengths. For some modes in the first excited state, we can use symmetry-defined nodes. However, if symmetry cannot be used, we utilize the fact that the zero-point energy on both sides of the node must be the same. This means that the location of the node can be found by trial and error. Alternatively, we can scan the coordinate with a slowly moving node location, under the assumption that the Hamiltonian is slightly perturbed, and the walkers still represent the ground-state solution at each time step. (adiabatic DMC). With this, we can plot the zero-point energy as the node moves, with walkers restricted to either the left or right side, and then use a simple polynomial fit to find the crossing point and the location of the node.

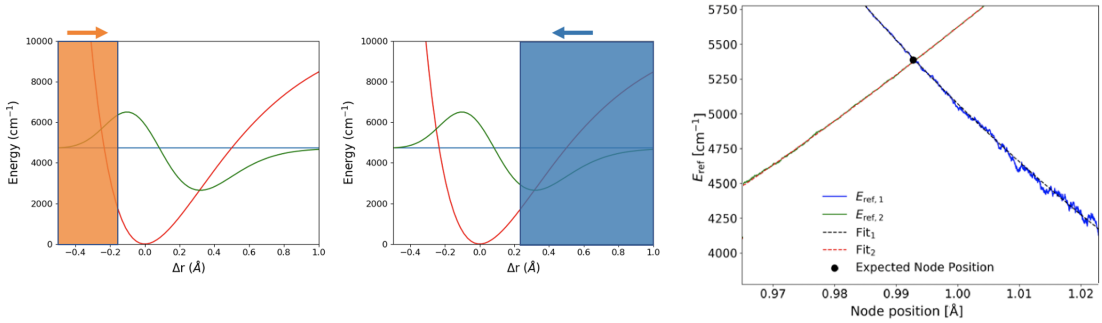

Figure 2.1: Examples of two adiabatic DMC scans to determine the location of the node. The first two plots show the constraint of putting a high potential energy surface on one side of the node and constraint all the walkers on the other side of the node with the direction of movement the position of the node. The third plot shows that plot of the E_{ref} of these two calculations against the location of the node with the fit and expected node position.

The main complication arises from the discrete time step. If a walker is sufficiently close to the node, then within a single time step it may cross into the forbidden region and return, as illustrated in Figure 2.2. In the path outlined by the solid line from A to B, the walker crosses into the forbidden region and then recrosses back within a single time step. Such a

walker should be removed from the simulation because its path enters the forbidden region even when the starting and ending points are in the allowed region. The goal is to determine the probability of such recrossing events.[31]

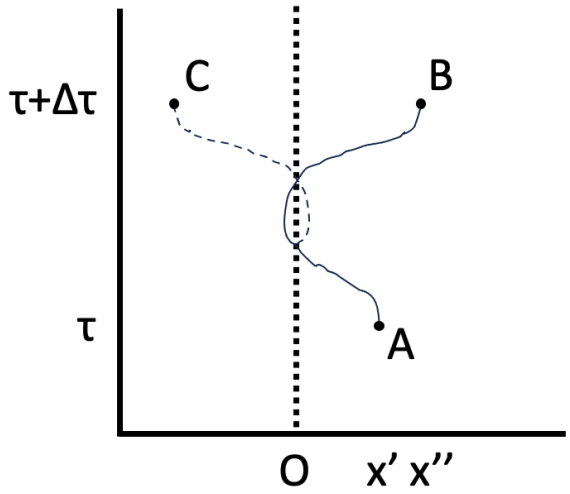

Figure 2.2: Example of a walker path that crosses into the forbidden region and then recrosses within a single time step. Here, O denotes the nodal surface.

First, we calculate the overall probability of the move from A at position x' to B at position x''. This is obtained from the Gaussian distribution derived in Eq. 2.9,

$$\mathcal{P}(\mathrm{A} \to \mathrm{B}) = N \exp\left(-\frac{(x' - x'')^2}{2\sigma^2}\right) \tag{2.46}$$

where N is a normalization factor, and σ is the width of the Gaussian distribution. We then note that if the path recrosses into the forbidden region, we can construct a reflected path from the point of crossing to the end point. Since this path is a reflection, it is equally likely as the original path. For any path that recrosses, we can construct this reflected path with the same probability, and the end point of the reflected path will be point C

(located at $-x''$). The probability for this path is

$$\mathcal{P}(\mathrm{A} \to \mathrm{C}) = N \exp\left(-\frac{(x' + x'')^2}{2\sigma^2}\right) \tag{2.47}$$

Therefore, the probability of recrossing is

$$P_r = \frac{\mathcal{P}(\mathrm{A} \to \mathrm{C})}{\mathcal{P}(\mathrm{A} \to \mathrm{B})} = \exp\left(-\frac{2x'x''}{\sigma^2}\right) \tag{2.48}$$

where $\sigma = \sqrt{\hbar^2 \Delta\tau G}$ and G is the element of Wilson's G-matrix, which represents the inverse mass in the coordinate of interest.

In summary, the algorithm for fixed-node DMC can be shown as a pseudo-code below:

```
1. IF node cannot be determined from symmetry
    1.1 Run two adiabatic DMC simulations where walkers are kept on either side of the
        node, and the node is scanned over a range of values
    1.2 Plot E_ref from both simulations as a function of node position
    1.3 Fit the curves (usually with a low-order polynomial), find the
        intersection, and use it as the node in that coordinate
2. Initialize the walkers on one side of the node
3. Calculate E_ref in the beginning of the simulation
4. FOR delta_tau from 1 to end
    4.1 Diffuse the walkers (Eq. 2.9)
    4.2 Determine whether a walker crosses the node; if so, remove the walker
    4.3 Apply the recrossing correction (Eq. 2.48)
    4.4 Update the weights of the walkers (Eq. 2.10)
    4.5 Add/Remove walkers according to either discrete or continuous weighting
    4.6 Update E_ref (Eq. 2.11)
    4.7 Collect data when applicable
```

Chapter 3

ISOTOPE EFFECTS ON GROUND AND EXCITED STATES OF ETHYL CATION, $H^+(C_2H_4)$

Reproduced in part with permission from [Pattarapon Moonkaen, Jacob M. Finney, and Anne B. McCoy. Isotope Effects on Ground and Excited States of Ethyl Cation, $H^+(C_2H_4)$. *J. Phys. Chem. A* **2023** , 127 (5), 1196-1205]. Copyright [2023] American Chemical Society.

3.1 Introduction

Carbocations have been of considerable interest due to their high acidity, importance as intermediates in solution phase chemistry, and in chemistry in extreme environments.[42] More fundamentally, carbocations present a class of molecular ions that exhibit non-classical bonding arrangements, for example, two-centered three-electron bonds.[43] Such bonding environments often result in low barriers for hydrogen scrambling. This can lead to complicated tunneling pathways, which can make the interpretation of the spectra of these ions challenging. An extreme example of such a situation is protonated methane, in which the equilibrium structure resembles a Lewis acid/base complex between CH_3^+ and H_2[43] which will be explored later in this thesis. The low-energy barriers separating the 120 equivalent minima on the potential surface for this ion result in a ground-state wave function that is delocalized among these minima and the transition states that separate the minima.[10–12] The high effective symmetry of $CH_5{}^+$ has made the spectrum of this deceptively simple ion difficult to assign.[44,45] Introducing a second or third carbon atom yields similarly complicated spectra. In the case of protonated acetylene, $H^+(C_2H_2)$, the classical HC-CH_2^+ and proton bridged, non-classical structures both represent minima on the potential.[43,46] As with CH_5^+ proton scrambling in $H^+(C_2H_2)$ is accessible at low temperatures.[47] The minimum-energy structure

of the ethyl cation in the gas phase is also the non-classical structure, while the classical $H_2C\text{-}CH_3^+$ structure is a transition state, which is expected to be at least 7 kcal mol^{-1} higher in energy than the non-classical structure,[13,48] and calculated to be 9.5 kcal mol^{-1} based on the potential used in this study. This contrasts the solution-phase equilibrium structure in which the structure of $H^+(C_2H_4)$ is best described by the classical $H_2C\text{-}CH_3^+$ form. Recent AIMD studies have shown that proton scrambling is also possible for the ethyl cation;[49] however, this process is not likely to affect the low-temperature spectrum.

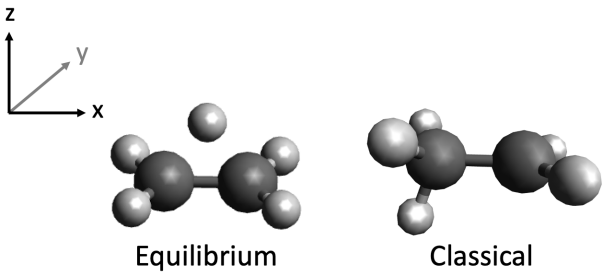

Figure 3.1: (Left) The equilibrium structure and (Right) the classical structures of the ethyl cation. The Cartesian coordinates used in this study are provided in the upper left.

About fifteen years ago, the Dopfer and Duncan groups[2,13] reported spectra of the ethyl cation in a complex with two argon atoms. Analysis of the spectra confirmed that the ion has the non-classical structure shown in Figure 3.1. The spectra, which together span the range from 2000 to 3500 cm^{-1}, are characterized by three high-intensity features, which were assigned to one quantum transitions based on scaled harmonic calculations performed at the MP2/aug-cc-PCVDZ level of theory/basis. The spectrum also contains several weaker features between 2500 and 3000 cm^{-1}, which were recently assigned to transitions to states with two quanta of excitation in the HCH bends and to the state with one quantum of excitation in the two vibrations of the bridging proton in the CH^+C plane. These assignments were made on the basis of a combination of second order vibrational perturbation theory (VPT2) based on MP2/aug-cc-pVTZ calculations, and reduced dimensional calculations.[3] All of these spectral assignments and calculations relied on the premise that the ground

state of the ethyl cation is localized in a single minimum on the potential surface. This is supported by our recently reported ground-state diffusion Monte Carlo study of this ion, which employed a potential surface that was based on electronic energies evaluated at the CCSD(T)/aug-cc-pVTZ level of theory/basis.[50] On the basis of that work, the ground-state wave function is localized in the minimum that corresponds to the non-classical structure shown in Figure 3.1 and there is no evidence of proton scrambling in the ground state. On the other hand, the amplitude of the motion of the bridging proton parallel to the CC bond is large, and extends over nearly the entire region between the two carbon atoms.

In the present study, we explore the nature of vibrationally excited states that are accessed in the reported spectra.[2,13] We also investigate how partial deuteration affects the structures, spectra and the extent of delocalization of the wave function upon vibrational excitation. We concentrate on four isotopologues of the ethyl cation, $H^+(C_2H_4)$, $D^+(C_2D_4)$, $H^+(C_2D_4)$, and $D^+(C_2H_4)$. Of particular interest is the extent to which vibrational excitation to states that are accessed in the spectra drives the ion toward the classical $H_2C\text{-}CH_3^+$ structure. This is a question that can be addressed by fixed-node diffusion Monte Carlo calculations.

In previous studies, we found that partial deuteration can alter the extent of delocalization of the ground-state wave function, as was the case for CH_5^+.[11] In the protonated water dimer, where the excess proton is at the midpoint between the two oxygen atoms of the terminal water molecules, deuterating the central proton leads to a > 100 cm^{-1} red shift of the HOH bend frequency of the outer water molecules.[51–53] These questions will be explored using diffusion Monte Carlo approaches for calculating both the ground- and excited- state wave functions and energies.

3.2 Theory

3.2.1 Overview of Diffusion Monte Carlo

The diffusion Monte Carlo (DMC) approach and our implementation have been described in chapter 2 and also elsewhere,[22–24,31,54] and in this study we use the PyVibDMC[30,54]

implementation of DMC that was recently developed in our group. Below, we summarize the aspects that are important to the present study. The reader is referred to the earlier works for more detailed descriptions of the approach.

Diffusion Monte Carlo is based on using Monte Carlo approaches to model the propagation of an arbitrary wave function, $|\Psi(\tau)\rangle$, in imaginary time, $\tau = it/\hbar$, and noting that the long-time solution to the imaginary-time, time-dependent Schrödinger equation is proportional to the ground-state solution to the Hamiltonian for the system of interest. This arises from the fact that $|\Psi(\tau)\rangle$ can be expanded as a linear superposition of eigenstates of the Hamiltonian of the system of interest, $|\psi_n\rangle$, as

$$|\Psi(\tau)\rangle = \sum_n c_n(\tau = 0) e^{-(E_n - E_{\mathrm{ref}}(\tau))\tau} |\psi_n\rangle \tag{3.1}$$

Since the contributions of each of the states in the summation decay with time as $\exp\left[-\left(E_n - E_{\mathrm{ref}}(\tau)\right)\tau\right]$, at large τ the state with the smallest energy will dominate the expansion in Eq. (3.1). In the simulations, the value of E_{ref} is adjusted so that the amplitude of the wave function remains constant, and in the long τ limit, E_{ref} converges to E_0.

In this work, we employ unguided DMC. In this approach, the wave function is represented by a sum of localized functions,

$$\Psi(\mathbf{x}, \tau) = \sum_i w_i(\tau) g_i(\mathbf{x} - \mathbf{x}_i(\tau)) \tag{3.2}$$

which are represented by $g_i(\mathbf{x} - \mathbf{x}_i(\tau))$. These localized functions will be referred to as walkers in the following discussion. As seen in Eq. (3.2), the walkers are each characterized by the configuration of the molecule, $\mathbf{x}_i(\tau)$, and its weight, $w_i(\tau)$. The weighted density of walkers near a particular molecular geometry provides the amplitude of the wave function at that geometry. While the weights can evolve along with the coordinates of the walkers, here we constrain all of the weights to equal one.

In order to simulate the propagation of the wave function, the walkers diffuse in the Carte-

sian coordinates of the atoms according to the imaginary-time, time-dependent Schrödinger equation,

$$\begin{aligned}\Psi(\mathbf{x},\tau+\Delta\tau) &= \exp[-(H-E_{\text{ref}}(\tau))\Delta\tau]\Psi(\mathbf{x},\tau) \\ &\approx \exp[-(V(\mathbf{x}_i(\tau+\Delta\tau))-E_{\text{ref}}(\tau))\Delta\tau]\exp[-T\Delta\tau]\Psi(\mathbf{x},\tau) \qquad (3.3)\end{aligned}$$

Here, the application of the propagator in the kinetic energy operator to one of the walkers transforms it to a Gaussian distribution function in the $3N$-dimensional space that describes the Cartesian coordinates of the N atoms in the molecule of interest. The standard derivation of this distribution along the coordinates of the jth atom is given by $\hbar\sqrt{\Delta\tau/m_j}$, where m_j is the mass of the jth atom. To maintain the form of the wave function provided by Eq. (3.2), the coordinates of the atoms are displaced by a random amount based on the $3N$-dimensional Gaussian distribution. Likewise, application of the propagator in the potential energy leads the weight of the ith walker to become

$$w_i(\tau+\Delta\tau) = \exp[-(V(\mathbf{x}_i(\tau+\Delta\tau))-E_{\text{ref}}(\tau))\Delta\tau]w_i(\tau) \qquad (3.4)$$

In order to retain the form for the wave function that is provided by Eq. (3.2) where all of the weights are equal to one, the value of $w_i(\tau+\Delta\tau)$ is used to determine the number of walkers at $\mathbf{x}_i(\tau)$ at the start of the next iteration of the propagation. Specifically, the integer part of $w_i(\tau+\Delta\tau)$ provides the number of walkers at this geometry, while the fractional part provides the probability that one additional walker is added at that configuration.[31,54]

Finally, at the start of each time step in the simulation, the value of E_{ref} is updated based on

$$E_{\text{ref}}(\tau) = \overline{V}(\tau) - \alpha\frac{N(\tau)-N(0)}{N(0)} \qquad (3.5)$$

where $\overline{V}$ is the average of the potential energy over the coordinates of the walkers, $N(\tau)$ is

the number of walkers that make up the ensemble at time τ, and α is a simulation parameter. We find $\alpha = 0.5/\Delta\tau$ to be an effective choice for this parameter.[34,35] The second term in Eq. (3.5) ensures that the number of the walkers remains roughly constant throughout the simulation. As noted above, at large τ, E_{ref} converges to the zero-point energy. This allows us to evaluate the zero-point energy by taking the time-averaged value of E_{ref}.

While the zero-point energy can be a useful quantity, of greater interest is the wave function, as it will determine properties of the molecule of interest. In this work, we focus on projections of the probability amplitude onto one or two coordinates, which require a way to obtain Ψ^2 from a wave function of the form provided by Eq. (3.2). Expressed in this way, the ensemble of walkers provides a Monte Carlo sampling based on the wave function and the evaluation of integrals involving Ψ^2 requires a way to evaluate the values of the wave function at the values of $\mathbf{x}_i$ where the walkers are located.[35,54] Following Barnett, Reynolds and Lester,[24] and Suhm and Watts,[23] this is achieved using descendant weighting, in which we exploit the fact that the value of the wave function at the geometry of one of the walkers is proportional to the number of walkers that can be traced to that walker after the simulation has been propagated for a specified amount of time.[54]

3.2.2 Calculation of Excited States Using Fixed-Node DMC

In addition to the ground state, we are also interested in evaluating the energies and wave functions of selected excited states. The excited states of interest in the present study involve one or two quanta of excitation. The normal mode picture of molecular vibrations leads us to expect that the nodal surfaces that describe these excited states can be defined by the value of a coordinate, or the linear combination of coordinates, along which the molecule is being excited.[25,55,56] This approximation for the nodal surface is expected to be rigorous in the limit of low-amplitude vibrations. In studies of several molecules and molecular clusters including $H_5O_2^+$,[57] $H_3O_2^-$,[58] H_5^+[59] and complexes of two neon atoms with SH or OH,[56] all of which contain large amplitude vibrational motions, we showed that the fixed-node approach provides excited-state energies that are in good agreement with the results of

variational calculations. For these studies, the definitions of the nodal surfaces were based on the symmetry of the molecule. In some cases, the shape of the nodal surface was further informed by reduced-dimensional variational calculations.[59,60] As all of the systems where we calibrated the fixed-node approach show comparable or larger amplitude vibrational motions compared to $H^+(C_2H_4)$, we expect the approach will be similarly effective for the present study.

Once the forms of the nodal surfaces have been determined, the next step is to identify the value of this coordinate at which the wave function changes sign. When the vibration that is excited is not totally symmetric, as is the case for the displacement of the excess proton in $H^+(C_2H_4)$ parallel to the CC bond, the value of the coordinate at the node is zero by symmetry. In cases where the position of the node cannot be determined by symmetry, we use the requirement that the zero-point energies evaluated in the nodal regions where the wave function has positive and negative amplitude must be equal.[55] In these cases, the location of the node can be found by trial-and-error, but this is inefficient. Alternatively, the location of the node can be identified by slowly shifting the position of the node throughout the simulation and fitting the value of the zero-point energy as a function of the nodal position to a low-order polynomial. Once this is done for the parts of the wave function with positive and negative amplitude, the location of the node is found by identifying the value of the scanned coordinate at which the energies obtained from the two simulations are equal. We refer to this approach as adiabatic DMC or ADMC, and more complete descriptions of this approach and our implementation can be found elsewhere.[26,32,54]

Once the position of the node is known, DMC simulation are performed that focus on the configurations of the molecule in which the amplitude of the wave function is either positive or negative. Within this region, the part of the excited-state wave function that is being considered resembles a ground state, where the wave function goes to zero at the node with finite slope. Following Anderson,[31] in DMC simulations of excited states the walkers are confined to a single nodal region, and the potential outside this region is replaced by an infinite potential. This process is repeated for all of the nodal regions for the state of

interest. Since the Scrödinger equation is locally satisfied, the ground-state solution to the Schrödinger equation that is based on the modified potential will provide the excited-state solution had the full potential been considered. The above procedure would be sufficient to evaluate excited states in the limit of infinitesimal time steps. When finite time steps are used in numerical simulations, there is a probability that a walker that is on the same side of the nodal surface at the start and end of a time step would have crossed the node and crossed back had a smaller time step been used. This is easily accounted for using the recrossing correction described by Anderson.[31,54]

3.3 Results

In this study, we ran five sets of DMC simulations for the ground, and five sets of DMC simulations for each nodal region of five excited states of ethyl cation and its deuterated analogues. To distinguish the four isotopologues, we use the $X^+(C_2Y_4)$ notation, where X and Y can represent either H or D with X representing the isotope of the bridging proton and Y representing the isotope of the four ethylenic hydrogen atoms. In the discussion that follows, we will use the term hydrogen and proton to represent any isotope, and H or D when we wish to specify the isotope that is being discussed.

At the end of the simulations, we obtain the value of E_{ref} as a function of the propagation time. A plot of this data for a ground-statte simulation of $H^+(C_2H_4)$ is provided in Figure 3.2. As can be seen the value of E_{ref} rises rapidly at short time, and by 1000 a.u. the simulation has stabilized and the value of E_{ref} fluctuates around what appears to be a nearly constant value. After recent analysis of the behaviors of E_{ref} in DMC simulations,[35] we find that allowing 5000 a.u. of equilibration time is sufficient, and all of the reported averaged values of E_{ref} are based on averages starting after 5000 a.u.. We also use descendant weighting, described above, to obtain the probability amplitudes for the states that are studied.

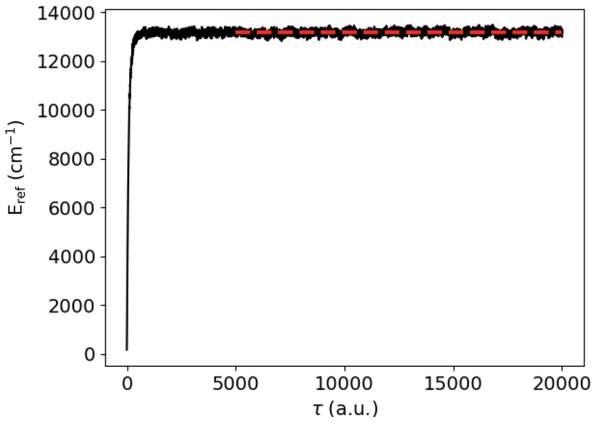

Figure 3.2: The value of E_{ref}, plotted as a function of the simulation time, τ, for a calculation of the ground state of $H^+(C_2H_4)$ (black solid line). The red dashed line provides the average value of E_{ref} based on this simulation.

3.3.1 Isotope Effects on the Ground State Properties

We start by considering the ground-state probability amplitudes for four isotopologues of ethyl cation, focusing on how the amplitudes of the motions of the five hydrogen atoms are affected by deuteration of either the ethylenic hydrogen atoms or the bridging proton. Figure 3.3 provides the results of this analysis. In these plots, the ground-state probability amplitude is projected onto the Cartesian coordinates of each of the five hydrogen atoms. Unless stated otherwise, the projections of the probability amplitude onto x, y and z Cartesian coordinates are obtained by rotating the coordinates of each of the walkers into an Eckart frame[1,61] that is based on a reference structure in which the isotopologue of ethyl cation has been rotated into a principle axis system. More specifically, in the reference structure, the carbon-carbon bond lies parallel to the x-axis, while the bridging proton lies in the xz-plane as is shown for $H^+(C_2H_4)$ at the left of Figure 3.1. Since the five hydrogen atoms are spatially separated, the projections of the probability amplitude onto the x and y coordinates of the five hydrogen atoms (lower panels of Figure 3.3) can be viewed in a single graph. Here, the probability amplitude for the bridging proton lies between the two carbon atoms, the positions of which

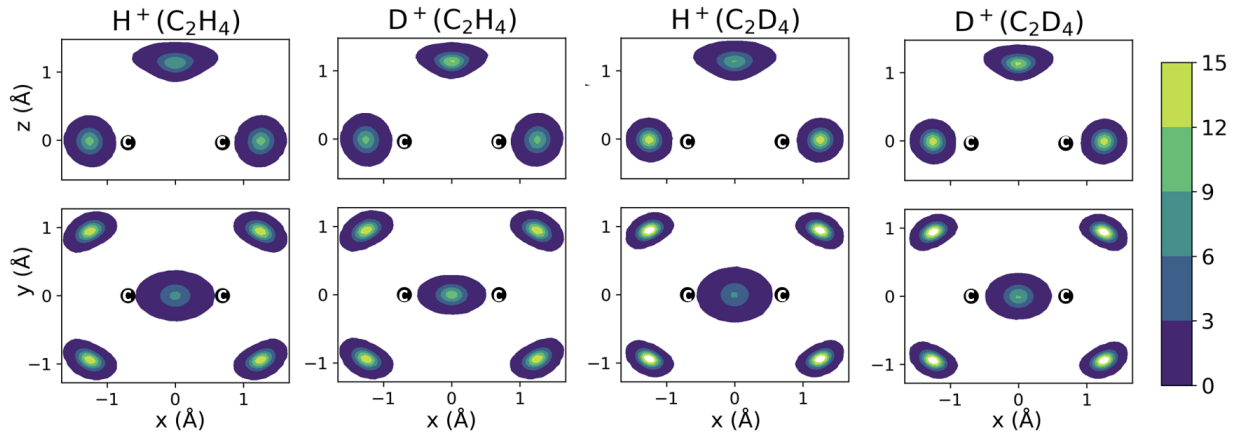

Figure 3.3: Projections of the ground-state probability amplitude onto (top) the x and z, and (bottom) x and y coordinates of each of the five hydrogen atoms in $H^+(C_2H_4)$, $D^+(C_2H_4)$, $H^+(C_2D_4)$, and $D^+(C_2D_4)$, respectively. The coordinate system is defined in Figure 3.1, and the black circles provide the positions of the carbon atoms in the equilibrium structure.

are shown with black circles with a white C. The probability amplitudes for the four ethylenic hydrogen atoms are at the four corners of the plot. For the projections of the probability amplitudes onto the x and z coordinates of each of the five hydrogen atoms, two pairs of distributions that correspond to the projection of the probability amplitude onto the coordinates of the ethylenic hydrogen atoms are identical, and only one member of each pair is plotted. These are the distributions in the upper panels of Figure 3.3 that are centered at $z = 0$ and $x = \pm 1.3$ Å.

We begin by considering $H^+(C_2H_4)$ and $D^+(C_2D_4)$. The most significant difference between these two sets of probability distributions is the decrease in the amplitude of the motions of the hydrogen atoms upon deuteration, which is expected. On the other hand, if we compare the distributions for the ethylenic hydrogen atoms for $H^+(C_2H_4)$ and $D^+(C_2H_4)$, and for $D^+(C_2D_4)$ and $H^+(C_2D_4)$, we find that they are nearly indistinguishable. Comparison of the probability distributions for the bridging proton shows larger differences upon deuteration of the ethylenic hydrogen atoms. This is most easily seen in the projections of the ground-state probability amplitude onto the x and y coordinates, where the $y-$component

of the probability distribution for the bridging proton is wider when the ethylenic hydrogen atoms are deuterated. Additionally, we note that the probability amplitude of the bridging proton remains between the two carbon atoms when this ion is in its ground vibrational state. This confirms the previous expectations that the ground state of the ethyl cation is localized in the non-classical structure.

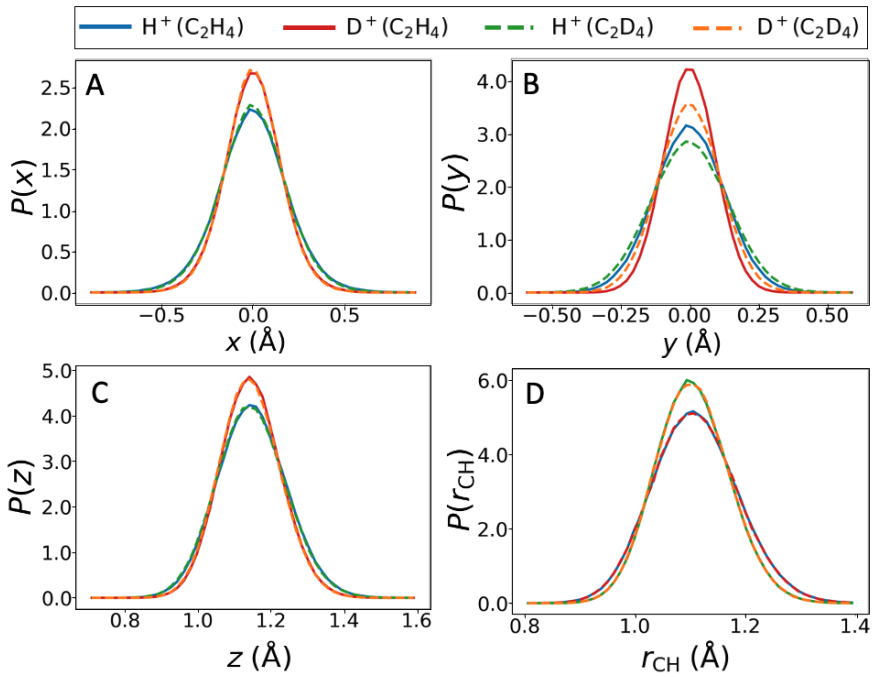

Figure 3.4: Projections of the ground-state probability amplitude, P, onto the (A) x, (B) y and (C) z coordinates of the bridging proton in $H^+(C_2H_4)$ (solid blue line), $D^+(C_2H_4)$ (solid red line), $H^+(C_2D_4)$ (dashed green line), and $D^+(C_2D_4)$ (orange dashed line) after the coordinates of the walkers have been rotated into an Eckart frame.[1] The coordinate system is defined in Figure 3.1. (D) The projection of the ground-state probability amplitude onto one of the ethylenic CH bond lengths.

To further explore the effect of deuteration onto the projections of the probability amplitudes onto the coordinates of the five hydrogen atoms, in Figure 3.4, we plot the one-dimensional projections of the ground-state probability amplitudes for the four isotopologues onto the three Cartesian coordinates of the bridging proton (panels A-C) and onto the CH

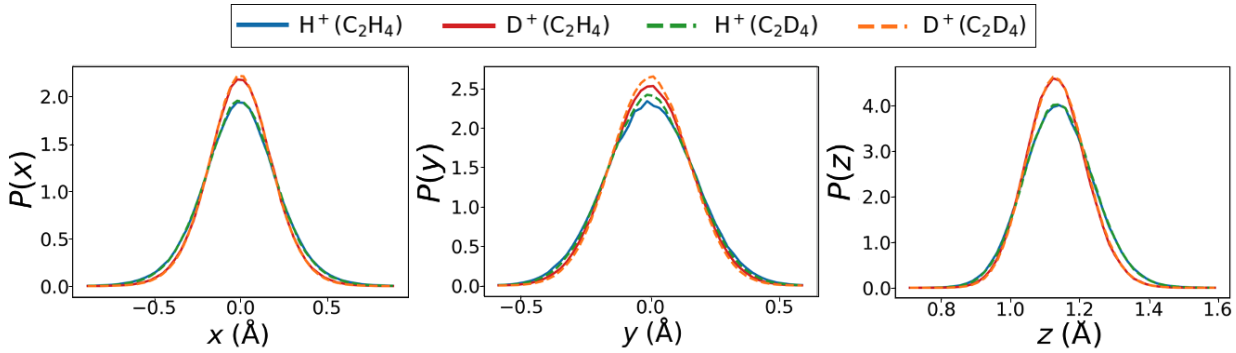

Figure 3.5: Projections of the ground-state probability amplitude onto the (A) x, (B) y and (C) z coordinates of the bridging proton, P, in $H^+(C_2H_4)$ (blue solid line), $D^+(C_2H_4)$ (red solid line), $H^+(C_2D_4)$ (green dashed line), and $D^+(C_2D_4)$ (orange dashed line). The coordinates are defined such that the origin is at the center of the C-C bond, with the carbon atoms lying on the x axis. The z axis is defined by the biscector of the torsion angle between the two CH_2 groups, and $y = z \times x$.

bond length of one of the ethylenic hydrogen atoms (panel D). The projections shown in panels A, C and D can be grouped into two pairs of nearly identical distributions, where the narrower distributions correspond to motions of a D deuterium atom and the broader distributions correspond to motions of a H atom. Interestingly, when we consider the projections of the ground-state probability amplitudes onto the displacement of the bridging proton perpendicular to the plane that contains CH^+C, all four distributions are unique. Here, the narrowest distribution corresponds to $D^+(C_2H_4)$, while the broadest one is for $H^+(C_2D_4)$. Overall, the distributions when the bridging proton is hydrogen are broader than when the bridging proton is deuterium, but the width also increases upon deuteration of the ethylenic hydrogen atoms. This trend is surprising. Further analysis shows that the larger differences among the distributions shown in Figure 3.4B is a consequence of the use of an Eckart embedding to define these Cartesian coordinates. There are two heavy carbon atoms in ethyl cation, which define the direction of the x axis; so, the Eckart rotation of the axis system about the $x-$axis is biased toward moving the deuterium atoms closer to their positions in the equilibrium geometry. This results in larger apparent displacements

of the lighter H atoms in the ion. This has the effect of enhancing the amplitude of the motion of the bridging proton in $H^+(C_2D_4)$ and diminishing the motion of the deuterium atom in $D^+(C_2H_4)$. When we use a geometric embedding, in which the $x-$axis lies along the CC bond axis, the bisector of the angle that defines the torsion of the terminal CH_2 groups provides the $z-$axis and $y = z \times x$, the projections of the probability amplitude onto the Cartesian components of the vector from the center of the CC bond to the bridging proton follow the trends described above. Plots of the projections of the probability amplitude onto these coordinates are provided in Figure 3.5.

Table 3.1: Ground-State Rotational Constants.[a,b]

System	$B_{xx}(\mathrm{cm}^{-1})$	$B_{yy}(\mathrm{cm}^{-1})$	$B_{zz}(\mathrm{cm}^{-1})$
$H^+(C_2H_4)$	3.4058(14)	0.8672(1)	0.7768(1)
$D^+(C_2H_4)$	2.7545(11)	0.8173(4)	0.7786(3)
$H^+(C_2D_4)$	1.9742(5)	0.6549(1)	0.5336(1)
$D^+(C_2D_4)$	1.7322(14)	0.6257(3)	0.5342(2)

[a] Evaluated based on an Eckart embedding.[1,61] The calculated off-diagonal rotational constants are smaller than 3×10^{-4} cm^{-1}, which is smaller than their uncertainties.

[b] Reported values reflect the average over 5 simulations, each of which has approximately 1 500 000 walkers. Standard deviations are provided in parentheses.

Table 3.2: Equilibrium Rotational Constants

System	$B_{xx}(\mathrm{cm}^{-1})$	$B_{yy}(\mathrm{cm}^{-1})$	$B_{zz}(\mathrm{cm}^{-1})$
$H^+(C_2H_4)$	3.5512	0.8916	0.7921
$D^+(C_2H_4)$	2.8688	0.8173	0.7921
$H^+(C_2D_4)$	2.0354	0.6694	0.5432
$D^+(C_2D_4)$	1.7884	0.6403	0.5432

One set of experimental observables that depends on the ground-state probability amplitude is the vibrationally averaged rotational constants. The rotational constants can be

evaluated by rotating each of the walkers in the ensemble based on the Eckart conditions,[1,61] and evaluating the elements of the inverse of the moment of inertia tensor. One half the ensemble averaged value of the elements of the vibrationally averaged inverse moment of interia tensor gives the vibrationally averaged rotational constants.[62] The results of this analysis for the four isotopologues are provided in Table 3.1. As expected, the rotational constants are consistent with a near prolate symmetric top molecule. They are all smaller than the values of the rotational constants obtained from the equilibrium structures, which are provided in Table 3.2. This decrease is largest for the B_{xx} values, reflecting the large amplitude of the zero-point motion of the bridging proton. These rotatinal constants should aid in the assignment of future rotationally resolved spectra of ethyl cation.

3.3.2 Excited States

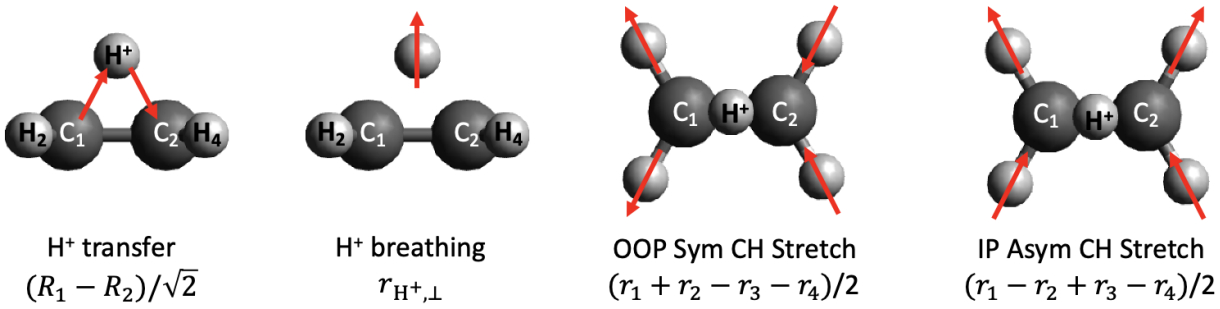

Figure 3.6: Illustrations and definitions of the vibrational motions that correspond to the excited states of $H^+(C_2H_4)$ explored in this studies.

We now turn our attention to vibrationally excited states, which are calculated using the fixed-node approximation, described above. As noted in the Introduction, spectra have been reported for the $H^+(C_2H_4)$ isotopologue of the ethyl cation,[2,3,13] and we begin our discussion with the excited-state energies of this ion. We focus on excitations involving four vibrations. These are illustrated in Figure 3.6. They include the proton transfer vibration, which is defined as the difference between the distances between the bridging proton and

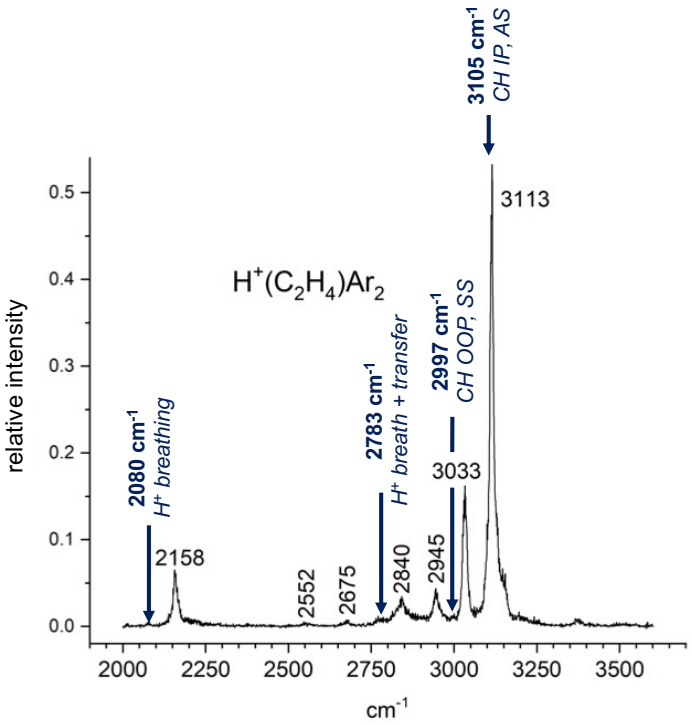

Figure 3.7: Comparison of the previously reported spectrum of $H^+(C_2H_4)Ar_2$[2] (black trace) and the energies obtained from the fixed-node DMC calculations (blue arrows). The spectrum is adapted with permission from *Chem. Phys. Lett.* **2009**, *480*, 17-20. Copyright 2009, Elsevier.

the carbon atoms, $(R_1 - R_2)/\sqrt{2}$, the proton breathing vibration, which corresponds to the displacement of the bridging proton perpendicular to the C-C bond axis, the out-of-phase symmetric CH stretch, and the in-phase antisymmetric CH stretch. The definitions of these coordinates are also provided in Figure 3.6. On the basis of harmonic and VPT2 calculations, the 1-0 transitions in the last three of these vibrations have been assigned to the peaks at 2158, 3033 and 3113 cm^{-1} in the spectrum reported by Ricks *et al.*[2,3] This spectrum is reproduced in Figure 3.7. Additionally, the transition at 2840 cm^{-1} recently has been assigned as a transition to the state with one quantum of excitation in the breathing motion of the bridging proton as well as one quantum of excitation in the proton transfer vibration.[3] On the basis of these assignments, we focus on the states with one quantum of

excitation in each of these four vibrations as well as the state with one quantum of excitation in both the breathing and the proton transfer vibrations. For all but the breathing vibration, the first excited states is characterized by the wave function changing sign when the value of the coordinate associated with the excitation is zero.

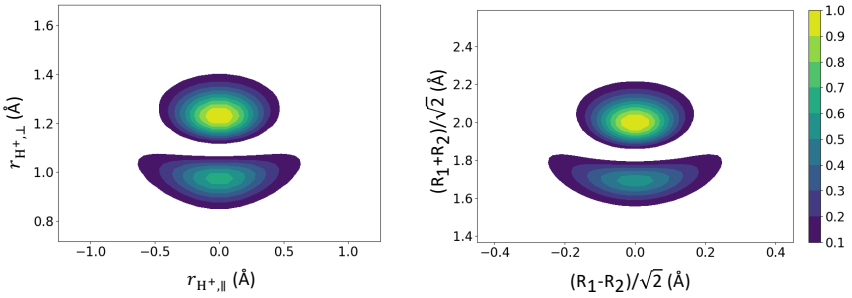

Figure 3.8: Plots of the probability amplitude obtained from two-dimensional calculations of the state with one quantum of excitation in the breathing vibration. For these calculations, all of the other coordinates were constrained to their positions in the minimum energy geometry. The calculations were performed using the procedures described elsewhere.[3] From these plots, we note that there is greater curvature in the node when the calculation is performed in the coordinates that describe the distance of the bridging proton from the two carbon atoms, R_1 and R_2, compared to when this motion is described in terms of the displacement along ($\parallel$) and perpendicular to ($\perp$) the CC bond axis.

Table 3.3: The Location of the Nodal Surface (in Å)[a]

System	H^+ breathing	H^+ transfer + breathing
$H^+(C_2H_4)$	1.149	1.165
$D^+(C_2H_4)$	1.140	1.153
$H^+(C_2D_4)$	1.149	1.165
$D^+(C_2D_4)$	1.140	1.153

[a] Measured as the distance of the bridging proton from the CC bond axis.

The situation is more complicated for the breathing vibration. As noted above, we employ the ADMC approach[26,62] to identify the location of the node in this coordinate. The

accuracy of the fixed-node approach relies on the nodal surface being well-described by a plane in the $(3N-6)$-dimensional coordinate space used to describe $H^+(C_2H_4)$. There are several ways one could define the breathing vibration. By analogy to the proton transfer vibration, one choice would be to use $(R_1+R_2)/\sqrt{2}$. Another focuses on the displacement of the bridging proton from the CC bond. We preform two-dimensional calculations that focus on the motion of the bridging proton in the symmetry plane that contains the CC bond, where all of the other atoms are constrained to their values in the equilibrium geometry using both of these sets of coordinates. The probability amplitude for the state with one quantum in the breathing vibration are provided in Figure 3.8. As can be seen, when we define the breathing coordinate as the displacement of the bridging proton from the CC bond, the node shows much less curvature compared to when the node is defined by $(R_1+R_2)/\sqrt{2}$. For this reason, we define the node for the breathing vibration in terms of the distance of the bridging proton from the C-C bond, and the resulting positions of the nodes for these excited states are reported in Table 3.3.

The results of the fixed-node calculations of the excited-state energies are indicated with blue arrows in Figure 3.7 and in the third column of Table 3.5 (shown at the end of this chapter). We also provide the VPT2 energies obtained at the MP2/aug-cc-pVTZ level of theory/basis, which were reported recently.[3] In general, the agreement between the fixed-node DMC energies and the measured line positions is good, but there are notable differences. There are two sources for these differences. The first is in the experiment. The recorded spectrum is based on monitoring the loss of an argon atom from $H^+(C_2H_4)\cdot Ar_2$, so the spectrum that is reported is for $H^+(C_2H_4)\cdot Ar_2$ rather than $H^+(C_2H_4)$. Based on calculations by us[3] and by Ricks *et al.*,[2] the argon atoms bind to the bridging proton, so they are expected to have a larger impact on the frequency of vibrations involving the bridging proton than on the outer hydrogen atoms. This is consistent with the 5 and 35 cm^{-1} differences between the DMC and measured energies for the CH stretching vibrations compared to a 70 cm^{-1} difference for the proton breathing vibration. The second source of the differences between measured and calculated energies comes from the treatment of the nodal surfaces as $(3N-7)$-

dimensional hyperplanes, where the node is defined to exist at a single value of the coordinate that corresponds to the vibration that is being excited. In addition to possible sensitivities of the calculated energy to how this coordinate is defined,[57] this description of the nodal surface does not account for possible couplings between nearly degenerate vibrations. In this way, the excited-state energies obtained from the DMC simulations should be considered to be those of the deperturbed bright states, rather than that of the vibrational eigenstates.

On the basis of VPT2 calculations,[3] of the states considered here, the state with one quantum of excitation in the breathing vibration is found to shift by 60 cm^{-1} when couplings to nearly degenerate levels are introduced. The states with one quantum of excitation in the CH stretching vibrations show much smaller shifts. The value of the shift in the energy of the breathing vibration is in line with the difference between the calculated and measured excited-state energy for the first excited state in this vibration, although the shift is in the opposite direction. Likewise, when we compare the differences between the calculated and measured energies of states with one quantum of excitation in the CH stretching vibrations, the differences are consistent with the 22 cm^{-1} and 63 cm^{-1} differences between the measured and calculated OH stretch frequencies in $H^+(H_2O)_2$[57] and $H_3O_2^-$,[63,64] respectively. Finally, the energy of the state with one quantum of excitation in the breathing and proton transfer vibrations is roughly the sum of the energies of the states with one quantum in both of these vibrations. The energy of the state with one quantum of excitation in the proton transfer vibration is surprisingly low and likely reflects the fact that the non-classical minimum energy structure results from the interaction of the CH bond with the unfilled *p*-orbital on the CH_2 group when one considers the classical ^+H_3C-CH_2 structure.[65] It would be interesting if this very low-frequency transition could be measured.

We can also compare the DMC energies for $H^+(C_2H_4)$ to previously reported VPT2 results. In general, the agreement between the present results and the measured transitions is better than that obtained from the VPT2 calculations. The differences likely reflect a combination of the higher level of electronic structure theory used to develop the potential used in this study, and the improved treatment of anharmonicity. The latter is particularly impor-

tant in describing the vibrations that involve the bridging proton. In addition to providing better agreement with experiment, the DMC studies allow us to explore properties of the ground- and excited-state wave functions through projections of the probability amplitude.

Finally, for the two excited states that involve the bridging proton, there are two possible ways to define the node. For the breathing vibration we noted above that there is less curvature in the probability amplitude obtained from a two-dimensional calculation when the node is described by the displacement of the bridging proton from the CC bond. As reported in Table 3.5, if we define the node using a value of $(R_1 + R_2)/\sqrt{2}$, the resulting energy lowers by nearly 500 cm^{-1}, and is in less good agreement with experiment. The excited-state energy for the proton transfer mode is less sensitive to the coordinate used to describe the position of the node, and the energies obtained from calculations performed using $(R_1 - R_2)/\sqrt{2}$ and the displacement of the bridging proton parallel to the CC axis differ by only 4 cm^{-1}, which is smaller than the uncertainties of either of these calculations.

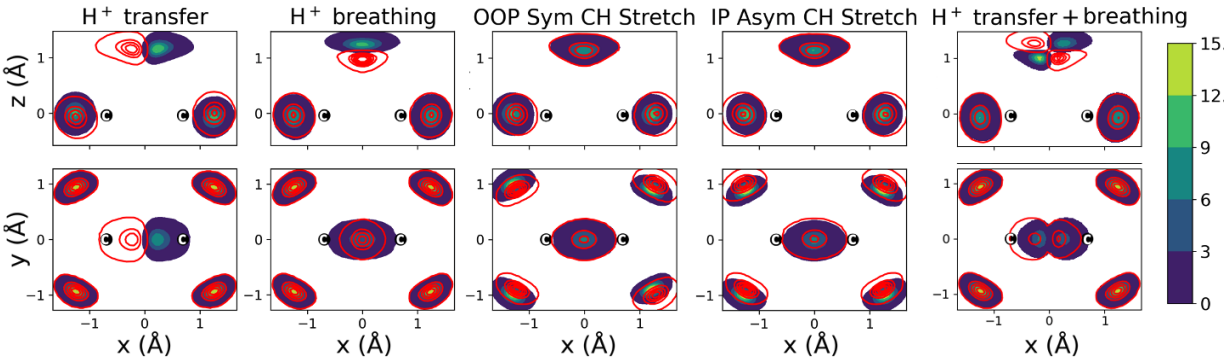

Figure 3.9: Projections of the excited-state probability amplitude onto (top) the x and z, and (bottom) the x and y coordinates for each of the five hydrogen atoms in $H^+(C_2H_4)$. The shaded contour plot shows probability amplitude obtained for the regions where the wave function has positive amplitude, while the red contour lines show the probability amplitude obtained for the regions where the wave function has negative amplitude. Illustrations and definitions of the coordinates are provided in Figure 3.6, and the black circles provide the positions of the carbon atoms in the equilibrium structure.

To further explore possible large couplings between these vibrations, which could lead to

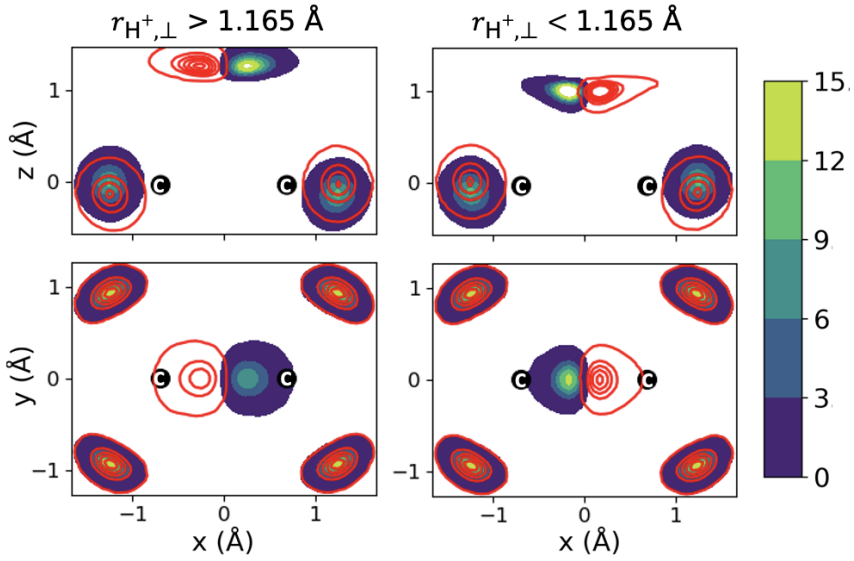

Figure 3.10: Projections of the excited-state probability amplitude for the state of $H^+(C_2H_4)$ with excitation in the proton transfer and breathing vibrations (see Figure 3.6). In this plot, the probability amplitude has been divided into the part for which $r_{H^+,\perp} > 1.165$ Å, and the part where $r_{H^+,\perp} < 1.165$ Å to illustrate the response of other coordinates to the displacement of the bridged proton.

more complex nodal structures, we consider the projections of the probability amplitude for each of the five excited states considered in this study onto the coordinates of the hydrogen atoms. In these calculations, the probability amplitude that is obtained from the nodal regions where the wave function has positive and negative amplitude are evaluated separately. In the plots in Figure 3.9, the probability amplitude obtained from the part of the wave function with positive amplitude is represented by the color map, while the part for which the wave function has negative amplitude is shown with the red contour lines. Since the state with two quanta of excitation is composed of four regions, we further divide the probability amplitude on the basis of the value of $r_{H^+,\perp}$ in Figure 3.10.

Overall, the largest differences between the two contour plots that represent the probability amplitude for one of the excited states are seen in the probability amplitudes for the hydrogen atom that is involved in the motion along which the ion is being excited. For

example when the proton transfer vibration is excited, the red contour that corresponds to the projection of the probability amplitude onto the coordinates of the bridging proton is localized at negative values of x, while the color map contour only has amplitude for $x > 0$. Likewise, the color map contours for the bridging proton when the breathing vibration is excited lie at larger values of z compared to the red contour lines. Similar trends are found for the excited state where both the breathing and proton transfer vibrations are excited. In contrast, for these excited states the projections of the probability amplitude onto the coordinates of the bridging proton are relatively unaffected by excitation of the ethylenic hydrogen atoms.

When we consider states in which the excitation involves the outer ethylenic hydrogen atoms, there are shifts between the color map and red contours that represent the projections of the probability amplitudes for each of the four hydrogen atoms onto the xy plane. The directions of these shifts are consistent with the vibrational motions illustrated in Figure 3.6. In contrast to the bridging proton, the probability distributions represented by the color map and red contours overlap. This is a reflection of the fact that the CH bonds do not line parallel to the xy plane in the equilibrium geometry of ethyl cation.

The only excited state for which there are notable changes in the projection of the probability amplitude of the ethylenic hydrogen atoms when the excitation involves the bridging proton is seen for the state in which the proton transfer vibration is excited. In the projection of the probability amplitude for this state onto the xz plane, we see a slight shift between the two contour plots that represent the projection of the probability amplitude onto the positions of the ethylenic hydrogen atoms. The shift is primarily in the $z-$direction, and reflects a coupling between the proton transfer motion and the out-of-phase umbrella vibrations of the outer CH_2 groups. Such a coupling is not surprising. As the bridging proton is shifted toward one of the carbon atoms, the system is being driven toward the classical $^{+}H_3C\text{-}CH_2$ structure. While this coupling can be seen in the plots of the projected excited-state probability amplitude, it is small and not likely to have a significant influence on the excited-state energies. Similar shifts are seen in the probability amplitude for the state with one quantum

of exciation in both the proton transfer and breathing vibration of the bridging proton. This is more easily seen when the distributions for the four nodal regions are plotted separately (see Figure 3.10).

Table 3.4: Root-Mean-Squared Displacement in Å of the x Coordinate of the Bridging Proton Defined in Figure 3.11.

State	$H^+(C_2H_4)$	$D^+(C_2H_4)$	$H^+(C_2D_4)$	$D^+(C_2D_4)$
Ground state	0.2202(9)	0.1846(10)	0.2166(3)	0.1814(5)
H^+ transfer	0.3417(8)	0.2799(18)	0.3335(14)	0.2752(8)
H^+ breathing (top)[a]	0.2545(13)	0.2192(10)	0.2505(7)	0.2154(11)
H^+ breathing (bottom)[a]	0.1653(3)	0.1426(3)	0.1639(3)	0.1416(4)
OOP Sym CH stretch	0.2206(6)	0.1859(8)	0.2169(7)	0.1819(6)
IP Asym CH stretch	0.2206(9)	0.1855(12)	0.2175(7)	0.1823(7)
H^+ transfer + breathing (top)[a]	0.3535(7)	0.3100(10)	0.3490(8)	0.3052(12)
H^+ transfer + breathing (bottom)[a]	0.2595(11)	0.2144(5)	0.2570(7)	0.2121(3)

[a] Top and bottom refer to the parts of the probability amplitude for states with excitation in the breathing vibration that correspond to larger (top) and smaller (bottom) values of the z coordinate of the bridging proton.

For all of the excited states considered in this study, the projected probability amplitude for the bridging proton remains between the two carbon atoms upon excitation of proton transfer vibration. This can be seen in the projections that are provided in Figure 3.9 and the root mean squared displacements of the bridged proton, which are reported in Table 3.4. These resultes indicate that while the displacement of the shared proton parallel to the CC bond is driving the system toward the classical structure, the wave function is not sampling the classical ^+H_3C-CH_2 geometry. This is further supported by the fact that the DMC simulation of this state does not show any evidence of exchange of hydrogen atoms between the ethylenic and bridged environments.

Having established that the fixed-node treatment provides reliable energies for $H^+(C_2H_4)$, we turn our attention to the other isotopologues. At first glance, the overall trends are not surprising. Since all of these vibrations involve primarily motions of the hydrogen atoms, their energies in $D^+(C_2D_4)$ are all reduced by roughly a factor of $\sqrt{2}$. Likewise, in $D^+(C_2H_4)$

and $H^+(C_2D_4)$, the vibrational energies are very close to the energy of the corresponding vibration in $H^+(C_2H_4)$ and $D^+(C_2D_4)$. The most notable energy shift is in the frequency of the proton transfer vibration, which increases by 13 cm^{-1} when the ethylenic hydrogen atoms are deuterated. This might reflect the slightly shorter average CC bond distance in $H^+(C_2D_4)$ compared to $H^+(C_2H_4)$. On the basis of the DMC calculations, 0.001 Å. Likewise, the probability amplitudes for these excited states follow the trends described above for the ground states of the various isotopologues and for the excited states of $H^+(C_2H_4)$. The resulting distributions are provided in Figure 3.11 (shown at the end of this chapter).

3.4 Conclusion

In this study, we explored the ground- and excited- state properties of the ethyl cation, $H^+(C_2H_4)$, and its deuterated analogues. This work confirms that the states of $H^+(C_2H_4)$ that were probed in previous spectroscopic studies[2,13] are localized in the non-classical minimum on the potential surface. While excitation of the bridged proton drives the ion toward the classical $^+H_3C\text{-}CH_2$ structure, the wave function does not access structures that can be assigned as a carbocation. Additionally, the calculated energies of the vibrationally excited states support previous assignments of the spectra for this ion.

We also explored the effects of partial and full deuteration on the ground- and excited-state probability amplitude and excited-state energies. For the most part, the shifts in the probability amplitude and vibrational frequencies associated with the bridging protons and ethylenic hydrogen atoms are unaffected by deuteration in the other position. An exception is in the frequency of the proton transfer vibration of $H^+(C_2H_4)$, which shows a 13 cm^{-1} shift upon deuteration of the ethylenic hydrogen atoms. A similar shift is seen in the energy of the state with one quantum of excitation in both the H^+ transfer and H^+ breathing vibration, and spectroscopic characterization of this isotopologue could provide interesting insights into the impacts of deuteration on the structure and amplitude of vibrational motion of this carbocation.

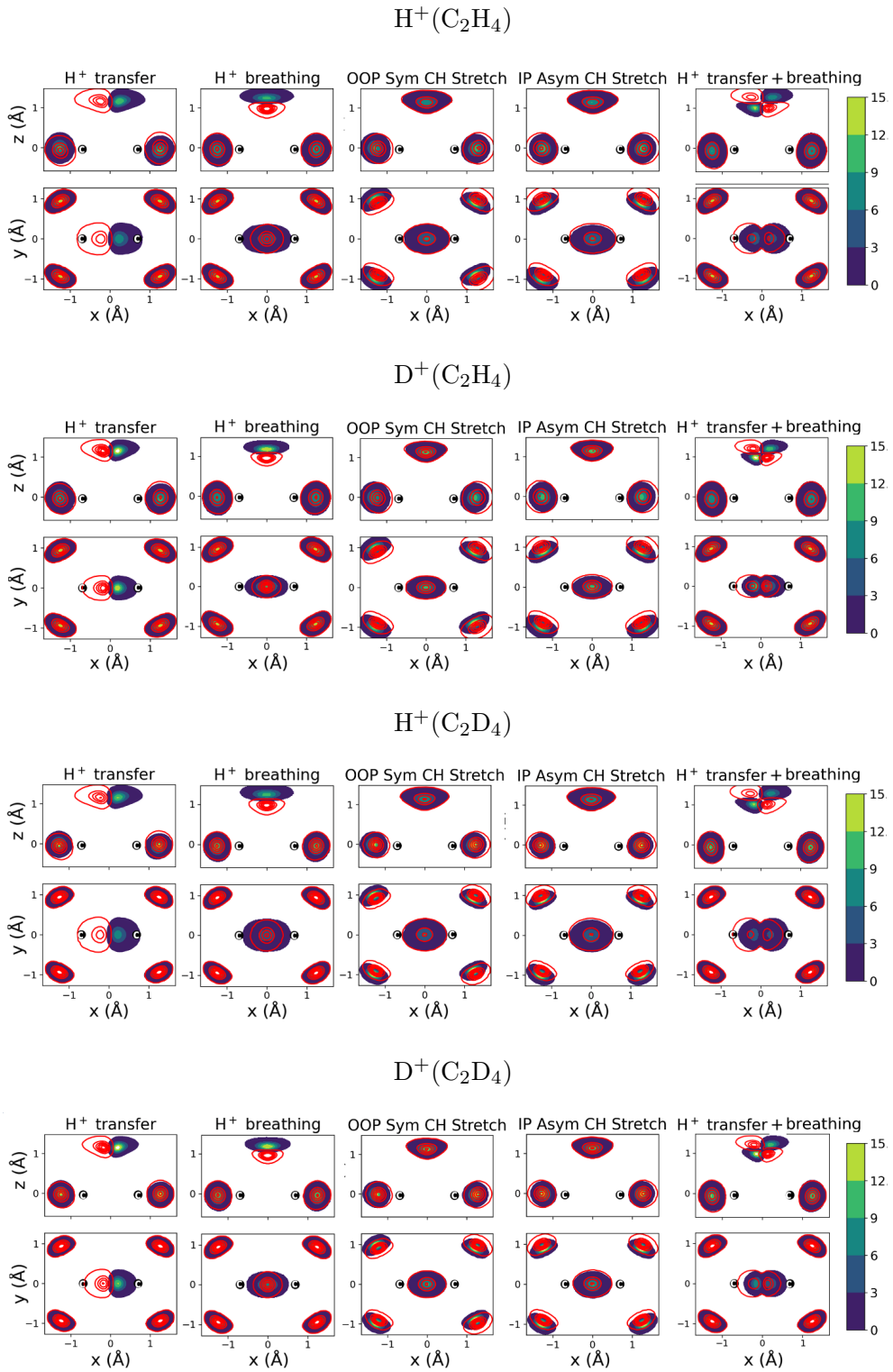

Figure 3.11: Projections of the excited state probability amplitude onto (top) the x and z coordinates, and (bottom) the x and y coordinates of each of the hydrogen atoms in $H^+(C_2H_4)$, $D^+(C_2H_4)$, $H^+(C_2D_4)$, and $D^+(C_2D_4)$ for each vibrational mode defined in Figure 3.6 after the walkers have been rotated into an Eckart frame[1] defined in Figure 3.1, and the black circles provide the positions of the carbon atoms in the equilibrium structure.

Table 3.5: Vibrational Energies in cm^{-1}.[a]

State[a,b]	$H^+(C_2H_4)$ Experiment[c]	$H^+(C_2H_4)$ DMC[d]	$H^+(C_2H_4)$ VPT2[e]	$D^+(C_2H_4)$ DMC[d]	$H^+(C_2D_4)$ DMC[d]	$D^+(C_2D_4)$ DMC[d]
Ground state	–	13 177(3)	13 360	12 668(3)	10 452(4)	9938(2)
H^+ transfer	–	616(9)[f]	697	491(7)	629(6)	494(5)
H^+ breathing	2158	2080(10)[g]	2263	1504(6)	2090(6)	1505(7)
OOP Sym CH stretch	3032	2997(9)	3060	3002(5)	2194(9)	2181(5)
IP Asym CH stretch	3114	3110(10)	3154	3109(7)	2348(7)	2340(4)
H^+ transfer + breathing	2840	2783(5)	3091	2041(9)	2795(6)	2043(4)

[a] Ground state energy is reported relative to the potential minimum. All excited state energies are reported relative to the ground state.

[b] See Figure 3.6 for definitions and illustrations of the vibrations.

[c] Refs. 2 and 3.

[d] Average based on 5 (ground state) or 10 (excited state) DMC simulations with 50 000 walkers and $\Delta\tau = 1$ a.u., as described in the text. Standard deviations are provided in parentheses.

[e] Results of VPT2 calculations at the MP2/aug-cc-pVTZ level of theory.[3]

[f] When this excited state is defined by $r_{H^+,\parallel} = 0$, the energy is 612(5) cm^{-1}.

[g] When this excited state is defined by $(R_1 + R_2)/\sqrt{2}$, the energy is 1791 cm^{-1}.

Chapter 4

EVALUATION OF INFRARED INTENSITIES USING DIFFUSION MONTE CARLO

Reproduced in part with permission from [Pattarapon Moonkaen, and Anne B. McCoy. Evaluation of Infrared Intensities using Diffusion Monte Carlo. *J. Phys. Chem. A* **2025**, 129 (11), 2705-2717]. Copyright [2025] American Chemical Society.

4.1 Introduction

Spectroscopy has played an important role in the development of quantum chemistry as it provided the experimental evidence that energy levels are quantized. Vibrational spectroscopy also provides a valuable tool for determining molecular structures. By considering the intensities as well as the energies of transitions in the vibrational spectra of molecules, we obtain information about mode couplings as well as any changes in the electronic structure that result from vibrational excitation. These connections require tools for calculating the intensity as well as frequency of transitions from a potential and dipole moment surface.

For the electronic-structure problems, which are based on interacting charged particles, all interactions are Coulombic and the energy spacing between the ground and excited states is generally large. Once the Born-Oppenheimer separation between the electronic and nuclear degrees of freedom is introduced, the potential energy surface for the nuclear degree of freedom cannot be expressed in a simple, general form. This means that there is not a universal set of coordinates that can be used to solve all vibrational problems, and often the best approach is to make a careful choice of coordinates so as to improve the accuracy of any approximations that must be invoked to solve the vibrational problem. This lack of generality makes solving the vibrational problems challenging.[18,66–72]

One method for solving for the ground-state vibrational energy and wave function, which does not rely on a careful coordinate choice, is diffusion Monte Carlo (DMC).[22,31,54,73–75] The implementation of DMC is general and is very accurate even for molecules that display large amplitude or strongly coupled vibrational motions. Indeed, the accuracy of the DMC approach is only limited by the accuracy of the potential surface used for the calculation. Likewise, since the Monte Carlo aspects of the approach scale roughly linearly with system size, the overall computational scaling of the DMC approach depends on the computational requirements for the evaluation of the potential energy. Since DMC is a ground-state method, extensions are needed to evaluate excited-state energies as well as the matrix elements involving two different vibrational states, which are needed to calculate intensities. The evaluation of matrix elements is particularly challenging as the DMC simulation provides a Monte Carlo sampling of the wave function for the state of interest, and the sampled geometries will be unique to each simulation.

Over the past several years, we have explored several approaches for obtaining excited-state energies and intensities using DMC. For example, in a recent study, we developed a spectral map that provided linear relationships between geometrical parameters, specifically OH bond lengths, and the frequencies and intensities of OH stretching transitions in protonated water clusters.[76,77] While this approach provided a qualitative fit to the spectrum, we can improve the approximation by utilizing the full ground-state probability amplitude and approximate excited states by products of the ground-state wave function that is obtained from DMC and low-order polynomial expansions in the $3N-6$ vibrational coordinates. This approach, which we have called the ground-state probability amplitude (GSPA) approach, has been applied to $H_3O_2^-$,[58] $H_5O_2^+$[52] and larger protonated water clusters.[78] A third approach that we have explored extensively involves a fixed-node approximation for obtaining excited states.[31,54] In this approximation, a nodal surface is imposed, and any structure in the ensemble that attempts to cross that nodal surface is removed from the simulation. This approach was shown to provide accurate excited-state energies for $H_3O_2^-$.[79] These previous studies focused on states with one or in some cases several quanta of excitation, typically

involving a single vibrational motion. In this way, they provide the frequency of the zero-order bright state in the chosen region of the spectrum. Possible couplings of these states to states that involve multiple quanta of excitation in lower-frequency vibrations can be identified by comparing projections of the probability amplitude of the ground and excited states onto these coordinates and exploring how the probability amplitude changes with vibrational excitation.

Calculating intensities from the ground- and excited-state wave functions obtained from separate DMC simulations introduces challenges as the two states are represented by different ensembles of structures, each of which provides a Monte Carlo sampling of the wave function for the state of interest. To address this challenge we have used the descendant weighing approach, which allowed us to obtain probability amplitudes,[23,24] to calculate the matrix element needed to evaluate the intensities of transitions in $H_3O_2^-$.[80] While this approach appeared promising, we found it to be computationally expensive and numerically unstable when applied to excited states that were calculated using the fixed-node approach.

In the present study, we will focus on using guided DMC to obtain excited-state energies and intensities. In the guided DMC approach,[36,54] the quantity that is sampled is the product of the wave function for the state of interest and a guiding function, ϕ^T, which is constructed to provide a reasonable approximation to the wave function for the state of interest. We have shown that, for water clusters[81,82] as well as protonated water clusters,[9,83] guiding functions that are formed from products of ground-state wave functions that describe the OH stretching and HOH bending motions in water work well for these systems. In the present study, we will extend this idea and develop guiding functions for describing OH stretching and HOH bending motions for states with one quantum of excitation in an OH stretching vibration.

With methods for evaluating the excited-state energies and wave functions using guided DMC, two approaches have been proposed for evaluating matrix elements involving these states. The first one replaces the wave functions for one of the states with the trial wave function, and we will refer to this approach as the trial wave function (TWF) approach.[54,84] A second approach employs the descendant weighing (DW) approach we had used in earlier

studies,[80,84] but basing the calculations on ground- and excited-state wave functions that were obtained using guided DMC calculations.

The above approaches will be investigated for a series of systems including water,[85,86] $H_3O_2^-$[87] and $H_5O_2^+$.[88] We will also explore the behavior of these approaches on two model systems: a one-dimensional harmonic oscillator and a four-dimensional model of $H_3O_2^-$ as these, along with water, provide opportunities to compare the results to those of converged basis set calculations.

Among the motivations for focusing on $H_3O_2^-$ and $H_5O_2^+$ are that there have been several calculations of the energies of these ions using the same potential surface that is used in the present study.[87,88] These approaches include multiconfigurational time-dependent Hartree (MCTDH),[89,90] vibrational self-consistent field calculations with configuration interaction (VSCF/CI)[91] as well as fixed-node DMC calculations.[79] Likewise, there are also a variety of calculations of the spectra of $H_5O_2^+$ using the same potential and dipole surfaces used in this study.[88] These calculations include MCTDH,[92,93] as well as fixed-node DMC[57] calculations. Both ions have also been studied spectroscopically.[94,95] This will allow us to compare the frequencies and intensities obtained from the guided DMC calculations to those obtained from other approaches as well as to the measured spectrum.

4.2 Methods

4.2.1 Diffusion Monte Carlo

The diffusion Monte Carlo (DMC) approach and our implementation have been described in chapter 2 and also in other places.[22–24,31,54] Below, we summarize the aspects of DMC that are important for the present study. The reader is referred to the earlier studies for more detailed descriptions.[22–24,30,54]

4.2.2 Overview of Guided DMC

In the present study, we employ guided DMC, in which the DMC simulation samples the product of the solution to the time-independent Schrödinger equation, Ψ, and a trial wave function, ϕ^T. For this approach to be effective, ϕ^T should provide a good approximation to Ψ for the state of interest. An important consideration in selecting ϕ^T is that it samples the relevant configurations. For excited states, the node should be as accurate as possible. This is simplified in the present study as we will focus on excited states where the position of the node is determined by symmetry.

In guided DMC, the quantity that is evaluated is the product of Ψ_n and ϕ_n^T, which is represented by f_n, where

$$f_n(\mathbf{x}) = \Psi_n(\mathbf{x})\phi_n^T(\mathbf{x}) = \sum_j w_j^{(n)} g\left(\mathbf{x} - \mathbf{x}_j^{(n)}\right) \tag{4.1}$$

and n is used to represent the state of interest. In Eq. (4.1), $g\left(\mathbf{x} - \mathbf{x}_j^{(n)}\right)$ represents a function that is localized at $\mathbf{x}_j^{(n)}$. This function is often referred to as a walker. In the DMC simulation, the positions of the walkers, as well as their associated weights, w_j, are propagated in imaginary time, $\tau = it/\hbar$, according to the imaginary-time time-dependent Schrödinger equation. In Eq. (4.1) and the following discussion, the walkers are identified by the subscript j.

Substituting f_n/ϕ_n^T into the imaginary-time time-dependent Schrödinger equation, we obtain the working equations for DMC[36]

$$\frac{\mathrm{d}f_n}{\mathrm{d}\tau} = \sum_{k=1}^{n_a}\left[\frac{\hbar^2}{2m_k}\vec{\nabla}_k^2 - \vec{\nabla}_k \cdot \vec{D}_k(\mathbf{x})\right] f_n(\mathbf{x}) - (E_L(\mathbf{x}) - E_{\mathrm{ref}})f_n(\mathbf{x}) \tag{4.2}$$

where n_a provides the number of atoms in the system of interest,

$$E_L(\mathbf{x}) = \frac{H\phi_n^T(\mathbf{x})}{\phi_n^T(\mathbf{x})} \tag{4.3}$$

is the local energy, and

$$\vec{D}_k(\mathbf{x}) = \frac{\hbar^2}{m_k}\frac{1}{\phi_n^T(\mathbf{x})}\vec{\nabla}_k\phi_n^T(\mathbf{x}) \tag{4.4}$$

provides the drift term for the kth atom. In Eqs. (4.2)-(4.4) and in the discussion that follows, the k subscript will be used to refer to each individual atom in the molecule of interest. It should be noted that $\Delta\tau$ has units of 1/energy, while the drift term will have units of energy $\times$ length.

The DMC algorithm is obtained by replacing f_n in Eq. (4.2) with the expression in Eq. (4.1), and propagating the ensemble of walkers over a series of steps in imaginary time, $\Delta\tau$. In each time step, each walker is propagated independently by first displacing its position, accepting or rejecting the move based on microscopic reversibility, and updating its relative weight based on a comparison of the local energy to the reference energy, $E_{\text{ref}}(\tau)$. In the remainder of this discussion we will provide a description of each of these steps.

In the first step, the coordinates of each walker are displaced by an amount so that the new position of the jth walker is

$$\mathbf{x}'_j = \mathbf{x}_j + \mathbf{D}(\mathbf{x}_j)\Delta\tau + \boldsymbol{\delta}_j \tag{4.5}$$

The first contribution to the displacement comes from the drift term in Eq. (4.4) and has the effect of moving the walkers toward geometries where ϕ_n^T is large. The value of the additional displacement of each atom, $\delta_{k,j}$, is selected from a Gaussian distribution with a width of $\sigma_k = \hbar\sqrt{\Delta\tau/m_k}$.

Since the drift term is a function of $\mathbf{x}_j$, we need to consider if the displacement of the walker described by Eq. (4.5) satisfies the microscopic reversibility. This is achieved by evaluating the size of a random displacement that would be needed to move from $\mathbf{x}'_j$ to $\mathbf{x}_j$, $\boldsymbol{\delta}'_j$, based on

$$\mathbf{x}_j = \mathbf{x}'_j + \mathbf{D}(\mathbf{x}'_j)\Delta\tau + \boldsymbol{\delta}'_j \tag{4.6}$$

We then find the ratio of the probability of the move from $\mathbf{x}'_j$ to $\mathbf{x}_j$, $P(\mathbf{x}'_j \rightarrow \mathbf{x}_j)$ or the probability of the reverse move, to the probability of the move from $\mathbf{x}_j$ to $\mathbf{x}'_j$, $P(\mathbf{x}_j \rightarrow \mathbf{x}'_j)$ or the probability of the move that was taken. This can be expressed as[36]

$$P_j = \frac{P(\mathbf{x}'_j \rightarrow \mathbf{x}_j)}{P(\mathbf{x}_j \rightarrow \mathbf{x}'_j)} = \left(\frac{\phi_n^T(\mathbf{x}'_j)}{\phi_n^T(\mathbf{x}_j)}\right)^2 \prod_{k=1}^{n_a} e^{-\left(|\vec{\delta}'_{k,j}|^2 - |\vec{\delta}_{k,j}|^2\right)/2\sigma_k^2} \tag{4.7}$$

Equation 4.7 contains two contributions. The first is the ratio of the values of the probability amplitude at the coordinates of the walker before and after displacement, where the probability amplitude is approximated by the square of the trial wave function at that geometry. The second contribution reflects the relative probability of sampling $\boldsymbol{\delta}_j$ and $\boldsymbol{\delta}'_j$ from the Gaussian distribution described above. When $P_j \geq 1$ the probability of the reverse move is at least as large as the probability for the move that was taken, and the move is accepted. If $P_j < 1$, P_j is compared to a random number from a uniform random distribution between 0 and 1. If P_j is larger than the random number, the move is accepted. If P_j is smaller than the random number, the move is rejected and the walker remains at $\mathbf{x}_j$.

The final step in the DMC algorithm involves updating the weights of the walkers using[23,31]

$$w_j(\tau + \Delta\tau) = \exp\left\{\left(E_L(\mathbf{x}'_j(\tau)) - E_{\text{ref}}(\tau)\right)\Delta\tau\right\} w_j(\tau) = \Omega_j(\tau) w_j(\tau) \tag{4.8}$$

Even if a move is rejected, the weight of the walker is updated. In this work we use two approaches for updating the weights. In the first approach, we simply multiply $w_j(\tau)$ by $\Omega_j(\tau)$ as indicated by Eq. (4.8). This approach is referred to as continuous weighing since the weights will be represented by real numbers. In the second approach, all of the $w_j = 1$, and $\Omega_j(\tau)$ is used to determine the number of walkers at $\mathbf{x}_j(\tau)$ at the start of the next time step of the simulation. We have found this second, discrete weighting, approach to be more stable for most applications. The one important exception is when we use the descendant weighting approach for evaluating matrix elements using the descendant weighting approach,[80] described below.

At the end of each time step, E_{ref} is updated using the weighted average of the local energy of the walkers[22]

$$E_{\text{ref}}(\tau) = \frac{\sum_j w_j(\tau) E_L(\mathbf{x}_j(\tau))}{\sum_j w_j(\tau)} - \alpha \frac{\sum_j w_j(\tau) - \sum_j w_j(\tau = 0)}{\sum_j w_j(\tau = 0)} \tag{4.9}$$

where α is a simulation parameter. We find $\alpha = 0.5/\Delta\tau$ to be an effective choice for this parameter.[34,35] The second term in Eq. (4.9) ensures that the number of the walkers remains roughly constant throughout the simulation. At large τ, E_{ref} oscillates around the energy of the state of interest, and its time-averaged value provides the energy of that state.

4.2.3 Evaluation of Excited States Using Trial Wave Functions

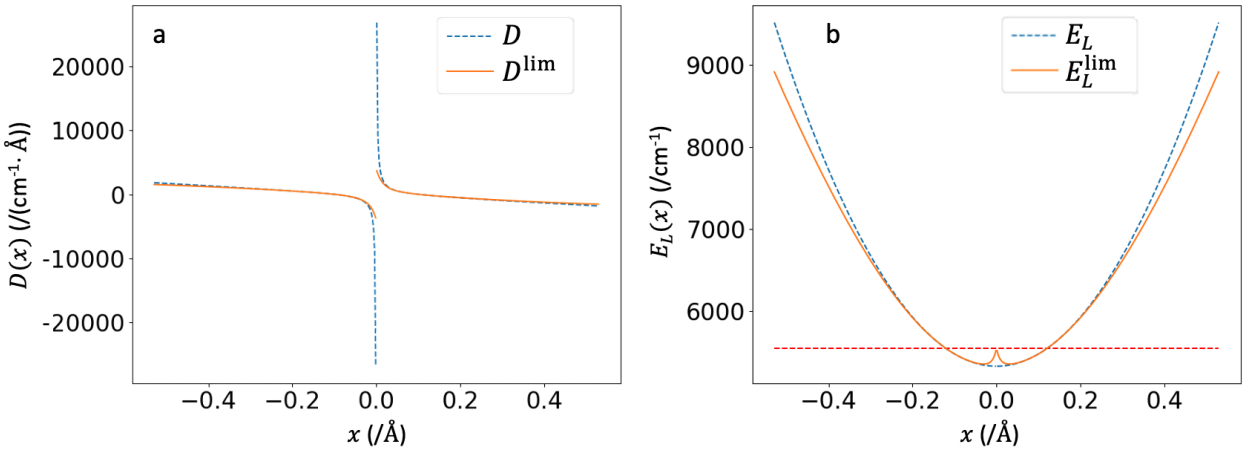

Figure 4.1: Comparison of the values of E_L (panel a) and D (panel b) in Eqs. 4.3 and 4.4 to the corresponding limiting values, D^{lim} and E_L^{lim}, defined in Eqs. 4.10 and 4.11, for a one-dimensional harmonic oscillator that describes the displacement of an OH bond with a frequency of 3700 cm^{-1}. For these plots, ϕ_1^T is defined according to Eq. 4.23 with $\beta = 0.98$. The dashed blue lines provide the values for D and E_L, while the solid orange curves provide the corresponding limiting values. Evaluation of E_L^{lim} requires a choice of E_{ref}, and we have used the energy of the first excited state of this system, $E_1 = 5550$ cm^{-1}, which is indicated by the dashed red line.

The above description of DMC is based on calculations of ground states. While the same

approach should work for any state of interest so long as ϕ_n^T is carefully chosen, the excited-state simulations often become unstable because the drift term diverges at the node. As is illustrated in Figure 4.1, when a walker becomes too close to the node $\left|\mathbf{x}'_j - \mathbf{x}_j\right|$ in Eq. (4.6) becomes large, and all of the attempted displacements from this geometry are rejected. For vibrational states with one quantum of excitation, the node passes close to the minimum in the potential, and, when the weights are updated, population will accumulate on walkers that are trapped near the node. In extreme cases, at long times the entire ensemble will localize at a single geometry.

This problem has been identified by Umrigar *et al,*[73] who suggested replacing the drift term for the kth atom, $\vec{D}_k$, with an approximate expression

$$\vec{D}_k^{\text{lim}} = \frac{-\hbar^2 + \hbar\sqrt{\hbar^2 + 2m_k|\vec{D}_k|^2\Delta\tau}}{m_k|\vec{D}_k|^2\Delta\tau}\vec{D}_k \tag{4.10}$$

which will be referred to as the limiting drift term in the following discussion. As defined, $\left|\vec{D}_k^{\text{lim}}\right|$ cannot exceed $\sqrt{2\hbar^2/(m_k\Delta\tau)}$ when $|\vec{D}_k|$ becomes large, while $|\vec{D}_k^{\text{lim}}| \approx |\vec{D}_k|$ at smaller values of $|\vec{D}_k|$. Likewise, the local energy is replaced with its limiting value,

$$E_L^{\text{lim}} = E_{\text{ref}} - (E_{\text{ref}} - E_L)\sqrt{\frac{\sum_k m_k \left|\vec{D}_k^{\text{lim}}\right|^2}{\sum_k m_k \left|\vec{D}_k\right|^2}} \tag{4.11}$$

This correction to the local energy has the effect of setting $E_L^{\text{lim}} = E_{\text{ref}}$ near the node, where $|\vec{D}_k^{\text{lim}}| \ll |\vec{D}_k|$. Further from the node, where $|\vec{D}_k^{\text{lim}}| \approx |\vec{D}_k|$, $E_L^{\text{lim}} \approx E_L$. By approximating E_L by E_{ref} near the node, Ω in Eq. (4.8) becomes one and the amplitude of the wave function remains constant at these geometries. Comparisons of E_L and D to E_L^{lim} and D^{lim} for a one-dimensional harmonic oscillator that models an OH bond with a frequency of 3700 cm^{-1} are provided in Figure 4.1. Except when the walker is close to the node, where the probability amplitude should be close to zero, the approximations provided by Eqs. (4.10) and (4.11) show only small deviations from D and E_L defined in Eqs. (4.4) and (4.3), respectively.

4.2.4 Evaluating Matrix Elements

With ground and excited states calculated, we can obtain the transition frequencies by taking the difference between the energies of these states. The final ingredient that is required for evaluating spectra is determining the intensity, and more specifically matrix elements that involve two different states as

$$I_{0,n} \propto \nu_{0,n} \left|\langle \Psi_0 | \mu | \Psi_n \rangle\right|^2 = \nu_{0,n} |M_{0,n}|^2 \tag{4.12}$$

where $\nu_{0,n}$ is the frequency of the transition between the ground state and the nth excited state, and μ is the dipole moment. The fact that the sampling of the ground and excited states involves distinct sets of geometries greatly complicates the evaluation of matrix elements like that in Eq. (4.12). We previously reported the results of preliminary investigations of how to circumvent these challenges,[33,54,80] which are based on approaches outlined by Barnett *et al.*[84]

To motivate the approaches used in this part of the study, we start by considering how expectation values of multiplicative operators are obtained from DMC calculations. There are several approaches that can be taken to obtain these values. The simplest approach is to exploit the fact that ϕ_n^T provides a good approximation to Ψ_n, and evaluate

$$\langle \Psi_n | O | \Psi_n \rangle \approx \langle \phi_n^T | O | \Psi_n \rangle = \sum_j w_j^{(n)} O\left(\mathbf{x}_j^{(n)}\right) \tag{4.13}$$

Barnett, *et al*[24] as well as Cho and Singer[96] have shown that this approximation can be improved without a substantial increase in computational effort by using

$$\langle \Psi_n | O | \Psi_n \rangle \approx 2\langle \phi_n^T | O | \Psi_n \rangle - \langle \phi^T | O | \phi^T \rangle = 2\sum_j w_j^{(n)} O\left(\mathbf{x}_j^{(n)}\right) - \langle \phi_n^T | O | \phi_n^T \rangle \tag{4.14}$$

This approach for obtaining expectation values can be extended to the evaluation of matrix

elements by multiplying the operator of interest by the ratio of the trial wave functions for the two states. For example to the transition moment between the ground state to the nth excited state, $M_{0,n}$, can be approximated by either

$$\begin{aligned} M_{0,n} \approx M_{0^T,n} &= \langle \phi_0^T | \mu | \Psi_n \rangle \\ &= \left\langle \phi_n^T \left| \mu \left(\frac{\phi_0^T}{\phi_n^T} \right) \right| \Psi_n \right\rangle = \frac{\int f_n(\mathbf{x}) \mu(\mathbf{x}) \left(\frac{\phi_0^T(\mathbf{x})}{\phi_n^T(\mathbf{x})} \right) \mathrm{d}\mathbf{x}}{\int f_n(\mathbf{x}) \mathrm{d}\mathbf{x}} \\ &= \left[\frac{1}{\sum_j w_j^{(n)}(\tau)} \right] \left[\sum_j w_j^{(n)}(\tau) \mu(\mathbf{x}_j^{(n)}(\tau)) \right. \\ &\quad \left. \times \left(\frac{\phi_0^T \left(\mathbf{x}_j^{(n)}(\tau) \right)}{\phi_n^T \left(\mathbf{x}_j^{(n)}(\tau) \right)} \right) \right] \end{aligned} \tag{4.15}$$

or by

$$\begin{aligned} M_{0,n} \approx M_{0,n^T} &= \langle \phi_n^T | \mu | \Psi_0 \rangle \\ &= \left\langle \phi_0^T \left| \mu \left(\frac{\phi_n^T}{\phi_0^T} \right) \right| \Psi_0 \right\rangle = \frac{\int f_0(\mathbf{x}) \mu(\mathbf{x}) \left(\frac{\phi_n^T(\mathbf{x})}{\phi_0^T(\mathbf{x})} \right) \mathrm{d}\mathbf{x}}{\int f_0(\mathbf{x}) \mathrm{d}\mathbf{x}} \\ &= \left[\frac{1}{\sum_j w_j^{(0)}(\tau)} \right] \left[\sum_j w_j^{(0)}(\tau) \mu(\mathbf{x}_j^{(0)}(\tau)) \right. \\ &\quad \left. \times \left(\frac{\phi_n^T \left(\mathbf{x}_j^{(0)}(\tau) \right)}{\phi_0^T \left(\mathbf{x}_j^{(0)}(\tau) \right)} \right) \right] \end{aligned} \tag{4.16}$$

where

$$\int f_n(\mathbf{x}) \mathrm{d}\mathbf{x} = \sum_j w_j^{(n)}(\tau) \tag{4.17}$$

Following the approach for obtaining expectation values,[24] we can combine these expres-

sions to obtain improved approximations to $M_{0,n}$ by using either[84]

$$\langle\Psi_0|\mu|\Psi_n\rangle \approx \frac{1}{2}\left[M_{0^T,n} + M_{0,n^T}\right] = M_{0,n}^{\mathrm{TWF},1} \tag{4.18}$$

or

$$\langle\Psi_0|\mu|\Psi_n\rangle \approx M_{0^T,n} + M_{0,n^T} - M_{0^T,n^T} = M_{0,n}^{\mathrm{TWF},2} \tag{4.19}$$

where

$$M_{0^T,n^T} = \langle\phi_0^T|\mu|\phi_n^T\rangle \tag{4.20}$$

In the above expressions, the TWF superscript is used to indicate that these results are obtained using the Trial Wave Function approach.

In the discussion that follows, ϕ_n^T for $H_3O_2^-$ and $H_5O_2^+$ will be represented as product wave functions that describe the OH stretches and OO stretch. For water, the trial wave function will be formed from one-dimensional functions of the OH bond lengths and in some cases the HOH angle. This approach allows us to focus on the higher-frequency modes or those that will be excited, while not constraining the other large-amplitude vibrational coordinates. In doing this, the matrix elements represented by Eqs. (4.15) and (4.16) reflect integrals over probability amplitudes in those coordinates included in ϕ^T, and integrals over just the wave function for the remaining coordinates. To explore how this approximation affects the evaluation of matrix elements, we recalculated the matrix elements for water, multiplying the integrand by a harmonic approximation to the ground-state wave function in the coordinates that are not included in the definition of ϕ^T.

An alternative approach[80,84] involves evaluating the ratio of Ψ_n and ϕ_n^T in the DMC simulation. This is achieved by using descendant weighting,[23,24] in which the value of Ψ_n/ϕ_n^T at the coordinates of a walker is equated to the number of descendants that can be traced to that walker when the walker is propagated for a predetermined amount of time, $\Delta\tau^{\mathrm{DW}}$, which typically around 250 a.u. These quantities are calculated using continuous weighting,

where

$$\frac{\Psi_{n'}\left(\mathbf{x}_j^{(n)}(\tau)\right)}{\phi_{n'}^T\left(\mathbf{x}_j^{(n)}(\tau)\right)} = \frac{w_j^{(n')}\left(\tau+\Delta\tau^{\mathrm{DW}}\right)}{w_j^{(n)}(\tau)} = d_{n',j}^{(n)}(\tau) \tag{4.21}$$

Here the subscript provides the state that is represented by the descendant weights, while the superscript (n) provides the state that is being represented by the ensemble of walkers at imaginary time τ. For expectation values, $n = n'$, while for matrix elements these two indices will differ. The descendant weighting calculation draws from the observation that $d_{n',j}^{(n)}(\tau)$ provides the value of $\Psi_{n'}/\phi_{n'}^T$ at the coordinates of the jth walker in a simulation of the nth state. This approach is implemented to obtain matrix elements of multiplicative walkers using

$$\begin{aligned}
M_{0,n}^{\mathrm{DW}} &= \frac{\langle\Psi_0\left|\mu\right|\Psi_n\rangle}{\sqrt{\langle\Psi_0|\Psi_0\rangle\langle\Psi_n|\Psi_n\rangle}} \\
&= \frac{\left\langle\Psi_0\left|\mu\left(\frac{\Psi_n}{\phi_n^T}\right)\left(\frac{\phi_n^T}{\phi_0^T}\right)\right|\phi_0^T\right\rangle}{\sqrt{\left\langle\Psi_0\left|\left(\frac{\Psi_0}{\phi_0^T}\right)\right|\phi_0^T\right\rangle\left\langle\Psi_0\left|\left(\frac{\Psi_n}{\phi_n^T}\right)^2\left(\frac{\phi_0^T}{\Psi_0}\right)\left(\frac{\phi_n^T}{\phi_0^T}\right)^2\right|\phi_0^T\right\rangle}} \\
&= \frac{\left\langle\Psi_0\left|\mu\ d_n^{(0)}\left(\frac{\phi_n^T}{\phi_0^T}\right)\right|\phi_0^T\right\rangle}{\sqrt{\left\langle\Psi_0\left|d_0^{(0)}\right|\phi_0^T\right\rangle\left\langle\Psi_0\left|\left(d_n^{(0)}\right)^2\left(d_0^{(0)}\right)^{-1}\left(\frac{\phi_n^T}{\phi_0^T}\right)^2\right|\phi_0^T\right\rangle}}
\end{aligned} \tag{4.22}$$

where the DW superscript indicates that this quantity was obtained using the Descendant Weighting approach. While the descendant weighting approach should provide a more accurate way to evaluate $M_{0,n}$ compared to the trial wave function approach, it suffers from numerical instabilities as when $d_0^{(0)}$ is small, its uncertainty can be proportionally quite large. As Eq. (4.22) requires evaluation of $\left(d_0^{(0)}\right)^{-1}$, these large fractional uncertainties are now affecting large contributions to the second term in the denominator. To address this challenge, for each of the snapshots of the wave function, the descendant weighting calculation is performed multiple times, and we take the average of these values to obtain the values for $d_0^{(0)}$

and $d_n^{(0)}$ that are used to evaluate Eq. (4.22). Since these calculations can require a substantial amount of computer time and storage, the results obtained by averaging 50 to 100 evaluations of the descendant weights are extrapolated to the limit of an infinite number of evaluations by fitting the calculated values of the matrix values as a function of the reciprocal of the number of evaluations of the descendant weights that are performed to a line.

4.3 Results and Discussion

In this study, we use guided DMC simulations to calculate frequencies and intensities of 1-0 vibrational transitions in several systems. We start by exploring the sensitivity of the calculated energies and intensities to the quality of the trial wave function. These comparisons will be made for a harmonic oscillator that models an OH stretching vibration in water. We start by investigating the harmonic oscillator as all of the required integrals can be evaluated analytically. This allows us to separate contributions to any deviations from expected values into those that arise from statistical uncertainties in the DMC simulations and those that come from the approximations used to evaluate matrix elements of the dipole moment. The discussion of the harmonic oscillator will be followed by a description of the trial wave functions that will be used for studies of H_2O, $H_3O_2^-$ and $H_5O_2^+$. We will use the results of calculations on these systems to explore the accuracy and limitations of the approaches for calculating the transition moments, $M_{0,1}$ given by Eqs. (4.18), (4.19) and (4.22). When possible, the results of the DMC calculations will be compared to the results of other calculations that employed the same potential and dipole surfaces.

4.3.1 Sensitivity of Trial Wave Function in Harmonic Oscillator

We start by exploring the sensitivity of the trial wave function approaches for calculating intensities (see Eqs. (4.15)-(4.20)) to the quality of the trial wave function that is used in these calculations. For this part of the study, we focus on a harmonic oscillator that describes an OH bond with a frequency of 3700 cm^{-1}, and approximate the dipole function by the displacement of the oscillator from its equilibrium value, x. For the trial wave function, we

use

$$\phi_n^T(x) \propto \Psi_n(\beta x) \tag{4.23}$$

where β ranges from 0.90 to 0.98, and $\Psi_n(x)$ is the analytic solution for this oscillator. The results of this analysis are provided in Table 4.1.

β^b	1.00^c	0.98	0.95	0.90
E_0 ($/\mathrm{cm}^{-1}$)	1850	1851(1)	1850(1)	1851(1)
E_1 ($/\mathrm{cm}^{-1}$)	5550	5551(1)	5553(1)	5555(1)
$M_{0,1^T}^{(\mathrm{DMC})}$ ($/$Å$)^d$	—	0.06931(15)	0.06907(26)	0.06894(24)
$M_{0,1^T}^{(\mathrm{Exact})}$ ($/$Å$)^{d,e}$	0.06932	0.06930	0.06918	0.06875
$M_{0^T,1}^{(\mathrm{DMC})}$ ($/$Å$)^d$	—	0.07074(0)	0.07297(0)	0.07702(0)
$M_{0^T,1}^{(\mathrm{Exact})}$ ($/$Å$)^{d,e}$	0.06932	0.07072	0.07283	0.07639
$M_{0^T,1^T}$ ($/$Å$)^d$	0.06932	0.07074	0.07297	0.07702
$M_{0,n}^{\mathrm{TWF},1}$ ($/$Å)	0.06932	0.07003(15)	0.07102(26)	0.07299(24)
$M_{0,n}^{\mathrm{TWF},2}$ ($/$Å)	0.06932	0.06931(15)	0.06907(26)	0.06894(24)

[a] The harmonic oscillator models an OH stretch with a harmonic frequency of 3700 cm^{-1}.
[b] β provides the broadening of ϕ^T, see Eq. 4.23.
[c] Expected values of the stated quantity.
[d] For these calculations, $\mu = x$.
[e] See Eqs. 4.25 and 4.26.

Table 4.1: Calculated Energies and Matrix Elements of x for a Harmonic Oscillator[a]

An earlier study[54] demonstrated that this form for the ground-state trial wave function provides an accurate zero-point energy, as is seen in the first row of Table 4.1. Here the energies calculated using DMC range from 1850 to 1851 cm^{-1}, with uncertainties of 1 cm^{-1} based on ten independent DMC simulations. The calculated energies for the first excited state show greater sensitivity to the value of β, although the DMC energies are all within 5 cm^{-1} of the expected value of 5500 cm^{-1} over the reported range of β. The larger deviations in the excited state energy are not surprising given the factor of three increase in the value of the excited state energy compared to that for the ground state. The expected values are provided in the column labeled $\beta = 1$ in Table 4.1.

We next turn our attention to the matrix elements of x, where the expected value is $M_{0,1} = 0.06932$ Å. One advantage of exploring the behavior of the approximate approaches for evaluating $M_{0,1}$ for a harmonic oscillator is that all integrals can be evaluated analytically. For example,

$$M_{0^T,1^T} = \beta \times M_{0,1} \tag{4.24}$$

$$M_{0^T,1} = \sqrt{\frac{8\beta}{(1+\beta^2)^3}} \times M_{0,1} \tag{4.25}$$

$$M_{0,1^T} = \sqrt{\frac{8\beta^3}{(1+\beta^2)^3}} \times M_{0,1} \tag{4.26}$$

In general the values of $M_{0,1^T}$ evaluated using DMC agree with the corresponding exact value, identified by the (Exact) superscript, to within the stated uncertainties. The deviations of $M_{0,n}^{\mathrm{TWF},2}$ from its value at $\beta = 1$ can be accounted for by the changes in the value of $M_{0,1^T}^{(\mathrm{Exact})}$ when β is smaller than 1. As with the excited-state energies, the deviations increase as the value of β is decreased. On the other hand, the calculated values of $M_{0^T,1}$ are unexpected. In all cases, $M_{0^T,1} = M_{0^T,1^T}$ with zero uncertainty. This finding can be traced to the properties of the harmonic oscillator, for which

$$\frac{x\phi_0^T}{\phi_1^T} = \beta \times \sqrt{\frac{\hbar}{2\mu_{\mathrm{OH}}\omega}} = \left\langle \phi_0^T \left| x \right| \phi_1^T \right\rangle \tag{4.27}$$

The results reported in Table 4.1 indicate that for the harmonic oscillator $M_{\mathrm{DMC}}^{\mathrm{TWF},2}$ is more accurate than $M_{\mathrm{DMC}}^{\mathrm{TWF},1}$. This can be traced to the fact that $M_{0,1^T}$ provides a better approximation to $M_{0,1}$ than $M_{0^T,1}$ for this system. The poorer performance of $M_{0^T,1}$ reflects the fact that the range of x over which $\Psi_0 x \Psi_1$ is non-zero is determined by the ground-state wave function as it decays to zero faster than the excited-state wave functions. Replacing Ψ_0 by a broadened trial wave function, increases the range of x over the integrand is non-zero, leading to the deterioration of the accuracy of $M_{0^T,1}$ as an approximation to $M_{0,1}$.

As we move to larger systems, we note that the quality of the matrix elements obtained by the trial wave function approach is sensitive to to the choice of the trial wave function. That noted, even when $\beta = 0.90$ we are able to obtain accurate excited-state energies and intensities. Moving forward, we will utilize trial wave functions that are obtained by solving for the ground- and excited-state solutions based on one- or two-dimensional cuts through the potential surface for the molecule of interest. In this way, we do not need to introduce broadening. We expect that the accuracy of these trial wave functions are comparable to those for which $\beta = 0.98$ in our harmonic oscillator model.

4.3.2 Trial Wave Functions for Molecular Systems

As we move from the harmonic oscillator, to the protonated water dimer, $H_5O_2^+$ we explore how the quality of the trial wave function affects the final results, and how these calculations can be used to obtain insights into couplings in these systems. Specifically, we focus on the vibrational motions that are illustrated in Figure 4.2. These OH stretching vibrations were selected because in all cases the position of the node can be determined by symmetry. While prior knowledge of the position of the node serves to simplify the choice of the trial wave function, this is not a requirement for the approach. As we have shown, there are straightforward approaches for identifying the position of the node when it is not known in advance.[26,33]

In developing the trial wave function for ground state of the OH stretching vibration in water or the outer OH stretching vibrations in $H_3O_2^-$ and $H_5O_2^+$, we found[9,81,82] that the product of one-dimensional wave functions that are obtained by calculating the ground-state solution to a one-dimensional cut through the potential surface for water, developed by Partridge and Schwenke,[85] along one of the OH bonds, with the other two coordinates constrained to their equilibrium values, worked well. These one-dimensional OH wave functions will be denoted $\psi_n(r_{OH})$, where n denotes the number of quanta in the OH stretching vibration. While such a description is sufficient for H_2O, for $H_3O_2^-$ and $H_5O_2^+$ this product of wave functions for the outer OH stretch is multiplied by a two-dimensional function of the

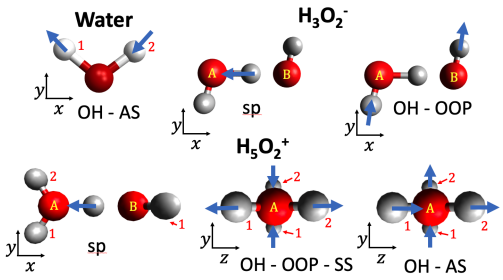

Figure 4.2: The OH vibrational motions explored in this study. The oxygen atoms are labeled as A and B, while the hydrogen atoms are identified with numbers. These labels are used in defining the coordinates. The motions are identified as shared proton (sp) or outer OH stretches (OH) with AS and SS denoting the antisymmetric stretch, symmetric stretch of two OH bonds in a single water molecule, respectively. OOP indicates that the combination of the stretching vibrations in two units are out-of-phase.

displacement of the shared proton and the OO distance. In this way,

$$\phi^{T}_{n_{\mathrm{OH}},n_{\mathrm{sp}}} = \phi^{T,\mathrm{OH}}_{n_{\mathrm{OH}}} \times \phi^{T,\mathrm{sp}}_{n_{\mathrm{sp}}} \tag{4.28}$$

To extend this approach to excited states, we adopt a local mode[97] description for the excited states in the outer OH stretching vibrations. For the asymmetric stretch in water,

$$\phi^{T,\mathrm{OH}}_{n_{\mathrm{OH}}=1}(r_1, r_2) = \left(\frac{1}{\sqrt{2}}\right)\left[\psi_1(r_1)\psi_0(r_2) - \psi_0(r_1)\psi_1(r_2)\right] \tag{4.29}$$

The trial wave function for the out-of-phase OH stretch in $H_3O_2^-$ takes the same form, but is now a function of r_A and r_B, denoting the OH bonds involving oxygen atoms A and B in Figure 4.2. The above definition has the desired property that it will go to zero when the two OH bond lengths are equal. The corresponding trial wave functions for the OH stretching vibrations in $H_5O_2^+$ follows the same principle.

Displacements of the atoms will break the symmetry exhibited by the reference structures. This complicates the definition of the axes needed to determine matrix elements of the Cartesian components of the dipole function. This is achieved by rotating all of the walkers to

an Eckart-embedded axis system, which is based on a high-symmetry reference structure.[1,61] For H_2O reference structure, it is the equilibrium structure. For the $H_3O_2^-$ reference structure, all of the atoms are co-planar, the shared proton is equidistant from the two oxygen atoms, the O-H-O angle is 180°, and the two OH groups are in a trans orientation. For the $H_5O_2^+$ reference structure, the O-H-O angle is 180°, and the shared proton is equidistant from the two oxygen atoms. Additionally, each of the HOH groups are coplanar with the shared proton and the other oxygen atom, while the two HOH groups lie in planes that are perpendicular to each other. This results in a structure with D_{2h} symmetry. All reference structures are shown in Figure 4.2.

4.3.3 Application to Water

The first molecular system that we explore is the water molecule. We use water to determine how the use of reduced-dimensional trial wave functions affects the evaluation of excited-state energies and intensities. To achieve this, we will use two forms for the trial wave function. The first utilizes the product of the two-dimensional stretch wave function, described by Eq. (4.29) and a trial wave function that describes the bending vibration, e.g.

$$\phi^T(r_1, r_2, \theta) = \phi^{T,\mathrm{OH}}_{n_{\mathrm{OH}}}(r_1, r_2)\chi(\theta) \tag{4.30}$$

where $\chi(\theta)$ is a harmonic wave function with $\omega = 1668.46$ cm^{-1}, an effective mass of 2789.72 $m_e \cdot a_0^2$ and an equilibrium HOH angle of 104.508°. We also use only $\phi^{T,\mathrm{OH}}_{n_{\mathrm{OH}}}(r_1, r_2)$. The results of these calculations are reported in the second and third columns of Table 4.2. The results from a previously reported three-dimensional variational calculation[98] using the same potential[85] and dipole surfaces[86] are reported in the rightmost column for comparison.

As can be seen from the results reported in the first row of Table 4.2, the energies for the first excited state, obtained using both trial wave functions, are in excellent agreement with the expected results. Turning our attention to the results of the intensity calculations, we find that both trial wave functions provide intensities that are in good agreement with the

Method	$\phi^T(r_1, r_2, \theta)$	$\phi^{T,\mathrm{OH}}(r_1, r_2)$	$\phi^{T,\mathrm{OH}}(r_1, r_2)(\times\chi(\theta))$	Exact[b]
$E_1 - E_0$ (/cm^{-1})	3755(1)	3755(1)	—	3755
$M_{0,1^T}$ (/D)[c]	0.07808(30)	0.07930(22)	0.07800(11)	
$M_{0^T,1}$ (/D)[c]	0.07480(5)	0.07549(6)	0.07485(5)	0.07640
$M_{0^T,1^T}$ (/D)[c]	0.07755	0.07635	0.07755	
$I_{0,1}^{\mathrm{TWF},2}$ (/km mol^{-1})[d]	53.39(50)	57.91(42)	54.35(22)	
$I_{0,1}^{\mathrm{TWF},1}$(/km mol^{-1})[d]	54.98(26)	56.37(20)	54.97(11)	54.93
$I_{0,1}^{\mathrm{DW}}$(/km mol^{-1})[d]	55.31(18)	55.04(14)	—	

[a] Calculated using the potential and dipole surfaces developed by Partridge and Schwenke.[85,86]

[b] Obtained from a three-dimensional variational calculation.[98]

[c] The x-component of the transition moment used to evaluate $I_{0,1}^{\mathrm{TWF},i}$, see Eq.s 4.16, 4.15, and 4.20.

[d] See Eq.s 4.18, 4.19, and 4.22.

Table 4.2: Calculated Energies and Intensities for the Antisymmetric OH Stretch in H_2O[a]

exact results, although the calculations that utilize the three-dimensional trial wave function, $\phi^T(r_1, r_2, \theta)$, are consistently in better agreement with the exact results than those that use $\phi^{T,\mathrm{OH}}(r_1, r_2)$ for the trial wave function.

One source of the differences between the intensities that are obtained using the two- and three-dimensional trial wave functions in the trial wave function approach comes from the fact that when we use $\phi^{T,\mathrm{OH}}(r_1, r_2)$ the integral in Eq. (4.15) is over the product of ground- and excited-state wave functions for the stretching vibrations and only the ground-state wave function for the bend. The lack of information about the bend in two-dimensional trial wave function can be addressed by multiplying μ in Eqs. (4.15), (4.16) and (4.20) by the harmonic bend wave function, $\chi(\theta)$, when evaluating these matrix elements. Indeed, as the results in the column labeled $\phi^{T,\mathrm{OH}}(r_1, r_2)(\times\chi(\theta))$ indicate, introducing contribution of the bend wave function in this manner yields intensities that are both in good agreement with those obtained using $\phi^T(r_1, r_2, \theta)$ and the exact values.

Focusing on the difference between the values of $I_{0,1}^{\mathrm{TWF},1}$ and $I_{0,1}^{\mathrm{TWF},2}$, we see that $I_{0,1}^{\mathrm{TWF},1}$ provides values for the intensities that are in better agreement with the expected values.

This observation is the opposite of what we found for the harmonic oscillator. The poorer agreement between the calculated value of $I_{0,1}^{\mathrm{TWF,2}}$ and $M_{0,1}^{(\mathrm{Exact})}$ for molecular systems likely reflects the approximations in $M_{0^T,1^T}$, which treats the ground- and excited-state wave functions as being described by a sum of products of one-dimensional wave functions. On the other hand, comparing the values of $M_{0^T,1}$ and $M_{0,1^T}$ to the expected values, we find that the magnitude of the deviations are comparable, albeit with opposite signs. In other words, by taking the average of these quantities we obtain a significant cancellation of errors. While $M_{0,1}^{\mathrm{TWF,1}}$ is the average of $M_{0^T,1}$ and $M_{0,1^T}$, $M_{0,1}^{\mathrm{TWF,2}}$ is the difference between the sum of $M_{0^T,1}$ and $M_{0,1^T}$, and $M_{0^T,1^T}$. This makes $M_{0,1}^{\mathrm{TWF,2}}$ sensitive to errors in $M_{0^T,1^T}$.

A third approximation is provided by the descendant weighing approach. When $\phi^T(r_1, r_2, \theta)$ is used, $I_{0,1}^{\mathrm{DW}}$ is in excellent agreement with both $I_{0,1}^{\mathrm{TWF,1}}$ and the exact value. This gives us confidence in both approaches as we move to systems where we will not be able to directly compare results to those obtained from converged variational calculations. It also provides us with a way to validate the accuracy of the calculated intensities through comparison of the results of the DW and TWF,1 approaches.

4.3.4 Application to $H_3O_2^-$ and $H_5O_2^+$

Next, we turn to $H_3O_2^-$ and $H_5O_2^+$. $H_3O_2^-$ is characterized by a very strong ionic hydrogen bond. In its minimum-energy structure, the shared proton is closer to one of the outer OH groups. On the basis of the potential surface used in this study, the barrier to proton transfer is 74 cm^{-1},[79] which is well below the zero-point energy for this motion. This leads to a very low-frequency shared proton stretching vibration, which has been measured to be 697 cm^{-1} in the $\mathrm{Ar{\cdot}H_3O_2^-}$ complex.[94] In the discussion that follows, we explore the excitation of this vibration as well as the out-of-phase OH stretching vibration involving the outer OH bonds, OH-OOP in Figure 4.2. This vibration has a reported frequency of 3653 cm^{-1}.[99] To explore the role of coupling to other degrees of freedom, we performed a DMC calculation,[100,101] as well as a DVR calculation of the energies and intensities for a four-dimensional model of $H_3O_2^-$. The four vibrational motions that are included in this model are the two outer OH

stretching vibrations, the shared proton motion along the OO bond and the OO distance.

Like $H_3O_2^-$, $H_5O_2^+$ is characterized by a strong ionic hydrogen bond, and the shared proton is midway between the two water molecules in the minimum-energy structure. The shared proton stretching vibration frequency is measured to be 1047 cm^{-1} in the $Ne{\cdot}H_5O_2^+$ complex.[57] This transition appears as a doublet in the spectrum of $Ne{\cdot}H_5O_2^+$ due to an accidental degeneracy between the shared proton stretch and the state with one quantum of excitation in the OO stretch and two quanta in the out-of-phase combination of the two wagging (e.g. umbrella) motions of the outer water molecules.[93] The DMC approaches described above focus on the shared proton stretching vibration, and, in this way, provide the integrated intensity of these two bands. As can be seen in the projections of the probability amplitude for the ground and state with one quantum of excitation in the shared proton stretch shown in Figure 4.3, there is significant coupling between the shared proton stretch and the OO stretching vibration (panels a and b) as well as the wag (panels c and d). In the case of the wag, this vibration corresponds to rotation of one of the water molecules as illustrated in the structure of $H_5O_2^+$ shown above the graphs in Figure 4.3 and denoted by α. As the shared proton shifts toward one of the water molecules, that water molecule will rotate, leading to a nonplanar H_3O^+ structure, which experiences a double-well potential in the wag coordinate. This is most clearly seen in the left part of the projected probability amplitude shown in Figure 4.3d. The increase in the amplitude of both the wagging and OO stretching coordinates with excitation in the shared proton stretch is consistent with the observed coupling between the state with two quanta in the wag and one in the OO stretch with the state with one quantum in the shared proton stretch.

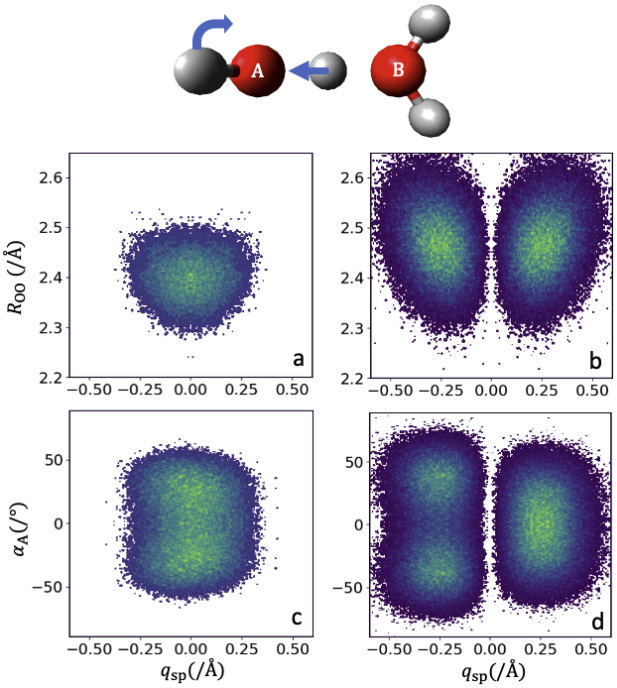

Figure 4.3: Projections of the probability amplitude for the ground state (a and c) and for the state with one quantum of excitation in the shared proton stretch (b and d). In panels a and b, the probability amplitude is projected onto the shared proton displacement, q_{sp} and the distance between the oxygen atoms, R_{OO}. In panels c and d, the the probability amplitude is projected onto the displacement of the wagging motion of the water molecule on the left in the inset at the top, where the wagging vibration is defined as the angle between the OO axis and a vector that is perpendicular to the plane of the water molecule, shifted by 90° so in the structure shown above the figure, $\alpha_{\mathrm{A}} = 0$.

In addition to exploring the shared proton stretching vibration, we calculate the intensities of the out-of-phase symmetric stretch (OH-OOP-SS) and the doubly-degenerate asymmetric stretch (OH-AS) involving the outer OH bonds. These vibrations have reported frequencies of 3603, 3683 cm^{-1} respectively.[57] Note that the in-phase symmetric stretch is totally symmetric so there would be no intensity for transitions to excited states in that mode.

We start by considering the calculated zero-point energies, which are reported in the first rows of Table 4.3. Consistent with previous studies of water clusters[81,82] and protonated water clusters,[9] the zero-point energies obtained using guided DMC for the nine-dimensional description of $H_3O_2^-$ is 6605 cm^{-1}, which agrees with the previously reported unguided DMC results.[79] Likewise, the zero-point energy for the four-dimensional calculation is 4690 cm^{-1}, which agrees well with the results from the DVR calculation using the same model at 4687 cm^{-1}. For $H_5O_2^+$, the zero-point energies obtained using guided DMC is 12 390 cm^{-1} which agrees well with the 12 393 cm^{-1} from the previously reported unguided DMC results.[102] This confirms that employing the trial wave functions for guided DMC works well for calculations of the ground state.

4.3.5 Shared proton motion

We start by considering the frequencies of the shared proton vibrations, q_{sp}. For both $H_3O_2^-$ and $H_5O_2^+$, the frequency of this vibration has been calculated using several computational approaches using the same potential surfaces as are used in the present work.[79,88] Specifically fixed-node DMC calculations have been performed in which the walkers are constrained to one side of the nodal surface, and any walker that crosses the node is removed from the simulation. Given the similarity of the fixed-node approach and the approach used in the present study, it should not be surprising that the difference between the frequencies obtained from these two DMC approaches differ by less than 5 cm^{-1} for both $H_3O_2^-$[80] and $H_5O_2^+$.[57,102] This small difference in vibrational frequencies provides us confidence in our choice of ϕ^T. As noted above, a poor choice of ϕ^T could lead to large errors in the calculated energies, as we

Method	$H_3O_2^-$ Full-D[a] x^d	y^d	$H_3O_2^-$ 4-D[a,b] x^d	y^d	$H_5O_2^+$[c] x^e
$E_0(/\mathrm{cm}^{-1})$[f]	6605(3)		4690(1)		12 390(4)
$E_1 - E_0(/\mathrm{cm}^{-1})$	648(4)		822(1)		991(6)
$M_{0,1^T}$ (/D)	−1.298(14)	0.079(1)	−1.181(6)	0.080(2)	−1.221(11)
$M_{0^T,1}$ (/D)	−1.051(6)	0.074(1)	−1.184(2)	0.081(0)	−0.652(3)
$M_{0^T,1^T}$ (/D)	−1.170	0.071	−1.170	0.071	−0.892
$M_{0,1}^{\mathrm{DW}}$	−1.166(1)	0.115(0.2)	−1.181(14)	0.082(14)	−0.902(58)
$\left\lvert M_{0,1}^{\mathrm{TWF},1}\right\rvert^2$ (/D^2)	1.385(24)		1.404(9)		0.877(14)
$\left\lvert M_{0,1}^{\mathrm{TWF},2}\right\rvert^2$ (/D^2)	1.397(49)		1.436(18)		0.962(28)
$\left\lvert M_{0,1}^{\mathrm{DW}}\right\rvert^2$ (/D^2)	1.373(4)		1.402(4)		0.815(6)

[a] Calculated using the potential and dipole surfaces developed by Huang *et al.*[87]
[b] 4-D DVR calculation gives $E_1 - E_0 = 801$ cm^{-1}, and $M_{0,1} = (-1.185, 0.086)$ D.
[c] Calculated using the potential and dipole surfaces developed by Huang *et al.*[88]
[d] In $H_3O_2^-$, the x-axis is parallel to the OO bond, and the y-axis is in the plane of the ion in the reference structure.
[e] In $H_5O_2^+$, the x-axis is parallel to the OO bond.
[f] Unguided DMC gives 6605 (5) cm^{-1} for $H_3O_2^-$[79] and 12 393(5) for $H_5O_2^+$;[102] 4-D DVR calculation gives 4687.2 cm^{-1} for $H_3O_2^-$.

Table 4.3: Calculated Energies and Transition Strengths for the Shared Proton (sp) Stretch

showed for the harmonic oscillator. Multiconfigurational time-dependent Hartree (MCTDH) and vibrational configuration interaction (VCI) calculations have also been used to explore the energy levels of $H_3O_2^-$[89–91] and $H_5O_2^+$.[92,93] The energy differences between the results of DMC calculations and these approaches are larger, which reflects differences in the treatment of the mode coupling. A summary of the comparison of the calculated energies using DMC, VCI and MCTDH approaches is provided in the Tables 4.4 and 4.5.

	sp		OH-OOP	
Method	$E_1 - E_0$ (/cm^{-1})	$\lvert M_{0,1}\rvert^2$ (/D^2)	$E_1 - E_0$ (/cm^{-1})	$\lvert M_{0,1}\rvert^2$(/D^2)
TWF,2[a]	648	1.397	3612	0.0486
TWF,1[a]	648	1.385	3612	0.0125
DW[a]	648	1.373	3612	0.0146
4D-DVR[b]	801	1.421	3645	0.0009
GSPA[c]	810	0.936	3650	0.0009
Fixed-node DMC - DW[d]	649	0.578	3607	0.0105
VSCF/CI[e]	741	—	3634	—
MCTDH[f]	693	—	—	—
Experimental (Ar)[g]	697	—	3653	—

[a] Present study.
[b] Four-dimensional DVR calculation performed as part of this study.
[c] Approximation from the ground state probability amplitude approach, reported in Ref. 58, 80.
[d] Earlier implementation of descendant weighting using fixed-node DMC using fixed-node DMC reported in Ref. 80.
[e] Vibrational self-consistent field/vibrational configuration Interaction reported in Ref. 91.
[f] Multiconfiguration time-dependent Hartree reported in Ref. 89, 90.
[g] Experimental spectrum of Ar·$H_3O_2^-$ Ref. 94, 99.

Table 4.4: Measured and Calculated Energies and Transition Strengths for $H_3O_2^-$

Method	sp	OH-OOP-SS	OH-AS (1)	OH-AS (2)
Guided DMC[a]	991	3513	3665	3664
Fixed-node DMC[b]	995	3511	3652	3652
GSPA[c]	1050	3586	3693	3719
MCTDH[d]	1033	3614	3689	3689
Experimental (Ne)[e]	1047	3603	3683	3683

[a] Present study.
[b] Fixed-node DMC using no trial wave function reported in Ref. 57, 102.
[c] Ground state probability amplitude reported in Ref. 52.
[d] Multiconfiguration time-dependent Hartree reported in Ref. 92, 93.
[e] Experimental spectrum of Ne·$H_5O_2^+$ reported in Ref. 57.

Table 4.5: Measured and Calculated Frequencies (in cm^{-1}) for $H_5O_2^+$

Next, we turn to the calculations of the transition moments, $M_{0,1}$. For both ions the leading component of the transition dipole moment is along the OO bond, which corresponds to the x direction. Comparing the values of the two non-zero components of $M_{0,1}$ for $H_3O_2^-$ obtained from the trial wave function approach, we find greater variability in the x-component, where the values range from -1.051 D to -1.298 D. When we repeat the DMC calculations using only the four coordinates included in the trial wave function (TWF), the differences among the results obtained using the different approaches is greatly diminished. Indeed, comparing the values of the components of $M_{0,1}$ obtained using the two TWF approaches or the DW approach to the values obtained from the DVR calculation for this four-dimensional model shows near exact agreement. The larger variability among the calculated values of these quantities from the full-dimensional TWF and DW calculations reflects differences in how couplings to other vibrations are treated in these three approximations to $M_{0,1}$.

When the results of the individual calculations of $M_{0,1}$ are combined using Eqs. (4.18) and (4.19) and we compare the squared magnitude of the transition moments, e.g. the transition strengths, we find that the differences among the approaches diminishes. In addition, both the TWF,1 and TWF,2 values are also in good agreement with the results obtained using the DW approach. This improved agreement with the DW approach indicates that differences in individual components of the transition moments calculated using the TWF

and DW approaches reflect a rotation of the transition moment rather than a change in its magnitude. For both the full and four-dimensional calculations, the the TWF,1 approach yields a transition strength that is in better agreement with the results of the DW calculation. Also, when we compare $M_{0^T,1^T}$ to the values of $M_{0^T,1}$ and $M_{0,1^T}$ from the 4D calculation, where there cannot be any couplings to other vibrations, we find that $M_{0^T,1} \approx M_{0,1^T}$, while $M_{0^T,1^T}$ deviates from both of these values. This makes the TWF,1 approximation closer to the DW values of the transition strength when compred to the value obtained using the TWF,2 approximation.

This observation further illustrates the fact that the deterioration of the TWF,2 approach for molecular systems reflects the choice of a a product form for ϕ^T given in Eq. (4.28), which cannot capture important couplings between $q_{\rm sp}$ and other vibrational motions. it is also consistent with what we noted for water and the results for $H_5O_2^+$, which are reported in the rightmost column of Table 4.3.

4.3.6 Outer OH stretches

We next consider the outer OH stretching vibrations, starting with the out-of-phase OH stretching vibration in $H_3O_2^-$, $q_{\rm OH-OOP}$. The results for this vibration are reported in Table 4.6. The vibrational frequency obtained from the guided DMC calculation is in excellent agreement with the previously reported results of fixed-node DMC calculations, which yielded a vibrational frequency of 3607 cm^{-1}.[80] VCI calculations using the same potential provided a slightly larger frequency of 3634 cm^{-1}[191] , while the measured frequency is 3653 cm^{-1} (see Table 4.4).

Comparing the components of the transition moments, we find that the two components have similar sizes, which is consistent with the orientation of the outer OH bonds. We also find larger variability among the calculated values of the components of $M_{0,1}$.

We first consider the x-component of the transition dipole. For this component, the value obtained using the DW approach agrees better with the $M_{0^T,1}$ value from the TWF approach, whereas $M_{0,1^T} \approx M_{0^T,1^T}$. The differences in these two pairs of approximations

	Full-D[b]		4-D	
Method	x^c	y^c	x^c	y^c
Frequency ($/cm^{-1}$)	3612(4)		3633(1)	
$M_{0,1^T}$ (/D)	0.0330(30)	−0.0699(17)	0.0411(20)	0.0280(1)
$M_{0^T,1}$ (/D)	0.1371(98)	−0.0749(74)	0.1195(24)	0.0339(2)
$M_{0^T,1^T}$ (/D)	0.0350	0.0293	0.0350	0.0293
$M_{0,1}^{\mathrm{DW}}$ (/D)	0.1019(56)	−0.0650(128)	−0.0997(160)	0.0328
$\left\lvert M_{0,1}^{\mathrm{TWF},1}\right\rvert^2$ ($/D^2$)	0.0125(8)		0.0074(2)	
$\left\lvert M_{0,1}^{\mathrm{TWF},2}\right\rvert^2$ ($/D^2$)	0.0486(66)		0.0168(11)	
$\left\lvert M_{0,1}^{\mathrm{DW}}\right\rvert^2$ ($/D^2$)	0.0146(15)		0.0110(5)	

[a] Calculated using the potential and dipole surfaces developed by Huang *et al.*[87]
[b] 4-D DVR calculation gives $E_1 - E_0 = 3645$ cm^{-1}, and $M_{0,1} = (0.0079, 0.0256)$ D.
[c] The x-axis is parallel to the OO bond, and the y-axis is in the plane of the ion in the reference structure.

Table 4.6: Calculated Energies and Transition Strengths for the Out-of-Phase OH (OH-OOP) Stretch in $H_3O_2^-$[a]

reflect the treatment of the coupling between the out-of-phase OH stretch and the shared proton displacement, which is enhanced upon excitation of the out-of-phase OH stretch. Indeed, the two calculations that provide the larger value for the x-component of the transition moment use DMC to calculate this excited state, while for the treatments that provide the smaller values the trial wave function is used to describe this excited state. We note that the motion of the shared proton should couple to the outer OH stretch since as the shared proton moves closer to one of the OH groups, the complex evolves from a proton equally interacting with two hydroxide ions to a hydroxide water complex. Since the equilibrium OH bond length is larger in hydroxide than in water, as the shared proton is displaced toward an OH group, that OH bond will shorten. Mixing of these two motions will contribute to the normal mode that describes the shared proton vibration. Conversely, the normal mode that describes the out-of-phase OH stretch will have the shared proton displacing toward the OH bond that is being lengthened. This is illustrated in the projection of $\phi_0^T \psi_1$ onto the shared proton stretch and out-of-phase OH stretch in Figure 4.4b. As illustrated by this

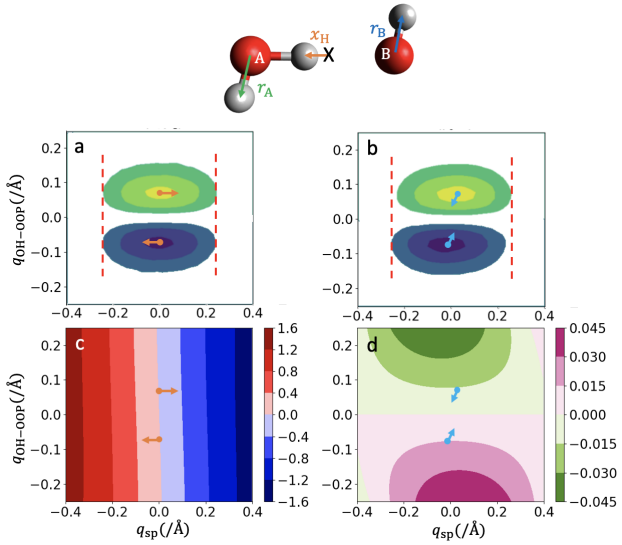

Figure 4.4: Panels a and b, Projections of the product of the ground and excited state wave functions onto the shared proton motion, q_{sp}, and the out-of-phase OH stretch coordinate, $q_{\mathrm{OH-OOP}} = (r_{\mathrm{A}} - r_{\mathrm{B}})/\sqrt{2}$, where this product is approximated by (a) $\Psi_0\phi_1^T$ and (b) $\phi_0^T\Psi_1$. (c) The x-component of the dipole moment and (d) $\mu_x(q_{\mathrm{sp}}, q_{\mathrm{OH-OOP}}) - \mu_x(q_{\mathrm{sp}}, q_{\mathrm{OH-OOP}} = 0)$. The vertical red dashed lines in panels a and b show the maximum extent of the product of the ground and excited state wave functions along q_{sp}. The orange dots in panels a and c are at the maximum and minimum values of these distributions, while the arrows show the direction of the shifts of these positions for $\phi_0^T\Psi_1$ compared to $\Psi_0\phi_1^T$. Likewise, the light blue dots in panels b and d show the maximum and minimum values of the distributions while the arrows indicate the direction they would shift for $\Psi_0\Psi_1$ compared to $\phi_0^T\Psi_1$.

plot, the part of the wave function where $q_{\mathrm{OH-OOP}} > 0$ is shifted to larger values of q_{sp}, while the part with $q_{\mathrm{OH-OOP}} < 0$ is shifted to smaller values of q_{sp}. The illustration above the graphs shows the phases of these vibrations with blue ($q_{\mathrm{OH-OOP}}$) and orange (q_{sp}) arrows. Displacements in the direction of these arrows lead to the shared proton being displaced toward the longer outer OH bond. While this behavior is evident when DMC is used to evaluate the vibrationally excited state, it is not evident in the projection plotted in Figure 4.4a, where the excited state is described by the trial wave function, which is expressed as a product of the ground state in the shared proton vibration and the excited state in the outer OH stretches, as described by Eq. (4.28).

To explore the effect of this coupling on the calculated transition moments, we consider the x-component of the dipole moment, plotted in panels c and d of Figure 4.4. The orange arrows in panels a and c, show the direction of the displacement of the projection of the product of the ground and first excited states when the coupling between q_{sp} and $q_{\mathrm{OH-OOP}}$ is introduced. As seen in panel c, where the x-component of the dipole moment is plotted as a function of these two coordinates, such a shift leads the product of the ground- and excited-state wave functions to sample regions where the magnitude of μ_x is increased. This results in the nearly factor-of-four increase in $M_{0,1}$ when the vibrationally excited state that is used to calculate $M_{0,1}$ is obtained from a DMC calculation. In this way, the calculated value of $M_{0,1^T}$ is expected to provide an underestimation of $M_{0,1}$.

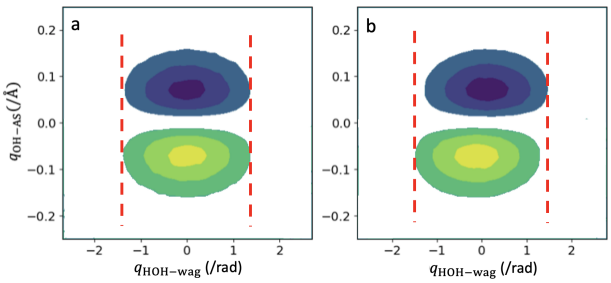

Figure 4.5: Comparison of the projections of products of the ground and first excited state wave functions in the asymmetric stretch, plotted as functions of $q_{\mathrm{HOH-wag}} = \alpha_{\mathrm{A}} + \alpha_{\mathrm{B}} - \pi$ and $q_{\mathrm{OH-AS}}$ for $H_5O_2^+$. Panel a provides results for the product of $\Psi_0\phi_1^T$ and panels b shows results using $\phi_0^T\Psi_1$. Red dashed lines indicate the extent of these distributions. For these plots, α_{A} is defined as the angle between $\vec{r}_{1\mathrm{A}} \times \vec{r}_{2\mathrm{A}}$ and the OO bond, while α_{B} is the angle between $\vec{r}_{1\mathrm{B}} \times \vec{r}_{2\mathrm{B}}$ and the OO bond.

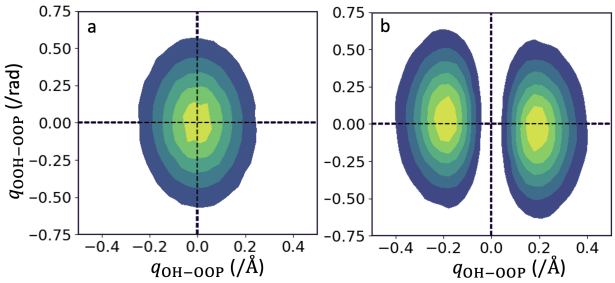

Figure 4.6: Projections of the a) ground state and b) state with one quantum of excitation in the OH-OOP stretch probability amplitudes onto $q_{\mathrm{OH-OOP}} = (r_{\mathrm{A}} - r_{\mathrm{B}})/\sqrt{2}$ and the out-of-phase combination of the two OOH bending vibrations, $q_{\mathrm{OOH-OOP}} = (\theta_{\mathrm{A}} - \theta_{\mathrm{B}})/\sqrt{2}$ for $H_3O_2^-$.

Next we consider panels b and d of Figure 4.4. While the projection in panel b illustrates couplings between q_{sp} and $q_{\mathrm{OH-OOP}}$, the slope of the nodal surface should be finite. The effect of rotating the node on the position of the maximum in the amplitude of the projection is illustrated with blue arrows in panels b and d. As in panel c, panel d provides the x-component of the dipole surface, but to help make it easier to see changes in the values of the dipole moment that is sampled when the excited-state wave function is rotated, we have subtracted the value of the dipole moment when $q_{\mathrm{OH-OOP}} = 0$. As can be seen in Figure 4.4d, the rotation of the excited-state wave function will lead to a decrease in the magnitude of the x-component of the dipole moment in the regions of configuration space where the projection is large. This leads us to expect that $M_{0^T,1}$ provides an overestimation of the magnitude of $M_{0,1}$. Indeed that is what is found when we compare the values of the x-component of the transition moment calculated by applying the DMC approaches for the 4-D model of $H_3O_2^-$ to the values obtained by a basis set calculation of this model system. By using the average of $M_{0,1^T}$ and $M_{0^T,1}$ to approximate $M_{0,1}$ we obtain a partial cancellation of the errors of the individual approximations. Similar behavior is found for the transition moments for the OH-OOP-SS in $H_5O_2^+$, as seen in Table 4.7, and illustrated in Figure 4.5.

Next, we consider the y-component of the transition moment for $H_3O_2^-$. As seen in the results reported in Table 4.6, the DMC calculations consistently provide a value of roughly -0.07 D, while the results based on the 4-D calculation give a value of $+0.03$ D. These differences reflect the coupling between this stretching motion and the out-of-phase OOH bending vibration, $q_{\mathrm{OOH-OOP}}$. This can be seen in the projection of the ground- and excited-state probability amplitude onto $q_{\mathrm{OOH-OOP}}$ and $q_{\mathrm{OH-OOP}}$ in Figure 4.6. The above discussion illustrates how the comparison of transition moments calculated with trial wave functions alone and using DMC can provide insights into important couplings that might not be immediately apparent.

Finally, we consider the asymmetric stretching vibration involving the outer OH bonds in $H_5O_2^+$. This vibration is doubly degenerate, and, as expected, calculations for the two vibrations yield identical results within the statistical uncertainties of the calculations. Because one of the water molecules lies in the xy plane, while the other one is in the xz plane, the magnitudes of the y- and z-components of the transition moment are expected to be identical, and this is what is found. As with the x-component of the out-of-phase OH stretching vibration in $H_3O_2^-$, the calculated values depend on whether the excited state is described using the trial wave function or if it is calculated using DMC. As we found above, such behavior is indicative of couplings between the vibration of interest and another vibrational motion of the same symmetry. An investigation of possible couplings identified the rotations of the two water molecules about their $a-$axes (or the axis in the plane of the water molecules that is perpendicular to the bisector of the HOH angle) to be the motion of interest in this case. We will refer to this vibration as $q_{\mathrm{HOH-wag}}$. Projections of $\Psi_0\phi_1^T$ and $\Psi_1\phi_0^T$ onto this coordinate and the asymmetric stretch are shown in Figure 4.5.

Comparing the transition strengths for the out-of-phase asymmetric OH stretches in $H_5O_2^+$, obtained from the two TWF approaches and the DW approach, we find that in all cases the TWF,1 approach is in better agreement with the DW approach. This is consistent with our findings for water and the sp vibrations in $H_3O_2^-$ and $H_5O_2^+$. It is also consistent with the above analysis that indicated that there is expected to be a partial error cancellation

between the values obtained from $M_{0^T,1}$ and $M_{0,1^T}$.

Before concluding this discussion, it is useful to compare the transition moments to those obtained by approaches other than DMC. While several studies have reported frequencies for $H_3O_2^-$, the only available calculations of intensities were obtained by our group using DMC approaches. Additionally, the spectra for this ion were not reported in a way that allows direct comparison of the intensities of the shared proton and out-of-phase OH stretching vibrations. In contrast, the spectrum for $H_5O_2^+$ has been calculated using the MCTDH approach. The authors report the transition strength of the outer OH stretching vibrations to be roughly 3.5% of that for the shared proton stretch, with both the symmetric and antisymmetric stretching vibrations carrying roughly equal intensity. As with $H_3O_2^-$, the experimental spectrum was recorded in two parts. While we cannot compare the transition strengths for the shared proton and the outer OH stretching vibrations, we can compare the transition strengths of the two vibrations associated with the outer OH stretches. From the action spectrum of $H_5O_2^+$-He,[95] the ratio of the transition strengths for the out-of-phase symmetric stretch to the asymmetric stretch is roughly 1:2. Given that the asymmetric stretch is doubly degenerate, this yields roughly equal transition strengths for these three vibrations. This is consistent with the MCTDH results. Our DW and TWF,1 calculations provide similar relative intensities to those obtained from MCTDH calculations for the asymmetric stretch, with the DW and TWF approaches providing values that are 3.2% and 2.1% of the value for the shared proton stretch, respectively. For the out-of-phase symmetric stretch, our calculated transition strengths are closer to 7.5% of the value for the shared proton stretch. This likely reflects the DMC approaches overestimating the effect of the coupling between this vibration and the shared proton stretch, as is seen when we compare the DMC results to the variational calculation for the 4-D model for $H_3O_2^-$. We expect that the agreement could be improved through the use of a single six-dimensional trial wave function, rather than the product of one- and two-dimensional wave function, but this would come with a significant increase in the computational requirements of the guided DMC calculations.

	OH-OOP-SS	OH-AS (1)		OH-AS (2)	
Method	x^b	y^b	z^b	y^b	z^b
$E_1 - E_0$ (cm^{-1})	3513(7)	3665(4)		3664(5)	
$M_{0,1^T}$ (/D)	−0.205(3)	0.125(4)	0.125(4)	0.124(4)	−0.124(4)
$M_{0^T,1}$ (/D)	−0.309(5)	0.070(2)	0.070(2)	0.073(2)	−0.073(2)
$M_{0^T,1^T}$ (/D)	−0.165	0.127	0.127	0.127	−0.127
$M_{0,1}^{\mathrm{DW}}$ (/D)	−0.242	0.114	0.114	0.114[c]	−0.114[c]
$\left\lvert M_{0,1}^{\mathrm{TWF,1}}\right\rvert^2$ ($/D^2$)	0.066(2)	0.019(1)		0.018(1)	
$\left\lvert M_{0,1}^{\mathrm{TWF,2}}\right\rvert^2$ ($/D^2$)	0.122(5)	0.009(1)		0.008(1)	
$\left\lvert M_{0,1}^{\mathrm{DW}}\right\rvert^2$ ($/D^2$)	0.059(2)	0.026(1)		0.026(1)[c]	
Transition strength,[d] TWF,2	0.126	0.010		0.010	
Transition strength,[d] TWF,1	0.075	0.021		0.022	
Transition strength,[d] DW	0.073	0.032		0.032[c]	
Transition strength,[d] GSPA[e]	0.023	0.034		0.043	
Transition strength,[d] MCTDH[f]	0.035	0.035		0.035	

[a] Calculated using the potential and dipole surfaces developed by Huang *et al.*[88]

[b] The x-axis is parallel to the OO bond, and the water molecules lie in the xy and xz planes in the reference structure.

[c] The magnitudes of these values are taken to be equal to the calculated values for OH-AS(1).

[d] The transition strength divided by the transition strength for the shared proton stretch.

[e] Ref 52.

[f] Ref 92, 93.

Table 4.7: Calculated Energies and Transition Strengths for the Outer OH Stretches in $H_5O_2^+$[a]

4.4 Conclusion

In this study, we explored how guided DMC can be used to calculate the frequencies and intensities of vibrational transitions. We showed that the strategy of expressing ϕ^T as a product of functions that depend on one or two vibrational coordinates, which we previously exploited for ground state calculations, can be extended to calculations involving excited state energies and wave functions. Two approaches for calculating intensities were explored. The first involves using the DW approach used to obtain probability amplitudes. This approach is shown to be accurate, albeit as expensive as the DMC calculation of the energy. In contrast, the TWF approach adds little additional computational expense once the energies have been calculated. By averaging the results of calculations of the transition moment using the TWF approach based on the ground and excited wave functions, accuracy that is comparable to the DW approach is achieved. Additionally, comparisons of the values of the transition moment obtained by these two TWF calculations provide insights into couplings between the vibrational motions.

Chapter 5

DIFFUSION MONTE CARLO CALCULATIONS OF GROUND AND EXCITED VIBRATIONAL STATES USING INTERNAL COORDINATES

Reproduced in part with permission from [Pattrapon Moonkaen, and Anne B. McCoy. Diffusion Monte Carlo calculations of ground and excited vibrational states using internal coordinates. *Molecular Physics*, e2535486] This is an **Original Manuscript** of an article published in Molecular Physics on 24 Jul 2025, available online: https://www.tandfonline.com/doi/full/10.1080/00268976.2025.2535486.

5.1 Introduction

Theoretical and computational approaches for studying vibrational spectroscopy and dynamics are essential for unraveling how molecular structure and couplings among vibrational degrees of freedom are encoded in spectra. Typically, such calculations and the insights that are obtained from them require a careful choice of the vibrational coordinates in which the Hamiltonian is expressed. Indeed, the interpretation of the origin of intensity of vibrational transitions can depend on the coordinates in which the calculation is performed, as has been illustrated for the complex of the chloride ion with a water molecule.[103–105] The choice of coordinates is particularly important when the calculation is performed in reduced dimensionality. Even for full-dimensional calculations, a careful choice of coordinates can make a computationally demanding study tractable.[27,92,106–109]

A method that is particularly powerful for exploring couplings among large amplitude vibrational motions is diffusion Monte Carlo (DMC).[23,24,36,54,110] This approach provides a Monte Carlo sampling of the ground-state wave function as well as the value of the ground-

state energy based on a potential function. As the algorithm involves Monte Carlo sampling of the ground-state wave function based on the potential, most of the expense of the calculation is in the potential evaluations, and the choice of coordinates becomes less critical. On the other hand, if one wishes to perform the calculation in reduced dimensionality, flexibility in coordinate choices, and the ability to manage Hamiltonians with non-separable and coordinate-dependent terms in the kinetic energy operator becomes important. Some work in this direction involved studies of molecular clusters in which the molecular units are kept rigid, and only rotational and translational motions of the molecular constituents are considered.[38,62,111] More recently, we explored complexes of up to three helium atoms with the ammonium/water complex for which we focused only on the motions of the helium atoms and the large amplitude internal rotation of the NH_3 unit.[28] Additionally, Jiang *et al* used DMC approaches to explore the structures of complexes of argon atoms with HF.[29]

The above examples focus on specific cases. To be able to apply DMC more generally using more flexible choices of coordinates requires a more flexible approach. Several years ago, we also explored the possibility of performing DMC simulations in internal coordinates, and showed that this could be achieved by expressing the kinetic energy in terms of linear combinations of the internal coordinates that rendered the kinetic operator separable, at least locally.[60] Since that time, we have recognized that considerable savings in DMC calculations can be achieved through the introduction of guiding functions.[9,36,77,82,112] In the present study we combine these two approaches, and present a reformulation of the working equations for DMC for calculations in internal coordinates that employ guiding functions.

Additionally, while DMC calculations of ground-state properties can be powerful, extensions to excited states are essential as we explore how the couplings among vibrational degrees of freedom evolve with vibrational excitation. We recently presented the results of guided DMC calculations of vibrationally excited states when the position of the nodal surface could be determined by symmetry.[113] In this work, we extend that approach to situations where the location of the node cannot be determined *a priori*.

The above approaches are applied to calculations of water, focusing on the ground state

and states with one quantum of excitation in the HOH bend and the asymmetric OH stretch. Results of these calculations are compared to those obtained from converged variational calculations and to those obtained from DMC calculations performed without guiding functions and using other choices of coordinates.

5.2 Methods

5.2.1 Guided DMC in Cartesian coordinates

Before, presenting an approach for performing guided DMC simulations in internal coordinate, we review some of the key aspects of guided DMC calculations when they are performed in Cartesian coordinates. Additional discussion of the approach can be found in earlier work.[22–24,31,36,54]

As with all studies of quantum dynamics and spectroscopy, we start from the time-dependent Schrödinger equation,

$$i\hbar\frac{\mathrm{d}\Psi_n}{\mathrm{d}t} = \left(\hat{T}+\hat{V}\right)\Psi_n(\mathbf{x}) = -\frac{\hbar^2}{2}\sum_{k=1}^{N_a}\frac{\nabla_k^2\Psi_n(\mathbf{x})}{m_k} + V(\mathbf{x})\Psi_n(\mathbf{x}). \tag{5.1}$$

Developing the guided DMC algorithm involves first replacing t with $\tau = it/\hbar$, and expressing the wave function for the state of interest (represented by n) as

$$\Psi_n(\mathbf{x}) = \frac{f_n(\mathbf{x})}{\phi_n^T(\mathbf{x})}, \tag{5.2}$$

where

$$f_n(\mathbf{x}) = \sum_{l=1}^{N_w} w_l g\left(\mathbf{x}-\mathbf{x}_l\right), \tag{5.3}$$

ϕ_n^T is the pre-determined guiding function, and $g\left(\mathbf{x}-\mathbf{x}_l\right)$ represents a function that is localized at $\mathbf{x}_l$. This function is often referred to as a walker which is represented by its location $\mathbf{x}_l$, and its associate weight, w_l. Finally, N_w provides the number of walkers that make up the ensemble at time τ. Note that here and in the following discussion, the walkers are

identified by the subscript l, while the N_a atoms are indexed by k.

Substituting the expression for Ψ_n in Eq. (5.2) into Eq. (5.1) we obtain[36]

$$\frac{\mathrm{d}f_n}{\mathrm{d}\tau} = \sum_{k=1}^{N_a} \left[\frac{\hbar^2}{2m_k} \nabla_k^2 - \vec{\nabla}_k \cdot \vec{D}_k(\mathbf{x}) \right] f_n(\mathbf{x}) - (E_L(\mathbf{x}) - E_{\mathrm{ref}}) f_n(\mathbf{x}), \tag{5.4}$$

where

$$E_L(\mathbf{x}) = \frac{\hat{H}\phi_n^T(\mathbf{x})}{\phi_n^T(\mathbf{x})} = -\frac{\hbar^2}{2} \sum_{k=1}^{N_a} \left(\frac{1}{\phi_n^T(\mathbf{x})} \right) \frac{\nabla_k^2 \phi_n^T(\mathbf{x})}{m_k} + V(\mathbf{x}) \tag{5.5}$$

is the local energy, and

$$\vec{D}_k(\mathbf{x}) = \frac{\hbar^2}{m_k} \frac{1}{\phi_n^T(\mathbf{x})} \vec{\nabla}_k \phi_n^T(\mathbf{x}) \tag{5.6}$$

provides the drift term for the kth atom. The walkers in Eq. (5.3) are propagated using Eqs. (5.4)-(5.6). More specifically, over a series of time steps, $\Delta\tau$, the propagation is performed in four parts:

First the coordinates of each of the atoms that define each of the walkers are displaced by the sum of a random displacement, represented by $\vec{\delta}_{k,l}$, and $\vec{D}_k(\mathbf{x}_l)$. The components of $\vec{\delta}_{k,l}$ are randomly selected from a Gaussian distribution with width

$$\sigma_k = \hbar \sqrt{\frac{\Delta\tau}{m_k}}, \tag{5.7}$$

and the new coordinates of the kth atom in the lth walker are given by

$$\vec{x}'_{k,l} = \vec{x}_{k,l} + \vec{\delta}_{k,l} + \vec{D}_k(\mathbf{x}_l)\Delta\tau. \tag{5.8}$$

In the Metropolis step, the probability of the move that was taken is compared to the probability that the walker could have been displaced from its new position, $\mathbf{x}'_l$, back to the original one, $\mathbf{x}_l$. Such a displacement would require a random displacement of

$$\vec{\delta}'_{k,l} = \vec{x}_{k,l} - \vec{x}'_{k,l} - \vec{D}_k(\mathbf{x}'_l)\Delta\tau. \tag{5.9}$$

This relative probability is evaluated using

$$\mathcal{P}_l = \frac{P\left(\mathbf{x}'_l \rightarrow \mathbf{x}_l\right)}{P\left(\mathbf{x}_l \rightarrow \mathbf{x}'_l\right)} = \frac{(\phi_n^T(\mathbf{x}'_l))^2}{(\phi_n^T(\mathbf{x}_l))^2} \prod_{k=1}^{N_a} \exp\left[-m_k \left(\left|\delta'_{k,l}\right|^2 - \left|\delta_{k,l}\right|^2\right) / (2\hbar^2 \Delta\tau)\right]. \tag{5.10}$$

If $\mathcal{P}_l$ is larger than a random number between zero and one, then the move is accepted. If the random number is larger than $\mathcal{P}_l$, the move is rejected, and the coordinates of the walker are unchanged.

In the third step, the weights of the walkers are updated so that

$$w_l(\tau) = \exp\left\{-\left[E_L(\mathbf{x}_l) - E_{\text{ref}}(\tau - \Delta\tau)\right]\Delta\tau\right\} w_l(\tau - \Delta\tau). \tag{5.11}$$

For these calculations, we constrain all the weights to be either 1 or 0, To enforce this, the integer part of w_l in Eq. (5.11) provides the number of walkers that will be included in the ensemble at the coordinates $\mathbf{x}_l$, and the fractional part of w_l provides the probability that an additional walker will be introduced at these coordinates. Whether or not the additional walker is introduced is determined by comparing the fractional part of w_l to a random number obtained from a uniform distribution between 0 and 1.[54] We have found that constraining the weights to be 0 or 1 after the displacement produces a more stable simulation than when the weights are represented by real numbers.

Finally, E_{ref} is updated using[31]

$$E_{\text{ref}}(\tau) = \frac{\sum_l E_L(\mathbf{x}_l) w_l(\tau)}{\sum_l w_l(\tau)} - \alpha\left(\frac{\sum_l w_l(\tau) - \sum_l w_l(\tau = 0)}{\sum_l w_l(\tau = 0)}\right), \tag{5.12}$$

where α is a simulation parameter. We have found that $\alpha = 0.5/\Delta\tau$ to be an effective choice for this parameter.[34,35]

Once the simulation is equilibrated, $f_n(\mathbf{x})$ will provide a Monte Carlo sampling of the product of the nth eigenstate of the system of interest and the trial wave function, ϕ_n^T. Likewise, the time-averaged value of E_{ref} provides the energy of the state of interest.

The above approach is general and should provide an accurate wave function and energy for any state of interest, assuming that the choice of ϕ_n^T reflects the expected nodal pattern. In practice excited state simulations often become unstable as both the local energy and drift term involve $1/\phi_n^T$, which diverges at the nodes. This problem has been identified by Umrigar *et al.*,[73] who suggested replacing the drift term and the local energy with limiting expressions. We recently extended the approach for studies of vibrational problems.[113]

5.2.2 Guided DMC in internal coordinates

The primary difference between propagations in Cartesian and internal coordinates comes in the increased complexity of the kinetic energy term in Eq. (5.1). Specifically, in internal coordinates,

$$\hat{T} = -\frac{\hbar^2}{2}\sum_{k=1}^{N_a}\frac{1}{m_k}\nabla_k^2 = -\frac{\hbar^2}{2}\sum_{i,j=1}^{3N_a-6}\frac{\partial}{\partial r_i}G_{ij}(\mathbf{r})\frac{\partial}{\partial r_j} + V'(\mathbf{r}). \tag{5.13}$$

In Eq. (5.13), r_i is used to represent one of the internal coordinates, and G_{ij} is an element of the **G**-matrix, which was introduced by Wilson *et al.*[66] The elements of the **G**-matrix have been tabulated[66,114] or they can be evaluated using

$$G_{ij}(\mathbf{r}) = \sum_{k=1}^{N_a}\frac{\left(\vec{\nabla}_k r_i\right)\cdot\left(\vec{\nabla}_k r_j\right)}{m_k}. \tag{5.14}$$

In this way, the diagonal elements of the **G**-matrix take the role of $1/m_k$ in the Cartesian kinetic energy, although unlike the kinetic energy in Cartesian coordinates, the elements of the **G**-matrix are generally functions of the internal coordinates. Finally, V' is the effective potential operator, which arises from the fact that the coordinates and momenta do not commute. This term can either be obtained from tabulations or calculated.[114]

Replacing the kinetic energy term in Eq. (5.1) with Eq. (5.13), and simplifying the resulting expressions, we obtain a revised set of working equations,

$$\frac{\mathrm{d}f_n}{\mathrm{d}\tau} = \frac{\hbar^2}{2}\sum_{i,j=1}^{3N_a-6}\left\{\frac{\partial}{\partial r_i}G_{ij}(\mathbf{r})\frac{\partial}{\partial r_j} + \frac{\partial}{\partial r_i}D_j(\mathbf{r})\right\}f_n(\mathbf{r}) - \left(E_L(\mathbf{r}) - E_{\mathrm{ref}}\right)f_n(\mathbf{r}), \tag{5.15}$$

where

$$E_L = -\frac{\hbar^2}{2}\sum_{i,j=1}^{3N_a-6}\left(\frac{1}{\phi_n^T(\mathbf{r})}\right)\left(G_{ij}(\mathbf{r})\frac{\partial^2\phi_n^T}{\partial r_i \partial r_j} + \frac{\partial G_{ij}}{\partial r_i}\frac{\partial \phi_n^T}{\partial r_j}\right) + V(\mathbf{r}) + V'(\mathbf{r}) \tag{5.16}$$

is the local energy and

$$D_i(\mathbf{r}) = \left(\frac{\hbar^2}{\phi_n^T(\mathbf{r})}\right)\sum_{j=1}^{3N_a-6}G_{ij}(\mathbf{r})\frac{\partial\phi_n^T}{\partial r_j} \tag{5.17}$$

is the drift term for the ith internal coordinate.

The introduction of internal coordinates leads to two additional complications to the implementation of the DMC algorithm. The first involves the displacement of the walkers since the kinetic energy is no longer separable. Following our earlier work,[60] this can be circumvented by displacing linear combinations of the internal coordinates, which are determined by diagonalizing the **G**-matrix, and evaluating the displacements using a distribution for the Ith linear combination of the internal coordinates of

$$\sigma_I = \hbar\sqrt{\mathcal{G}_I\Delta\tau}, \tag{5.18}$$

where $\mathcal{G}_I$ represents the Ith eigenvalue of the **G**-matrix. This approach assumes that the values of the elements of the **G**-matrix do not change significantly over the random displacement of the walker in a single time step. Earlier work on H_3^+ and its deuterated analogues confirmed this to be a valid assumption for displacements of the cartesian coordinates.[60]

The second complication comes in the Metropolis step. Since $\delta_l^{(r)}$ now represents displacements of internal coordinates, we need to replace the m_k in Eq. (5.10) with $\mathbf{G}^{-1}$, and the revised expression for $\mathcal{P}$ becomes

$$\mathcal{P}_l = \frac{(\phi_n^T(\mathbf{r}'_l))^2}{(\phi_n^T(\mathbf{r}_l))^2} \times \exp\left\{ \sum_{i,j=1}^{3N-6} \left[-\delta_{i,l}^{(r),\prime} \left(G^{-1}\right)_{ij} \delta_{j,l}^{(r),\prime} + \delta_{i,l}^{(r)} \left(G^{-1}\right)_{ij} \delta_{j,l}^{(r)} \right] / \left(2\hbar^2 \Delta\tau\right) \right\}, \quad (5.19)$$

where

$$\delta_{i,l}^{(r)} = r'_{i,l} - \left(r_{i,l} + D_i(\mathbf{r}_l)\right), \quad (5.20)$$

and

$$\delta_{i,l}^{(r),\prime} = r_{i,l} - \left(r'_{i,l} + D_i(\mathbf{r}'_l)\right). \quad (5.21)$$

For each part of the propagation, the **G**-matrix elements are evaluated at a chosen set of internal coordinates. Since the sizes of the displacements of the walkers depend on the values of the elements of the **G**-matrix, they should be evaluated at the coordinates of the walkers prior to displacement. Likewise, the **G**-matrix elements in the drift term in Eq. (5.17) should be evaluated at the same coordinates as are used to evaluate ϕ_n^T. We use the coordinates prior to displacement of the walkers here as well. For the evaluation of E_L in Eq. (5.16), the elements of the **G**-matrix should be evaluated at the same coordinates as the potential energy is evaluated at. The choice becomes less clear when we consider where to evaluate the elements of the **G**-matrix for the Metropolis step, which is given by Eq. (5.19). This question is explored in the following section.

Before moving to the results, it is useful to note the differences between the guided and unguided DMC approaches. Performing DMC simulations without a guiding function is the same as treating ϕ_n^T as a constant. As such, the kinetic contribution to the local energy and the drift term both vanish, and $\delta_{i,l}^{(r)} = \delta_{i,l}^{(r),\prime}$ in Eqs. (5.20) and (5.21), making $\mathcal{P}_l = 1$ for all walkers. For these reasons, in our earlier study,[60] we only needed to consider the evaluation of the **G**-matrix elements for the evaluation of the size of the random displacements of the

walkers.

5.3 Results

To explore the approach, described above, we will focus on DMC simulations of the ground and excited states of water. For these calculations, we use the potential surface developed by Partridge and Schwenke,[85] which is expressed in terms of the two OH bond lengths, $r_{\mathrm{OH},1}$ and $r_{\mathrm{OH},2}$, and the HOH angle, θ. The DMC simulations are performed using the approaches described above with a time step, $\Delta\tau$, of 1 a.u., and $\alpha = 0.5/\Delta\tau$ in Eq. (5.12). All simulations are run for 20 000 time steps, and five independent simulations are run for each calculation. Unless stated otherwise, all ensembles are initiated with 10 000 walkers.

Descendant weighting[23,24,54] is used to generate the probability amplitudes from the ensemble of walkers. For each of these calculations, wave functions are collected every 1000 time steps, starting after the simulation has been propagated for 5000 time steps. Descendant weights are collected after the ensemble of walkers has been propagated for an additional 300 time steps.

Following our earlier work, the guiding functions used in these studies are products of one-dimensional solutions to the Hamiltonian for one of the OH stretching vibrations, $\varphi_n(r)$, where the other OH bond length and the HOH angle are constrained to their equilibrium values, and a harmonic description of the bend. The OH stretching wave functions, evaluated on a grid, and the parameters for the HOH bending wave function have been reported previously.[9]

5.3.1 Ground state energies and wave functions

We start by considering the ground state of water, where

$$\phi_{\mathrm{gs}}^{T}(r_{\mathrm{OH},1}, r_{\mathrm{OH},2}, \theta) = \varphi_0(r_{\mathrm{OH},1})\varphi_0(r_{\mathrm{OH},2})\chi_0(\theta) \tag{5.22}$$

This will allow us to explore the effect of the choice of coordinates at which the elements of the

($\mathbf{G}^{-1}$)-matrix are evaluated on the calculation of the probability of accepting a move through the Metropolis step in Eq. (5.19). Analysis of Eqs. (5.19) - (5.21) indicates that there are four possible choices, the coordinates at either end of the displacement represented by $\delta_j^{(r)}$ or $\delta_j^{(r),\prime}$ or at the middle of this displacement. Focusing on Eq. (5.20) where $\delta_l^{(r)} = \mathbf{r}'_l - (\mathbf{r}_l + \mathbf{D}(\mathbf{r}_l))$, we could evaluate the elements of the ($\mathbf{G}^{-1}$)-matrix at $\mathbf{r}'_l$, at $\mathbf{r}_l + \mathbf{D}(\mathbf{r}_l)$, or at the mean of these two values. To simplify the discussion, these three points will be referred to as the end (e), beginning (b), or mean (m) in the discussion that follows. We also consider using the geometric mean of the elements of $\left(\mathbf{G}^{(b)}\right)^{-1}$ and $\left(\mathbf{G}^{(e)}\right)^{-1}$. The results of calculations of the ground state that employ these four choices in the evaluation of $\mathbf{G}^{-1}$ are provided in the column of Table 5.1, labeled $E_{\rm gs}$. For comparison, the results of DMC simulations in Cartesian coordinates are reported in the bottom row of this table. Previously reported variational calculations using the same potential give a ground state energy of 4636.8 cm^{-1}.[98] This value is in good agreement with the ground state energies obtained when the elements of the ($\mathbf{G}^{-1}$)-matrix are either evaluated at the average coordinates, or when the geometric mean of the elements of the ($\mathbf{G}^{-1}$)-matrix elements that are evaluated at the start and the end of the displacement are used. When employing the geometric mean, care must be taken to ensure that the sign of the geometric mean of the matrix elements matches the sign of the individual elements. Additionally, in some cases the off-diagonal elements of the ($\mathbf{G}^{-1}$)-matrix change sign over the displacement of the walker. In these cases the sign of the geometric mean is selected randomly.

Using ($\mathbf{G}^{-1}$)-matrix elements evaluated at one end of the displacement in the evaluation of $\mathcal{P}$ in Eq. (5.19) introduces errors. This finding should not be surprising as the values of the elements of the ($\mathbf{G}^{-1}$)-matrix depend on the coordinates at which they are evaluated. On the other hand, the 4 cm^{-1} shifts in the ground state energies are an order of magnitude larger than the uncertainties in the calculations.

An important advantage of using guided DMC comes in the savings in terms of the smaller ensemble sizes needed to obtain converged results. We first identified this in our studies of water clusters,[81,82] and identified similar savings for protonated water clusters.[9]

Table 5.1: Comparison of the calculated energies (in cm^{-1}) for the ground state and first excited state in the asymmetric stretch in H_2O[a,b] when $\mathbf{G}^{-1}$ is evaluated at different values of the coordinates, as described in the text.

Calc.	Method[c]	E_{gs}	$E_{n_a=1}(a>0)$	$E_{n_a=1}(a<0)$	$E_{n_a=1}-E_{gs}$ [d]
A	$\left(G^{(b)}\right)^{-1}$	4634.5(0.5)	8385.1(1.6)	8385.4(0.4)	3750.8(1.1)
B	$\left(G^{(e)}\right)^{-1}$	4641.9(0.4)	8399.4(0.7)	8399.5(0.3)	3757.6(0.6)
C[e]	$\sqrt{\left(G^{(b)}\right)^{-1}\left(G^{(e)}\right)^{-1}}$	4639.1(0.4)	8392.7(0.7)	8392.8(0.4)	3753.6(0.7)
D	$\left(G^{(m)}\right)^{-1}$	4638.6(0.4)	8392.8(0.5)	8392.4(0.3)	3754.6(0.6)
E	Cartesian[f]	4637.6(0.4)	8392.3(0.9)		3754.7(1.0)

[a] Calculated using the potential and dipole surfaces developed by Partridge and Schwenke.[85,86]

[b] Numbers in parentheses represent the standard deviation among five independent DMC simulations.

[c] Coordinates at which the elements of $\mathbf{G}^{-1}$ in Eq. (5.19) are defined. See text for details.

[d] The 3D variational calculation on the same potential gives 3755.1 cm^{-1}.[98]

[e] Results when the geometric means of the elements of the $\mathbf{G}^{-1}$ matrices are used.

[f] Results of a DMC calculation performed in Cartesian coordinates.

In Figure 5.1a, we show the evolution of the ground state energy and its uncertainty as a function of $1/N_w$, using the energy obtained from a guided DMC simulation with 10 000 walkers as a reference (gray dotted line). The unguided simulations require ensembles of at least 1000 walkers to obtain results that have an uncertainty below 10 cm^{-1} and where the deviation from the reference value is smaller than this uncertainty. In contrast, the guided DMC calculations achieve this threshold of convergence with as few as 100 walkers.

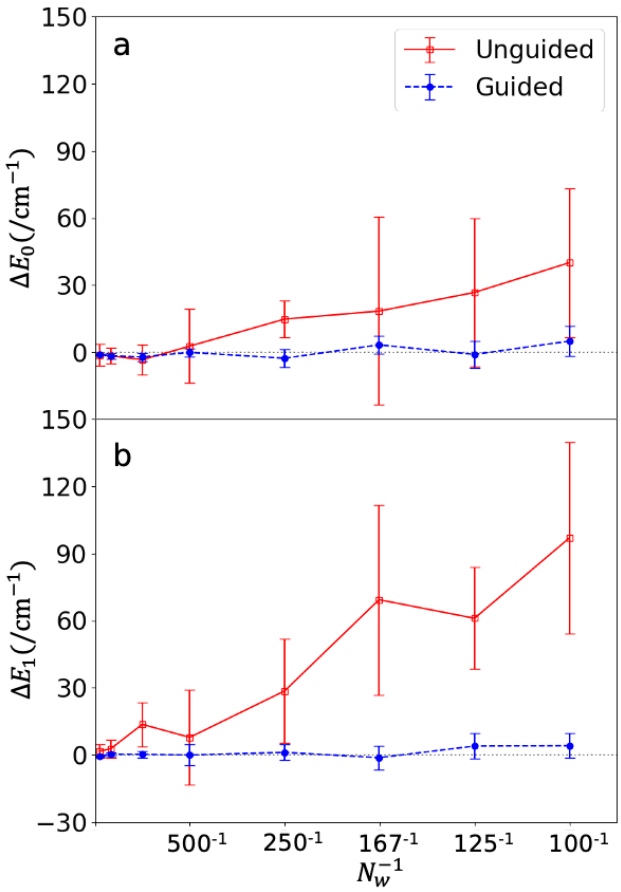

Figure 5.1: Energies obtained from guided (blue dashed lines) and unguided (red solid lines) DMC simulations for the ground state (a) and first excited state in the asymmetric OH stretch (b) in water plotted as a function of $1/N_w$, where N_w represents the number of walkers in the ensemble at $\tau = 0$. The energy obtained from a guided simulation with $N_w = 10\ 000$ is shown with the gray dotted line. The data used to make these plots are provided in Table 5.2. For all of the calculations, the values of $\mathbf{G}^{-1}$ used in the Metropolis step in Eq. (5.19) were evaluated at the center of the displacement, using $\left(\mathbf{G}^{(m)}\right)^{-1}$, as described in the text.

Table 5.2: Data plotted in Figure 5.1

N_w	E_{gs} - Unguided	E_{gs} - Guided	$E_{n_a=1}$ - Unguided	$E_{n_a=1}$ - Guided
100	4679.6(33.2)	4644.6(6.6)	8489.9(42.7)	8397.1(5.5)
125	4666.3(33.1)	4638.6(5.9)	8454.0(22.7)	8396.9(5.7)
167	4658.0(41.9)	4642.9(4.0)	8462.3(42.4)	8391.8(5.4)
250	4654.4(8.2)	4636.9(4.1)	8421.6(23.1)	8394.1(3.5)
500	4642.3(16.6)	4639.5(1.8)	8400.8(21.2)	8393.0(4.7)
1000	4636.3(6.7)	4637.5(1.9)	8406.6(9.8)	8393.3(1.5)
3000	4638.0(3.5)	4638.0(1.3)	8395.7(4.1)	8393.3(0.8)
10 000	4638.4(4.8)	4638.6(0.4)	8394.7(3.1)	8392.4(0.4)

5.3.2 Asymmetric stretch energies and wave functions

We also explored the first excited state in the asymmetric OH stretching vibration. For these calculations, the guiding function is given by

$$\phi^T_{n_a=1} = \frac{1}{\sqrt{2}} \left[\varphi_0(r_{\text{OH},1})\varphi_1(r_{\text{OH},2}) - \varphi_1(r_{\text{OH},1})\varphi_0(r_{\text{OH},2})\right] \chi_0(\theta) \tag{5.23}$$

For this excited state, the wave function changes sign when $r_{\text{OH},1} = r_{\text{OH},2}$, and no further adjustment to the DMC algorithm is needed. The energies obtained using the various approaches for evaluating the elements of the $(\mathbf{G}^{-1})$-matrix are reported in Table 5.1. Since in the DMC simulations walkers that start on one side of the nodal surface will remain on that side of the node, we report two results for each approach, one when the wave function is evaluated for only positive values of the asymmetric stretch coordinate, and one where $a < 0$. The agreement between the results of these two sets of DMC simulations is excellent, as expected, but larger variability is found among the approaches for evaluating the elements of the $(\mathbf{G}^{-1})$-matrix, and we find that using $\left(\mathbf{G}^{(m)}\right)^{-1}$ or the geometric mean of $\left(\mathbf{G}^{(b)}\right)^{-1}$ and $\left(\mathbf{G}^{(e)}\right)^{-1}$ both provide results that are in excellent agreement with the results of DMC simulations performed in Cartesian coordinates and the energy obtained from a variational calculation.[98] This is consistent with our observations for the ground state calculations.

Finally, we compare the convergence of the energies with ensemble size, reported in Figure 5.1. The energies obtained from the guided simulations of the ground state and this excited state show very similar behavior, both in terms of the deviations from the expected values and the size of the uncertainties. In contrast, the convergence of the excited state energy from the unguided simulation is slower, requiring an ensemble size of 3000 walkers to achieve the level of agreement obtained with 1000 walkers for the ground state calculation. This points to the possibility that the savings gained from performing the guided DMC simulation will be larger for excited states than for the ground state.

5.3.3 Bend energies and wave functions

Finally, we consider the first excited state in the HOH bend. For these calculations, we will exploit the fact that we have already determined that for the evaluation of $\mathcal{P}$ in Eq. (5.19) we want to evaluate the elements of the $(\mathbf{G}^{-1})$-matrix at the average geometry of the walker before and after displacement. Unlike the first excited state in the asymmetric stretch, where the position of the node can be determined by symmetry, the position of the node for the bend excited state must be identified, and the quality of the results of the DMC simulation will rely on an accurate determination of the nodal position.

To find the value of θ where we expect the wave function will change sign, we draw from some of our earlier studies and the work of Buch and co-workers,[25,26,55,62] and exploit the fact that we can divide excited states into two or more regions that are separated by the nodal surfaces. Within each region, the sign of the wave function is either positive or negative. Additionally, for each of these regions $\hat{H}\Psi = E\Psi$ and the associated energies must be identical in all of the regions. These observations led us to develop an algorithm in which we sweep the position of the node throughout the DMC simulation.[26] Specifically, after the simulation is equilibrated at the initial value of θ_{node}, the value of θ_{node} is increased linearly through the remainder of the simulation. By using a small value of $\mathrm{d}\theta_{\text{node}}/\mathrm{d}\tau$, the perturbation to the Hamiltonian from the displacement of the position of the node is small, and the ensemble of walkers continues to reflect the ground state under the constraints of the

calculation. Simulations are performed for ensembles for which $\theta > \theta_{\text{node}}$ and $\theta < \theta_{\text{node}}$, and the resulting $E_{\text{ref}}(\theta_{\text{node}})$ curves are fit to low-order polynomials. In the present case, a linear fit is used. The coordinates at which the two curves cross provide the position of the node and the corresponding energy of that excited state. For guided DMC calculations, sweeping the node corresponds to shifting the value of θ where $\chi_1(\theta)$ changes sign. This is achieved by using

$$\phi^T_{\text{n}_\theta=1}(r_{\text{OH},1}, r_{\text{OH},2}, \theta) = \varphi_0(r_{\text{OH},1})\varphi_0(r_{\text{OH},2})\chi_1(\theta - (\theta_e - \theta_{\text{node}})) \tag{5.24}$$

for the trial wave function for these calculations, where θ_e is the minimum in the potential of Partridge and Schwenke,[85] 104.3475°. For these simulations, the value of θ_{node} is shifted between 103° and 106° over 20 000 timesteps of 1 a.u., making $\text{d}\theta_{\text{node}}/\text{d}\tau = 1.5 \times 10^{-4}$ degrees a.u.$^{-1}$. This approach is similar to the approach we developed to obtain excited states from unguided DMC simulations, which we have called adiabatic DMC.[26] The key difference is that in unguided DMC, we require the wave function to go to zero at the node, by removing any walker that crosses the nodal surface from the simulation. In guided DMC the node is enforced by the guiding function, and the drift term in Eq. (5.17) moves amplitude away from the node.

The results of this approach are shown in Figure 5.2. In the simulation represented by the results shown in orange, the wave function is constrained to regions where $\theta < \theta_{\text{node}}$, while the results shown in blue have $\theta > \theta_{\text{node}}$. As we sweep the position of θ_{node}, the value of the energy decreases as the range of angles sampled is increased. We find that the simulation is more stable if the value of θ_{node} is scanned so that the value of E_{ref} decreases through the simulation. In this way, the region that walkers are allowed to explore is expanding. Performing the simulation where E_{ref} increases will lead to some walkers ending up on the incorrect side of the nodal surface, which leads to numerical instabilities in the simulations.

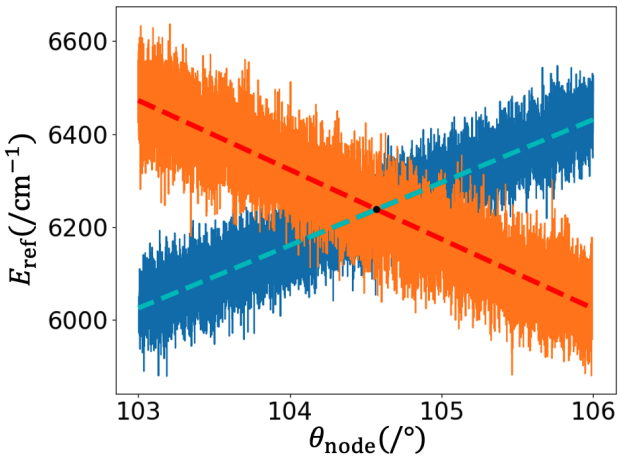

Figure 5.2: Plot of E_{ref} as a function of the position of the node, θ_{node}, for the excited state of water with one quantum in the HOH bend. The data plotted in orange represents calculations where all of the walkers in the ensemble have $\theta < \theta_{\mathrm{node}}$, while the data in blue provides the results for a distribution when $\theta > \theta_{\mathrm{node}}$. Solid lines provide the raw data from the simulations, while the dashed lines give the results of a linear fit to that data. The black circle shows the point where the two dashed lines intersect, and represents the node position and corresponding energy of the state. The fit for the orange data is $E_{\mathrm{ref}}/(\mathrm{cm}^{-1}) = -149.109\,\theta_{\mathrm{node}} + 21830.6$, and the fit for the blue data is $E_{\mathrm{ref}}/(\mathrm{cm}^{-1}) = 135.118\,\theta_{\mathrm{node}} - 7891.49$

We obtain a nodal position of 104.57° and an excited state energy of 1599.5(0.6) cm^{-1} based on five independent calculations of the type shown in Figure 2.1. Using this value of θ_{node}, we also performed ten calculations of the energy of this state, five for $\theta > \theta_{\mathrm{node}}$ and five for $\theta < \theta_{\mathrm{node}}$. These result in a calculated energy for the state with $n_\theta = 1$ of 1596.6(1.1) cm^{-1}. Additionally, the calculations performed when $\theta > \theta_{\mathrm{node}}$ and those performed with $\theta > \theta_{\mathrm{node}}$ differ by roughly 1 cm^{-1}, which is also the uncertainty of these calculations. These results are in excellent agreement with the results of an unguided DMC simulation of the same state, 1592.8(5.7) cm^{-1}, and the expected value of 1594.4 cm^{-1}. The small deviations between these results reflect the assumption that the nodal surface can be defined as a linear function of θ, and as such ignores the curvature in the nodal surface.

5.4 Conclusions

In this work, we described an extension of diffusion Monte Carlo approaches for studying vibrational problems that combines the use of guiding functions with an implementation of DMC in internal coordinates. The working equations for performing DMC simulations in internal coordinates are developed, and the approach is applied to calculations of the ground and excited states of water. The primary challenge of implementing DMC in internal coordinates comes in the coordinate-dependence of the **G**-matrix elements. While we show that assuming the values of the **G**-matrix can be treated as constant, the coordinates at which they are evaluated can affect the results. This sensitivity comes in the evaluation of whether a move is accepted or rejected through the evaluation of $\mathcal{P}$ in Eq. (5.19). We show that by evaluating the elements of the ($\mathbf{G}^{-1}$)-matrix at the center of the displacement that is considered, we are able to obtain accurate energies and wave functions for the ground and excited states of water. Additionally, we extend earlier work that used guided DMC for vibrationally excited states[113] to situations where the position of the node cannot be determined by symmetry considerations alone. This approach was demonstrated for a calculation of the state with one quantum of excitation in the bending vibration in water.

Chapter 6

EXPLORING THE SPECTRAL SIGNATURES OF LARGE AMPLITUDE MOTIONS IN THE CH STRETCHING REGION OF THE VIBRATIONAL SPECTRUM OF CH_5^+

Reproduced in part with permission from [Pattarapon Moonkaen, and Anne B. McCoy. Exploring the Spectral Signatures of Large Amplitude Motions in the CH Stretching Region of the Vibrational Spectrum of CH_5^+. *J. Phys. Chem. A* **2026** , 130 (17), 3361-3369]. Copyright [2026] American Chemical Society.

6.1 Introduction

Methanium, CH_5^+, is a molecular ion of long-standing interest due to both its unusual bonding and its potential astrochemical significance.[10,14–16,115–119] Astrochemical detection of CH_5^+ requires an interpretable spectrum. Despite three reported high-resolution spectra for this ion,[7,44,45] the assignment of more than a fraction of the transitions remains an open challenge. It is reasonable to assume for a small molecule that the development of either accurate calculated rotation-vibration energy levels or a model Hamiltonian that can be used to obtain a simulated spectrum would be straightforward. The challenges that are introduced in the assignment of the spectrum for CH_5^+ reflect the fact that it contains five hydrogen atoms that are bound to a carbon atom with eight valence electrons and, unlike methane, the resulting five CH bonds are not equivalent in the minimum energy geometry.

The equilibrium structure of CH_5^+ can be described as containing a sp^3 hybridized carbon atom with three shorter CH bonds, which are similar in length to the CH bonds in methane, and two elongated CH bonds, which reflect a two-electron, three-centered-bonding interaction between the resulting CH_3^+, or methyl, unit and a hydrogen molecule, or H_2 group.[120] In the

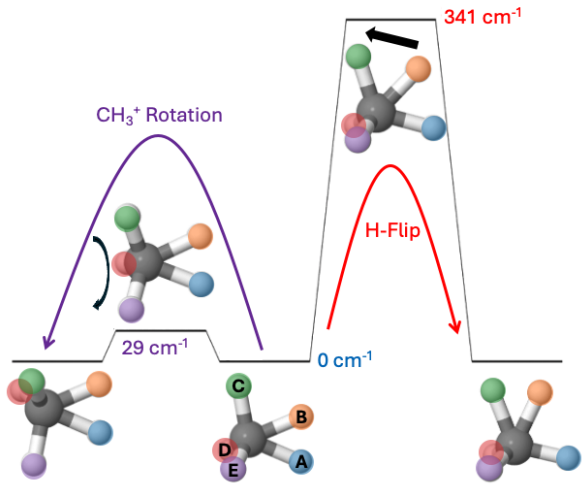

Figure 6.1: Structures of the three low-energy stationary points on the potential surface for CH_5^+. The colored highlight circles are included to illustrate the how the individual hydrogen atoms are displaced through the two isomerization processes. The relative energies of the structures are based on the potential surface of Jin and Bowman.[4]

discussion of the parts of the methanium ion, we will use the names, e.g. methanium, methyl, and hydrogen, when we are describing parts of the ion generically, while chemical symbols will be used when we are considering a specific isotopologue of methanium. Figure 6.1 shows the structures of methanium at the three low-energy stationary points on the potential. The three structures at the bottom of the figure reflect different orientations of the minimum energy structure.

Rotation of the methyl group (which is comprised of the hydrogen atoms shown in green, red and purple in the central depiction of the minimum energy structure) by roughly 60° takes the ion to another minimum on the potential, with the corresponding structure depicted in the lower left of Figure 6.1. The structure at the transition state that connects these minima is shown above these two structures. Further rotation of the methyl group relative to the hydrogen group accesses four additional minimum energy structures. As the barrier for this internal rotation is smaller than the associated rotational constant, the ground-state probability amplitude reflects nearly free internal rotation among the six equivalent minima

that are connected through this motion. This nearly free internal rotation has been identified in simulations of CH_5^+ by us and others,[10–12] where it was shown that the projection of the ground-state probability amplitude onto this torsion coordinate is nearly constant.

The second motion that leads to scrambling of the hydrogen atoms involves a flip motion of the CH bond that involves the orange hydrogen atom. As a result of this motion, the two hydrogen atoms that make up the hydrogen group are now the ones shown in orange and green, while the hydrogen atoms shown in blue, red and purple are now in the methyl group. As illustrated in the right side of Figure 6.1, motion across this transition state results in a pair of 90° rotations of methanium ion. It also transforms the chirality of the ion. Again, the projection of the ground-state probability amplitude for CH_5^+ onto this vibration shows nearly equal amplitude at the potential minimum and at the value of this coordinate that corresponds to the transition state.[11] This pseudorotation will also couple to the molecular rotation, resulting in additional complexity in the rotation-torsion-flip energy level progression. This has led to the difficulty in modeling the rotationally resolved spectrum. Consistent with the above discussion, Asvany *et al.* showed that the most effective treatment has been through a five-dimensional rotor model.[45,121,122] This complexity also introduces significant complications for calculations of the spectrum, and the work of Wang and Carrington represents the best efforts in this area to date.[106,123]

In addition to the rotationally resolved spectra mentioned above, several groups have explored lower-resolution spectra. The earliest of these studies was reported by Boo and Lee more than thirty years ago.[124,125] In these studies, Boo and Lee obtained the spectrum of CH_5^+ complexed with H_2 and other small molecules. They found that as they increased the number of H_2 molecules from one to five, the number of distinct peaks in the spectrum increased from one to three, and the vibrational frequency of the attached H_2 molecule increased from 4077 cm^{-1} to 4109 cm^{-1}, which is still significantly red-shifted from the vibrational frequency of a free hydrogen molecule of 4160 cm^{-1}. This large redshift in the H_2 stretching frequency upon complexation with CH_5^+ indicates that there is a strong interaction between CH_5^+ and H_2. The associated frequencies of the CH vibrations ranged from 2880

to 3070 cm^{-1}, and were assigned to CH vibrations of the CH_3^+ part of the ion with the scrambling of the positions of the hydrogen atoms, illustrated in Figure 6.1 being quenched by the introduction of the H_2 molecules.

Roughly ten years later, Schlemmer and coworkers used a laser-induced reaction approach to obtain lower resolution spectra of CH_5^+ and its isotopologues.[5,6] The detection of vibrational excitation in these studies is based on the observation that proton transfer from CH_5^+ to CO_2 is endothermic, and the energetic difference can be overcome by vibrational excitation. Specifically, vibrational excitation of CH_5^+ was probed by detecting the formation HCO_2^+ from the reaction of CO_2 with CH_5^+. The resulting spectra of CH_5^+ and its deuterated analogues included an intense band that extended from 2200 to 3200 cm^{-1}. We modeled these spectra[7,126] by calculating the harmonic spectra at the stationary points on the potential, and evaluating a weighted sum of the harmonic spectra based on the relative ground-state probability density in the vicinity of each symmetry distinct stationary point. For this analysis, the ground-state probability densities were obtained from diffusion Monte Carlo simulations. At the resolution of those experiments, this relatively simple approach provided surprisingly good agreement with the measured spectra.

More recently, the groups of Ellis[127] and Vilesov[8] reported spectra of CH_5^+ in helium nano-droplets. In their studies, Ellis reported a single broad peak, spanning from 2800 to 3200 cm^{-1}, which is centered at 2966 cm^{-1} with a full width at half maximum of 100 cm^{-1}. This feature is consistent with the previously reported high-resolution spectra,[44,45] and was interpreted to indicate full scrambling of the hydrogen atoms under these conditions. This interpretation is also consistent with computational studies of CH_5^+ complexed with several helium atoms by Marx and co-workers,[128,129] and with the breadth of the CH stretching feature reported by Boo and Lee for the hydrogen tagged experiments.[124,125] Interestingly, the spectrum reported by Vilesov contains a pair of peaks at 2933 and 2984 cm^{-1}. While the spectrum spans roughly the same energy range as the spectrum reported by Ellis, the peaks are narrower than those reported in the Ellis study. In contrast to the work of the Ellis lab who indicate helium droplets with approximately 100 helium atoms and a temperature

of roughly 5 K, the Vilesov experiment has CH_5^+ in droplets containing approximately 10^4 helium atoms and a temperature of 0.4 K. This raised the question of the extent to which the scrambling of the CH bonds in CH_5^+ might be partially quenched in the helium droplet studies.

The simplicity of the helium droplet spectrum obtained by the Vilesov group suggests that it could be reflecting the type of CH stretching transitions one would expect to dominate the spectrum of a less floppy molecule. This led us to consider whether we could model the spectrum and interpret the findings by extending the harmonic oscillator-based model we developed[7,126] in our earlier studies to explore the laser-induced reaction spectra reported by Schlemmer and co-workers.[5,6] In that work, we convoluted the spectra evaluated at the three stationary point geometries using the probability density from diffusion Monte Carlo calculations. However, the DMC approach provides the probability density at all geometries that are sampled in the simulation. As such, we are not limited to considering only stationary points in our analysis. Additionally, the anharmonicity of the CH vibrations should be considered in evaluating the spectrum. In extending the approach taken in our earlier studies, we first consider the full range of structures sampled in a DMC simulation. Starting from these structures, we model the five CH stretching vibrations using a harmonically-coupled anharmonic oscillator (HCAO) model,[37,130] in which the potential is constructed from one-dimensional cuts through the CH_5^+ potential of Jin and Bowman[4] along each of the five CH bonds, along with bilinear couplings involving displacements of pairs of these CH bonds from the minimum in these one-dimensional cuts.

Convoluting these spectra will provide a simple extension of the previous treatment. This will also result in a spectrum that is much broader than observed in the helium droplet spectra. To address these higer-resolution spectra, rather than averaging the spectra obtained from this model, we evaluate the spectra using the combined DMC/HCAO model to generate a Hamiltonian matrix, the elements of which are averaged over the ground-state probability density for the remaining vibrational degrees of freedom.

In the following section, these models will be described in fuller detail. The developed

models will then be used to explore the reported vibrational spectra of CH_5^+ as well as CH_4D^+.

6.2 Methods

In earlier studies of CH_5^+, $HC_2O_4^-$[131] and complexes of $CaOH^+$ and $MgOH^+$ with up to five water molecules,[132] we employed a strategy for evaluating the spectra in the CH or OH stretching region that involved calculating spectra for the isolated CH or OH stretching vibrations over the range of geometries that are sampled ground-state probability density in the lower-frequency vibrations. In the case of CH_5^+, this was achieved by focusing on the harmonic spectra evaluated at the three stationary point structures shown in Figure 6.1. For the other systems, the harmonic spectra in the OH stretching region were averaged over the harmonic ground-state probability density. This was achieved by randomly selecting geometries from the ground-state probability density, minimizing the structures with respect to the OH bond lengths and convoluting the resulting spectra using

$$I(E) \propto \sum_{i=1}^{n_{\rm vib}} \sum_{j=1}^{N_{\rm samp}} \nu_{n_i=1-0}^{(j)} \left| \left\langle \psi_{n_i=1}^{(j)} \middle| \vec{\mu} \middle| \psi_{n_i=0}^{(j)} \right\rangle \Phi_0^2(R_j) \right|^2 \delta(E - \nu_{n_i=1-0}^{(j)}) \tag{6.1}$$

where $n_{\rm vib}$ represents the number of high-frequency vibrations that are included in the calculation of the spectra, and $N_{\rm samp}$ provides the number of geometries, R_j, that are sampled from the ground-state probability density, Φ_0^2. The transition frequency for the ith oscillator at the jth sampled geometry, is represented by $\nu_{n_i=1-0}^{(j)}$, and the associated wave functions are given by $|\psi_{n_i}^{(j)}\rangle$. Note, these wave functions may be mixed in character. For the purpose of analysis, the δ-function in Eq. (6.1) is replaced by a Gaussian function

$$\delta(E - \nu_{n_i=1-0}^{(j)}) \approx \exp\left[-\frac{1}{2} \left(\frac{E - \nu_{n_i=1-0}^{(j)}}{\Delta E} \right)^2 \right] \tag{6.2}$$

with a width ΔE. The approach represented by Eq. (6.1) reflects an adiabatic separation of the high-frequency OH stretching vibrations and the other vibrational motions. It assumes

that the geometry-dependent frequencies of the OH stretching vibrations are unique, allowing us to sum the spectra over the sampled geometries.

As noted above, in earlier studies of CH_5^+ and its deuterated analogues, the sampling was limited to the low-energy stationary points on the potential of Jin, *et al*,[4] where the values of Φ_0^2 were obtained from DMC simulations, and the $|\psi_{n_i}^{(j)}\rangle$ were evaluated using the harmonic approximation. In subsequent studies of $HC_2O_4^-$ and complexes of $CaOH^+$ and $MgOH^+$ with several water molecules, more geometries were sampled and both Φ_0^2 and the $|\psi_{n_i}^{(j)}\rangle$ were evaluated using the harmonic approximation. As we consider extensions of this approach to CH_5^+, we note that anharmonicity of both the high- and low-frequency vibrational motions is important. For this reason, in the present study we use DMC to evaluate Φ_0^2, and randomly sample geometries based on this distribution. The details of the DMC approach,[22–24,32,36,54] and its application to methanium[9] can be found elsewhere. All of the calculations described in this work employ the potential surface for methanium developed by Jin and Bowman,[4] and the DMC calculations were performed using PyVibDMC.[30]

To address the anharmonicities in the CH stretching vibrations, we employ a harmonically coupled anharmonic oscillator (HCAO) model.[37,130] In this model, each CH stretch is treated as an isolated anharmonic oscillator, the potential for which is a one-dimensional cut through the CH_5^+ potential after the potential energy has been minimized with respect to the five CH bond lengths. The energies and wave functions for each CH oscillator are then obtained by solving the corresponding one-dimensional Schrödinger equation in a discrete variable representation (DVR) based on a uniform grid of of 1001 points spanning the CH bond lengths between 1 and 3.8 a_0.[100] The wave functions for the five oscillators are coupled through the quadratic terms in the expansion of the terms for the potential and kinetic energy in the Hamiltonian. In this model, higher-order coupling terms between CH vibrations are found to be small. As such, the wave functions for the CH oscillators are eigenstates of

$$H = \sum_{i=1}^{5} \left[h_i^{1\mathrm{D}} + \sum_{j>i} \left[\frac{\cos\theta_{ij}}{m_{\mathrm{C}}} p_i p_j + F_{ij} \Delta r_i \Delta r_j \right] \right] \tag{6.3}$$

where

$$h_i^{1D} = \frac{p_i^2}{2\mu_{CH}} + V_{1D}^{(i)}(r_i) \tag{6.4}$$

F_{ij} provides the second derivative of the potential with respect to r_i and r_j at the optimized geometry, and θ_{ij} is the H_iCH_j angle. Likewise, the dipole moment, $\vec{\mu}$ in Eq. (6.1), is approximated by the sum of one-dimensional cuts through the dipole surface along each of the CH bonds, evaluated at the optimized values of the other coordinates, $\mathbf{R}_{opt}$,

$$\vec{\mu}(\mathbf{r}) = \sum_{i=1}^{5} (\vec{\mu}(r_i, \mathbf{R}_{opt}) - \vec{\mu}_e) + \vec{\mu}_e \tag{6.5}$$

Terms in the expression of the dipole moment that involve displacements of two or more CH bonds are found to have a small contribution to the spectrum. The orientation of $\vec{\mu}$ is determined using Eckart conditions[1,61] based on the C_{2v} stationary point geometry illustrated in the top right structure of Figure 6.1.

Operationally, the eigenstates of Eq. (6.3) are obtained by first obtaining the eigenstates of one-dimensional Hamiltonians, Eq. (6.4), and using a direct product basis formed from these states to set up the Hamiltonain matrix. Because the Hamiltonian and dipole moment functions are expressed as sums of separable terms that involve the displacement of a single CH bond, this choice of basis leads to efficient evaluation of the matrix elements needed to obtain the various quantities in Eq. (6.1). Additionally, since the coupling terms in the Hamiltonian in Eq. (6.3) are small compared to the anharmonicity of the CH stretching potential, their largest contribution will be in the coupling of basis states with the same total amount of excitation in the CH stretching vibrations. For this reason, the basis used in our analysis includes only the ground state and the five states with one quantum of excitation in one of the CH bonds. The inclusion of more basis functions, as well as higher-order coupling terms in the potential and dipole surface, were found to have little effect on the calculated spectra.

The approach described above is appropriate for describing the low-resolution spectrum

of isolated CH_5^+ ions, where both ionization pathways illustrated in Figure 6.1 are accessible even in the ground state. This renders all five CH bonds equivalent in the vibrational ground state. For the higher-resolution helium droplet spectra, it appears that the spectrum reflects a single vibrational transition (e.g. a single narrow peak) for each of the CH vibrations that could be excited. In this case, the convolution of the sampled spectra, which is the approach that is represented by Eq. (6.1), is no longer appropriate. As a second strategy, we use the results of the evaluation of the CH wave functions and matrix elements of the dipole moment, but rather than calculating separate spectra for each sampled structure, we obtain average values of the elements of the Hamiltonian matrix and of the transition moments. This results in a single transition for each CH oscillator.

This approach is based on two assumptions. First, the five states that correspond to one quantum of excitation in one of the CH oscillators are largely decoupled from the ground state and states with more excitation in the CH stretches. As noted above, because in the HCAO model contains only bilinear couplings between the CH stretching states, the largest contributions from these terms among the CH stretching states will be through their couplings of states with the same amount of excitation in the CH vibrations. The second assumption is that the wave function that describes the seven other vibrations is unchanged between the ground and vibrationally excited states. This second approximation is justified by earlier studies in which we used fixed-node DMC to explore excitations of the CH stretching vibrations in CH_5^+.[133]

One challenge in performing this analysis comes in identifying which CH bond is which as with the low-energy barriers to isomerization the environment that each CH bond experiences will depend on the orientations of the five CH bonds. Additionally, depending on the extent of isomerization that is expected, each structure that is sampled reflects as many as 120 equivalent structures arising from the permutation of hydrogen atoms whose exchange is energetically accessible.

For this reason, for each structure that is sampled, we identify the position of each of the five hydrogen atoms based on the middle minimum-energy structure shown at the bottom of

Figure 6.1. The approach is based on our earlier work on this ion.[11,134] Specifically, the ten distances between the hydrogen atoms are evaluated and the two hydrogen atoms that are involved in the shortest H-H distance are associated with the hydrogen group (the orange and blue hydrogen atoms in the structure in Figure 6.1). The six H-H distances involving the two hydrogen atoms in the hydrogen group are then evaluated. The hydrogen atom in the hydrogen group that is involved in the shortest of these H-H distances in identified as H_B (orange atom), the other atom in the hydrogen group is H_A (blue atom), while the remaining hydrogen atom that is closest to H_B is H_C (green atom). The remaining two hydrogen atoms are randomly assigned as H_D and H_E (red and purple atoms).

These structural identifications take on two roles in the analysis of the spectra in the CH region. When we obtain the Hamiltonian matrix by averaging the Hamiltonian matrices for each sampled geometry, we align the rows and columns based on the A-E labels that identify the CH bond that is excited. Likewise, when we convolute the spectra using Eq. (6.1), it is useful to look at contributions to the spectrum from individual CH oscillators. This is achieved by projecting eigenstates of the Hamiltonian in Eq. (6.3) onto the basis states, which are products of the eigenstates of the h_i^{1D} Hamiltonians in Eq. (6.4). For mixed states, the assignment is made on the basis of the leading contribution to the eigenstate. If two or more eigenstates are identified as having their largest contribution from the same basis state, the eigenstate with the largest contribution from this zero-order state is assigned excitation of that CH bond, and the second-largest contribution is used in the assignment of the other state.

Finally, when obtaining the average values of the elements of the Hamiltonian matrix, care must be taken to ensure that the phases of the wave functions are consistent across calculations, since a change in the phase of one of the wave functions will alter the sign of both the transition moment elements between the ground and excited states and the sign of off-diagonal elements of the Hamiltonian matrix. Additionally, as we consider possible equivalences among CH oscillators, we will average elements of the Hamiltonian matrix as well as the values of the transition moments associated with exchangeable CH bonds. While

the elements of the Hamiltonian matrix are scalars, the transition moments are vector quantities, and the orientations of these vectors depend on the choice of the reference structure used for the Eckart embedding. For these reasons, we have elected to average the magnitude of the transition moments and retain the calculated direction, based on the chosen reference structure.

6.3 Results and Discussion

6.3.1 CH_5^+

To start, we consider the low-resolution spectrum of CH_5^+, which is plotted in gray in Figure 6.2B. The spectrum obtained using the approach described in the previous section is shown with the black trace in Figure 6.2A. Generally, the agreement is good. The calculated spectrum reproduces the overall breadth of the measured trace and the relative intensities of the lower- and higher- frequency features. On the other hand, the calculated spectrum resolves the broad peaks in the experimental spectrum into narrower features. The narrower features seen in the calculated spectrum shown in Figure 6.2A reflect the choice of $\Delta E = 10$ cm^{-1} for convoluting the spectrum (see Eqs. (6.1) and (6.2)). This value is smaller than the breadth of these features that results from the many allowed rotation/torsion/flip transitions in this ion leading to a manifold of excitations for each CH stretching transition. This is expected to result in band contours that are broader than the 10 cm^{-1} value used to generate the calculated spectrum.

In Figure 6.2C, we provide the spectral envelope that was reported in our earlier study, in which we convolute the harmonic spectra obtained at the three stationary points shown in Figure 6.1.[7] In that study, the spectra were convoluted with Gaussians with full-width at half maximum of 200 cm^{-1}. This width better reflects the width of the features in the recorded spectrum, but, as expected, the peaks are all higher in energy than are observed due to the lack of anharmonicity in this calculation.

For each of the sampled structures, we can assign the five CH stretching transitions to

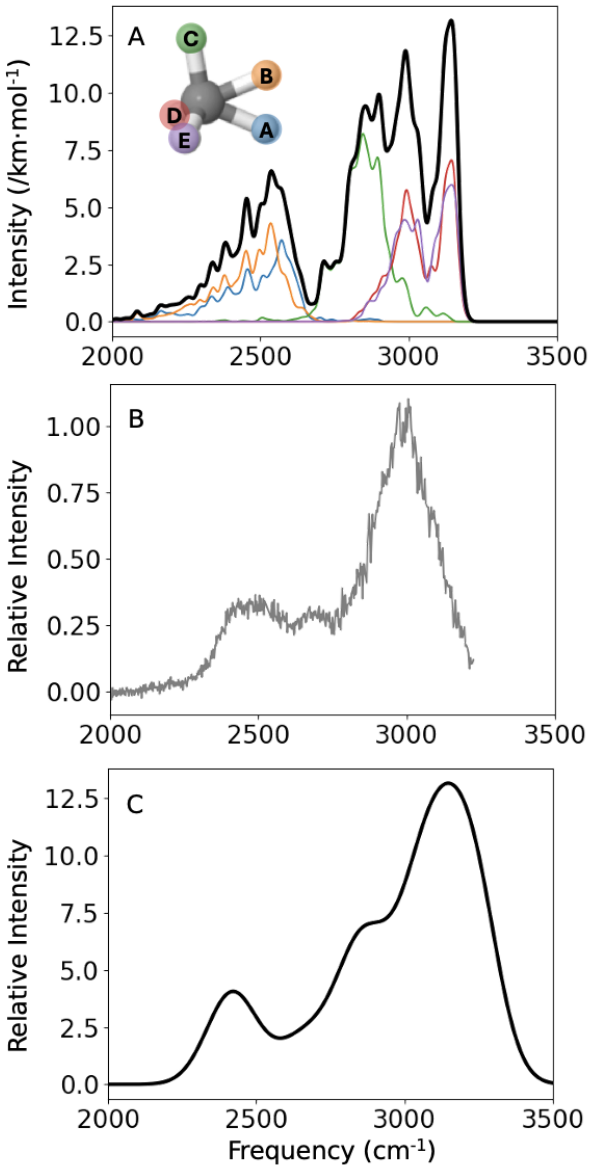

Figure 6.2: Comparison between the calculated and experimental spectra for CH_5^+. (A) Calculated low-resolution spectrum, with individual contributions from each CH bond shown in different colors, where the colors match the colors of the hydrogen atoms in the inset. The black curve is the total spectrum. (B) Low-resolution experimental spectrum from Asvani *et al.*[5,6] (C) Convolution of the harmonic spectra obtained at the three stationary points shown in Figure 6.1, which was reported previously.[7]

individual CH oscillators. In cases in which states are highly mixed in character we assign the transition based on the leading contributions to the wave function, as described above. Once assigned, we can deconvolute the black trace in Figure 6.2A into its contributions from each of the five CH oscillators. These are shown in the traces plotted in green, blue, purple, red and orange in Figure 6.2A, where the corresponding CH bonds in the equilibrium structure are indicated in the inset in the figure. Consistent with earlier studies,[7,126] the peaks that span from 2700 to 3200 cm^{-1} reflect transitions of the CH oscillators that make up the methyl group, while the peak below 2700 cm^{-1}reflects excitations of the CH oscillators that form the hydrogen group. As can be seen, the contributions from the latter two CH bonds are nearly identical, reflecting the near indistinguishability of the CH_A and CH_B bonds. Likewise, the purple and red traces, which reflect contributions from the excitations of the CH bonds involving the hydrogen atoms labeled D and E, are almost identical. This latter observation reflects the fact that these two CH bonds are related by reflection of the ion in the symmetry plane in the reference structure, shown in the inset, making them indistinguishable. The fact that the contributions to the spectrum from these two CH bonds are bimodal is consistent with them contributing in their symmetric and antisymmetric combinations. Finally, the fifth CH oscillator, which is part of the methyl group in the equilibrium structure, but which can exchange with one of the hydrogen atoms in the hydrogen group through the flip vibration that is illustrated in the right side of Figure 6.1, contributes the spectrum shown in green in Figure 6.2A.

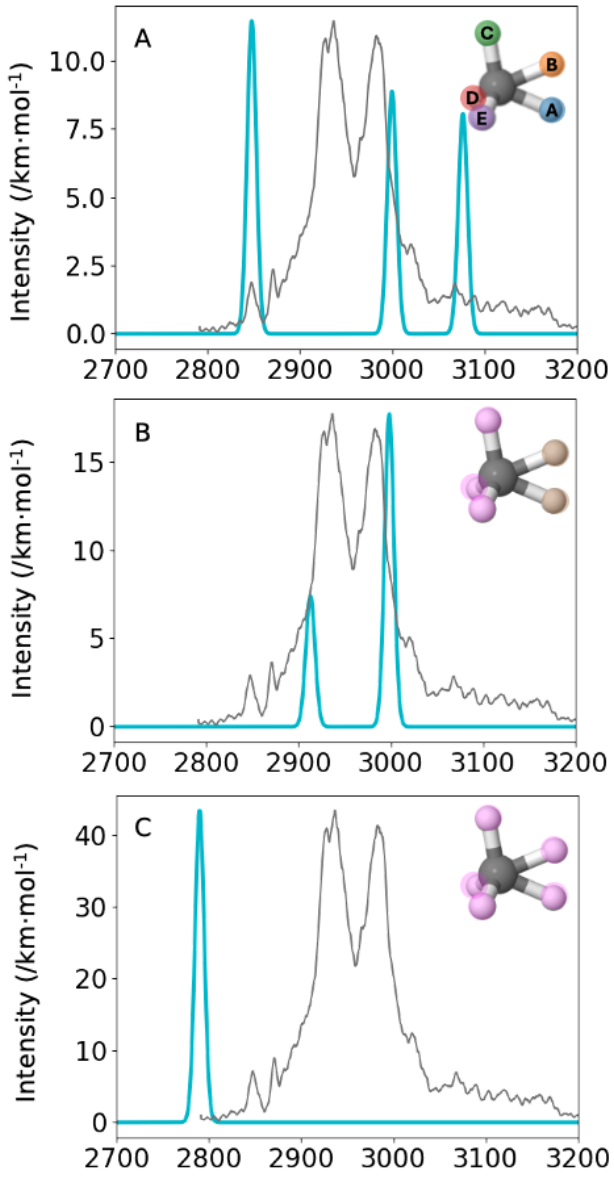

Figure 6.3: Comparison between calculated CH_5^+ spectra (turquoise) and experimental measurements (gray).[8] (A) Calculated high-resolution spectrum obtained when all CH bonds are treated as distinct. (B) Calculated high-resolution spectrum when the CH bonds involving the hydrogen atoms in the hydrogen and methyl groups are made to be equivalent. (C) Calculated high-resolution spectrum when all five CH bonds are made to be equivalent. The calculated peak positions and intensities are reported in Tables 6.1 to 6.3.

Table 6.1: Calculated CH-stretch transition frequencies and intensities with assignments for CH_5^+ high-resolution spectrum when all five CH bonds are treated as distinct.

Frequency (cm^{-1})[a]	Intensity (km mol^{-1})[a]	Assignment
2421.4	65.4	CH_B stretch
2485.2	130	CH_A stretch
2847.9	144	CH_C stretch
2999.8	111	Symmetric CH_D, CH_E stretches
3076.6	101	Asymmetric CH_D, CH_E stretches

[a] When CH bonds involving H_D and H_E are treated as equivalent, the frequencies change by less than 0.1 cm^{-1} and the intensities change by less than 1 km mol^{-1}.

Table 6.2: Calculated CH-stretch transition frequencies and intensities with assignments for CH_5^+ high-resolution spectrum when the CH bonds in the methyl and hydrogen units are treated as equivalent.

Frequency (cm^{-1})[a]	Intensity (km mol^{-1})	Assignment
2436.7	96.0	Symmetric CH_A, CH_B stretches
2484.7	133	Asymmetric CH_A, CH_B stretches
2912.9	92.8	Symmetric CH_C, CH_D, CH_E stretches
2998.3(2)	222	Asymmetric CH_C, CH_D, CH_E stretches

[a] The number in parentheses indicates the degeneracy of the mode.

Table 6.3: Calculated CH-stretch transition frequencies and intensities with assignments for CH_5^+ high-resolution spectrum when all five CH bonds are treated as equivalent.

Frequency (cm^{-1})[a]	Intensity (km mol^{-1})	Assignment
2670.7	1.13	Symmetric CH stretches
2790.1(4)	544	Asymmetric CH stretches

[a] The number in parentheses indicates the degeneracy of the mode.

While it is reassuring to see that the approach can reproduce the lower-resolution spectrum, this has been previously achieved using much simpler approaches.[7] Of greater interest is the helium droplet spectrum, which was recently reported by the Vilesov group.[8] This spectrum has been reproduced in the gray traces in Figure 6.3. As described above, to model this spectrum instead of convoluting the spectra at all of the sampled geometries, we average the elements of the Hamiltonian matrix over all the sampled geometries, taking care to ensure consistent phases of the wave functions. The resulting spectrum is shown in the turquoise trace in Figure 6.3A. The spectrum contains three peaks in this energy range. Two additional peaks are calculated, which have frequencies of 2421.4 and 2485.2 cm^{-1} and intensities that are similar to those for the three peaks in Figure 6.3A. We find that the intensities are in good agreement with the integrated intensities from the low-resolution spectrum. Interestingly, averaging the elements of the Hamiltonian matrix shifts the highest-frequency CH stretching features from 2976 and 3124 cm^{-1} in Figure 6.2A to 3000. and 3077 cm^{-1} in Figure 6.3A, bringing them into better agreement with the peaks at 2933 and 2984 cm^{-1} in the helium droplet spectrum. These two peaks are assigned to the in- and out-of-phase combinations of the CH_D and CH_E stretching vibrations (see Table 6.1 for assignments of all of the peaks in the calculated spectrum).

While the agreement between the measured and calculated spectra is improved, the calculated peaks are still significantly higher in frequency than the reported spectrum. There is also an additional peak in the calculated spectrum at 2748 cm^{-1} that is not seen in the measured one. The above analysis assumes that only the hydrogen atoms shown in purple and red in the inset of Figure 6.3A are equivalent. As noted, analysis of projections of the ground-state probability amplitude for CH_5^+ in isolation shows that the barrier for internal rotation is low. This motion would make the hydrogen atoms shown in green, purple and red hydrogen equivalent. Likewise, the orange and blue hydrogen atoms, which make up the hydrogen group, are also equivalent. We can introduce these equivalences by replacing the elements in the Hamiltonian matrix and the transition moments with the corresponding averaged values over equivalent CH bonds. In Figure 6.3B, the spectrum is recalculated

treating the CH bonds in the methyl group and in the hydrogen group equivalent, while in Figure 6.3C, we provide the results when all five CH bonds are considered equivalent.

As can be seen by comparing the three calculated spectra shown in Figure 6.3, as we move from panel A to panel C, the number of peaks in this energy range decreases from three to one. When the CH bonds in the methyl and hydrogen groups are considered equivalent, the three distinct peaks that correspond to transitions of the CH stretching vibrations in the methyl group become two as the symmetry reflects a symmetric methyl rotor with a single degenerate (A) and doubly degenerate (E) vibration. Making all five CH oscillators symmetrically equivalent further increases the symmetry and now there is a four-fold degenerate asymmetric CH vibration and a singly-degenerate symmetric CH vibration, where the symmetric vibration carries no intensity, by symmetry. In principle, all the components of the degenerate vibrations should have the same intensity. This is not fully achieved due to a combination of numerical noise in the calculation and the use of a reference structure for embedding the body-fixed axis system that does not reflect the high-symmetry of the vibrational ground-state wave function.

Comparing the three approaches for calculating the higher-resolution spectrum to the helium droplet spectrum from the Vilesov group[8] (gray traces in Figure 6.3), we find that the best agreement is achieved in panel B, where only the bonds that are exchanged through internal rotation are treated as equivalent. The splitting between the calculated bands is slightly larger than the reported spectrum, but overall the agreement is quite good. This suggests that in the He nanodroplet, the methyl group retains some rotational freedom, while the flip motion shown on the right side of Figure 6.1 is quenched. This conclusion is consistent with earlier spectroscopic studies on $(HF)_2$,[135] $(HCl)_2$[136] and the vinyl radical.[137] For these systems, it was asserted that the helium environment perturbs the isomerization process through a combination of solvent response to changes in the orientation of the dipole moment and increases in the effective mass associated with the vibration due to interaction with the solvating helium atoms. Focusing on the first of these, the flipping motion, which is shown on the right side of Figure 6.1, leads to a change in the orientation of the dipole moment,

while the internal rotation leads to a much smaller change in overall charge distribution. This combined with the larger barrier for the flipping motion provides a rationalization for this isomerization pathway becoming less important in the helium droplet systems. This contrasts with the results of path-integral studies of smaller complexes of CH_5^+ with up to four helium atoms, which indicate that the scrambling is essentially unperturbed by the interactions with a small number of helium atoms.[128,129]

The above analysis introduces the question of whether the use of a ground-state probability density that allows for permutation of the hydrogen atoms to calculate the spectra reported in Figure 6.3 could be affecting the results of calculations that model spectra in which the flip-isomerization is suppressed. To explore this question, we repeated this analysis, replacing the ground-state probability density for CH_5^+ with the probability density obtained from a ground-state calculation of $CH_2D_3^+$. In earlier studies,[11,138] we found that more than 60% of the ground-state probability density for $CH_2D_3^+$ is localized in the minima in which all three deuterium atoms are in the methyl group. This corresponds to more than six times the expected percentage if all minima were equally populated. When we recalculate the spectrum using the probability density for the part of the ground state of $CH_2D_3^+$ with the deuterium atoms in the methyl group, the resulting spectrum is nearly indistinguishable from the one shown in Figure 6.3B.

The calculated spectra can also be compared to other experiments that probe the cold spectrum. As mentioned above, Boo and Lee[124,125] obtained the spectrum of CH_5^+ complexed with with one to five H_2 molecules, focusing on the high-frequency region between 2700–3200 cm^{-1}. With a single H_2 tag, the spectrum shows a single dominant peak at 2964 cm^{-1}. However, inspection of the line shape reveals small humps on both the low- and high-frequency sides of this peak, suggesting that multiple underlying features contribute to the observed band. Consistent with this interpretation, the authors fitted the spectrum using three Gaussian components centered at 2907, 2965, and 3070 cm^{-1}. As additional H_2 molecules are attached, these three peaks become more clearly separated, with only slight shifts in their frequencies. When compared to our theoretical results, this behavior closely

resembles the three-peak structure obtained in the high-resolution calculation where no hydrogen atoms are treated as equivalent (Figure 6.3A). Consistent with earlier path integral studies,[139] this comparison suggests that in these tagged experiments both isomerization pathways are quenched by the time there are four or five hydrogen molecules attached.

Next, the spectrum reported by Ellis and co-workers[127] consists of a single broad feature centered at 2966 cm^{-1}, with no resolved substructure. This spectrum is similar to the nanodroplet spectrum reported by the Vilesov group, but without the clear separation into two peaks. A possible explanation for this difference is the presence of hot-band contributions, since the Ellis experiment was performed at a higher temperature. When compared to the theoretical spectra, the Ellis spectrum most closely resembles the averaged-Hamiltonian result in which hydrogen atoms within the hydrogen and methyl groups are treated as equivalent (Figure 6.3B). This again supports the interpretation that the nanodroplet environment effectively quenches the H-flip motion, leading to a simplified spectral pattern.

Lastly, we examine whether the use of the full ground-state probability amplitude in the DMC sampling affects the calculation of $\Phi_0^2(R_j)$ in Eq. (6.1), since this quantity should not include the five CH-stretch vibrational degrees of freedom. To test this, we carried out several rigid-body DMC calculations, the results of which are shown in Figure 6.4. In panel A, we show the result obtained from the standard DMC calculation, in which all vibrational degrees of freedom are sampled. In panel B, rigid-body DMC is used with all of the CH bond lengths are 1.1533 Å. This value corresponds to the vibrationally averaged CH bond length obtained from the standard DMC calculation. In panel C, a similar rigid-body DMC approach is used, but the CH bond lengths are determined from the relationship between the CH bond length and the standard deviation of the HH bond lengths established in our previous study.[9] These CH distances are also used to determine the rotational displacement for each walker. Finally, in panel D, the same geometry-dependent CH distances are used not only to determine the rotational displacement, but also to adjust the CH bond lengths in the geometries used for the potential evaluation. Comparison of the four panels shows that the resulting low-resolution spectra differ only slightly. We therefore conclude that the

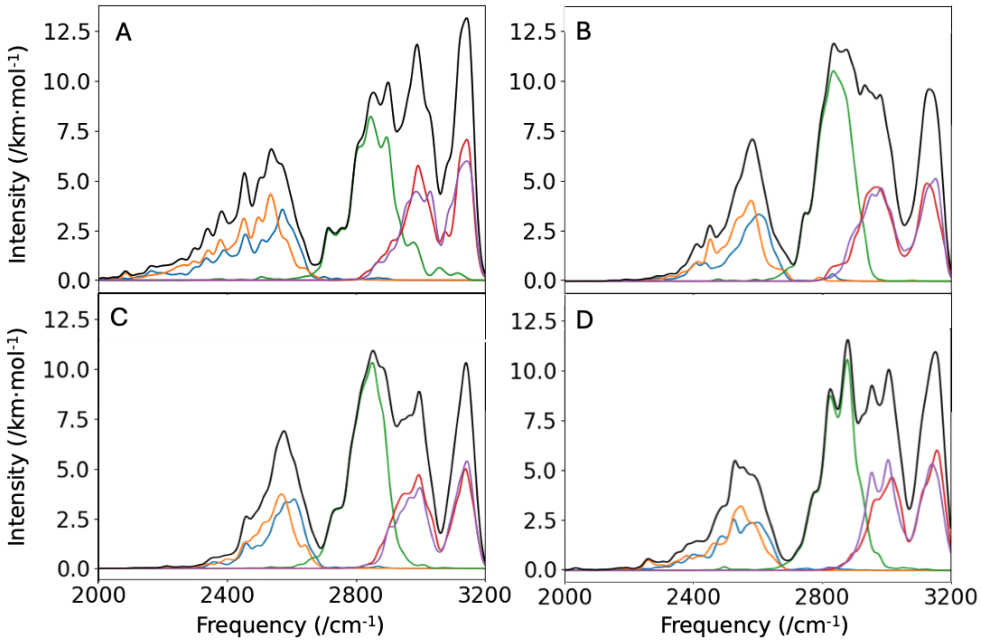

Figure 6.4: Comparison of the calculated low-resolution spectra of CH_5^+ obtained using several DMC approaches. (A) Standard DMC, in which all vibrational degrees of freedom are sampled. (B) Rigid-body DMC, in which all CH bond lengths are fixed at the vibrationally averaged CH bond length. (C) Rigid-body DMC similar to that in panel B, but with the rotational displacements determined from CH bond lengths obtained using the relationship between the CH bond length and the standard deviation of the HH bond lengths.[9] (D) The same approach as in panel C, except that the geometry-dependent CH bond lengths are also used in the potential energy evaluation.

inclusion of the CH-stretching motion in the DMC sampling does not significantly affect the analysis presented above.

6.3.2 CH_4D^+

We now extend the analysis to the singly deuterated isotopologue, CH_4D^+, to examine how deuteration affects the CH-stretch region of the spectrum. The results obtained by convoluting the spectra for individual structures (black curve) can be compared to the low-resolution spectrum, shown in panels A and B of Figure 6.5. As for CH_5^+, the calculated

spectrum shown in Figure 6.5A is decomposed into contributions from the four CH and one CD bond. While the spectrum extends to 1700 cm^{-1}, the intensity below 2000 cm^{-1} is very low.

As expected, the CD stretch appears at a much lower frequency compared to the CH stretches, near 2200 cm^{-1}. The peak that is assigned to the CD stretch, which is plotted in gray and indicated by an asterisk in Figure 6.5A, is much narrower than the contributions from the four CH bonds. This indicates that the deuterium is localized in the methyl part of the ion. Indeed, the most probable position for the deuterium atom is in the methyl group, with this assignment reflecting roughly 92.5% of the ground-state probability density. This is consistent with the earlier finding in our group.[126] This assignment is also reflected in the contributions to the spectrum that correspond to the hydrogen atoms in the D and E positions (red and purple curves). In contrast to CH_5^+, the red curve now contains a single peak. The purple curve appears to have two contributions, although its intensity is suppressed relative to the red curve as would be expected if the deuterium is preferentially in the E-position.

Comparing the calculated spectrum to the low-resolution experimental spectrum, shown in Figure 6.5B, we find that the agreement is good. Both spectra exhibit two broad regions corresponding to excitation of the CH stretches in the hydrogen and methyl groups. The notable difference is that the CD stretch peak is absent in the experimental spectrum. This is expected for an experiment that monitors the mass channel, which corresponding to loss of hydrogen.

The results from modeling the helium droplet spectrum for CH_4D^+ are shown in Figure 6.5C and D. To obtain these spectra, we need to consider the position of the deuterium atom, and set up a separate averaged Hamiltonian matrix based on the position of the deuterium atom. To achieve this, we divide the sampled structures into two groups based on whether the deuterium atom is in the methyl group or in the hydrogen group. In the case that the deuterium is in the methyl group, the deuterium is placed in the E-position (purple in the inset). On the other hand, if the deuterium is in the hydrogen group, it is assigned

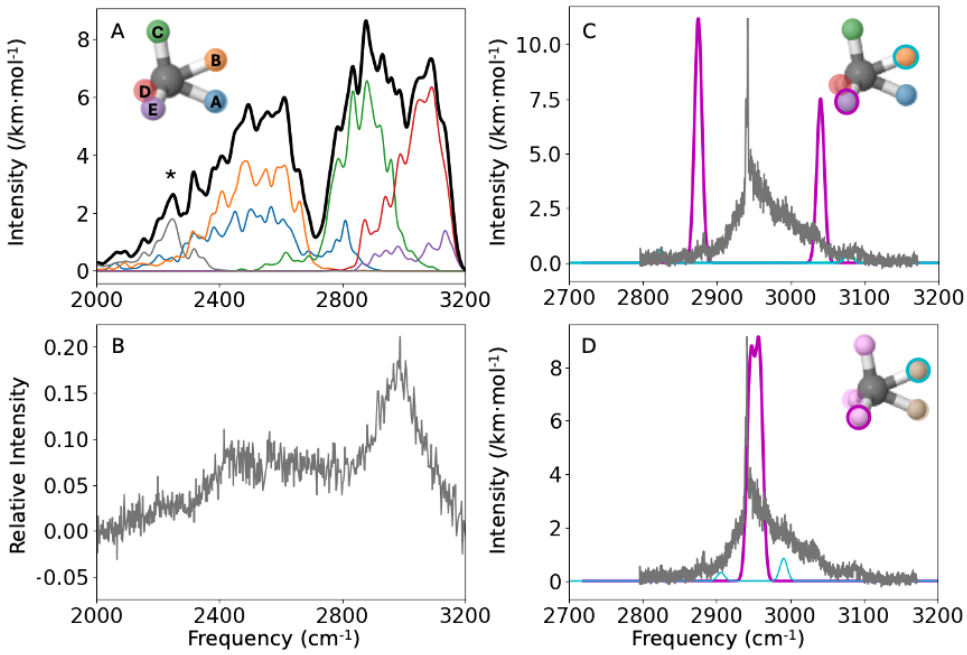

Figure 6.5: Comparison between calculated CH_4D^+ spectra and experimental measurements. (A) Calculated spectrum obtained by convoluting the spectra for the individual structures. The contributions from the CH bonds are shown in the color highlighting the corresponding hydrogen atom. The asterisk (*) and the gray contribution correspond to the CD stretching vibration. (B) Low-resolution experimental spectrum from Asvani *et al.*[5,6] (C) Calculated spectrum obtained by averaging the elements of the Hamiltonian and transition moment matrices. (D) High-resolution experimental spectrum from Singh *et al.*[8] The calculated peak positions and intensities shown in panels C and D are reported in in Tables 6.4 to 6.5.

Table 6.4: Calculated CH and CD-stretch transition frequencies and intensities with assignments for CH_5^+ high-resolution spectrum when the CH bonds are treated as distinct.

Deuterium is in the methyl group (C,D or E positions) and contributes 92.5% of the amplitude in the spectrum

Frequency (cm^{-1})	Intensity (km mol^{-1})	Assignment
2210.8	20.9	CD stretch
2424.3	68.7	CH_B stretch
2496.9	164	CH_A stretch
2874.8	151	CH_C stretch
3040.1	101	CH_D stretch

Deuterium is in the hydrogen group (A or B positions) and contributes 7.5% of the amplitude in the spectrum

Frequency (cm^{-1})	Intensity (km mol^{-1})	Assignment
1841.5	51.9	CD stretch
2476.7	52.3	CH_A stretch
2822.7	103	CH_C stretch
2988.5	2.52	Symmetric CH_D, CH_E stretches
3078.1	104	Asymmetric CH_D, CH_E stretches

to the B-position (orange in the inset). Spectra are calculated based on these two sets of structures and then weighted based on the probability density associated with the position of the deuterium atom. The results of this analysis are shown in Figure 6.5C. The trace shown in magenta reflects the results when the deuterium atom is in the methyl group, and the turquoise trace provides the spectrum that is obtained when the deuterium atom is in the hydrogen group. As expected, the magenta trace, which consists of two peaks between 2700-3200 cm^{-1}, dominates the spectrum. Based on this calculation, there are three additional peaks at 2187.5 cm^{-1} for the CD stretch and 2439.6 and 2510.9 cm^{-1} for the other two CH stretches. The calculated frequencies and intensities obtained from these two calculations are provided in Table 6.4. Compared to the helium nanodroplet spectrum (as shown in gray trace in Figure 6.5C), we can see that neither of the peak frequencies matches the single peak in the spectrum.

Table 6.5: Calculated CH and CD-stretch transition frequencies and intensities with assignments for CH_5^+ high-resolution spectrum when the CH bonds in the methyl and hydrogen units are treated as equivalent.

Deuterium is in the methyl group (C,D or E positions) and contributes 92.5% of the amplitude in the spectrum

Frequency (cm^{-1})	Intensity (km mol^{-1})	Assignment
2219.6	26.7	CD stretch
2432.4	93.2	CH_A, CH_B stretches
2493.1	157	CH_A, CH_B stretches
2946.4	109	CH_C, CH_D stretches
2958.0	114	CH_C, CH_D stretches

Deuterium is in the hydrogen group (A or B positions) and contributes 7.5% of the amplitude in the spectrum

Frequency (cm^{-1})[a]	Intensity (km mol^{-1})	Assignment
1841.7	53.3	CD stretch
2477.6	49.7	CH_A stretch
2906.1	56.3	Symmetric CH_C, CH_D, CH_E stretches
2991.0(2)	153	Asymmetric CH_C, CH_D, CH_E stretches

[a] The number in parentheses indicates the degeneracy of the mode.

To further explore the helium droplet spectrum of CH_4D^+, we recalculate the spectrum, treating the hydrogen atoms in the methyl and hydrogen groups as equivalent. The results of this analysis are shown in Figure 6.5D. While there are still two peaks in the magenta spectrum, the splitting has been reduced from 160 cm^{-1} to 13 cm^{-1}. Comparing this calculated spectrum to the helium nanodroplet spectrum, the agreement is much better, with the position of the peaks lying close to the peak in the experimental spectrum at 2942 cm^{-1}. Additionally, the spectrum obtained when the deuterium is in the hydrogen group provides intensity that is consistent with the longer tail at higher energies and the smaller one at lower energies. This is shown by the turquoise trace in Figure 6.5D. The frequencies and intensities of the peaks in the calculated spectra are provided in Table 6.5. As for CH_5^+, the agreement between the measured and calculated spectra shown in Figure 6.5D suggests that

the flip motion is quenched under nanodroplet conditions, while the internal rotation of the methyl group relative to the hydrogen group remains active.

6.4 Conclusion

We have developed a method for studying the CH stretching region of CH_5^+ and CH_4D^+ by combining diffusion Monte Carlo (DMC) sampling of the ground-state probability density with a harmonically-coupled anharmonic oscillator (HCAO) model for the CH stretches. Using this approach, we first generated spectra by convoluting transitions from the sampled structures, which produced broader features than those observed in the helium-nanodroplet experiments reported by the Vilesov group.[8]

To better reproduce the helium droplet spectra, we applied an alternative approach where the Hamiltonian and transition dipole moment matrices were averaged over all geometries sampled from the DMC ground state probability density. This approach yielded a five-peak pattern, which did not agree with the measured spectrum. When we modified the Hamiltonian to make the hydrogen atoms in the methyl and in the hydrogen groups equivalent, we were able to achieve excellent agreement with experiment. Similar findings are obtained for CH_4D^+.

These results suggest that in the helium-nanodroplet environment, the internal rotation persists, while the H-flip motion is largely quenched. The good agreement between experimental and theoretical spectra demonstrates that our combined DMC/HCAO framework provides a useful way to capture both anharmonicity and hydrogen scrambling effects in CH_5^+ and its isotopologues, and it can likely be extended to other highly fluxional ions.

Chapter 7

CONCLUSION

The work presented in this thesis has focused on the use and development of diffusion Monte Carlo (DMC) for studying vibrational structure in systems that exhibit large-amplitude motion, strong anharmonicity, and delocalized nuclear wave functions. Such systems present challenges for both theory and experiment because their vibrational dynamics cannot be described correctly in terms of small displacements about a single equilibrium geometry. The studies in this thesis have therefore combined methodological developments within the DMC framework with applications to fluxional molecular ions, with the goal of improving both the accuracy of the calculations and the physical interpretation of the resulting spectra.

Chapter 2 reviewed the theoretical foundation of DMC and several of its extensions that are relevant to vibrational problems. In addition to the standard unguided and guided formulations, this chapter summarizes fixed-node approaches for excited states, rigid-body treatments, and calculations involving multiple potential energy surfaces. These methods provide the conceptual basis for the later chapters and illustrate how DMC can be extended beyond the calculation of ground-state energies to problems involving excited states and more flexible coordinate representations.

In Chapter 3, DMC was applied to the ethyl cation, $H^+(C_2H_4)$, and its deuterated analogues. These studies showed that the ground-state wave function is localized near the nonclassical bridged structure where the proton is equidistant from the two carbon atoms, although the motion of the bridging proton remains large in amplitude. Fixed-node DMC calculations of vibrationally excited states were then used to examine the proton-transfer vibration and the CH stretching vibrations and to explore the effects of isotopic substitution

on both the frequencies and the corresponding probability amplitudes. These results clarified how deuteration modifies the extent of delocalization in the wave function and provided a more detailed picture of the vibrational structure of this carbocation.

Chapter 4 developed methods for evaluating infrared intensities using guided DMC wave functions. In this work, both trial-wave-function and descendant-weighting approaches were investigated for calculating transition dipole matrix elements. Applications to model systems, water, $H_3O_2^-$, and $H_5O_2^+$ showed that the trial-wave-function approaches provide a low-cost approximation while the accuracy is still at the same level as the descendant-weighting approach. These studies extended the scope of DMC from the evaluation of vibrational energies and wave functions to the calculation of spectroscopic observables that permit more direct comparisons with experiment.

In Chapter 5, a formulation of guided DMC in internal coordinates was introduced. This development was motivated by the need for coordinate systems that more directly reflect the underlying nuclear motion, particularly in reduced-dimensional studies and in problems for which Cartesian coordinates are not the most natural representation. The resulting working equations were developed for both ground and excited vibrational states, including cases in which the nodal surface cannot be determined by symmetry. Applications to water showed good agreement with Cartesian-coordinate DMC and with converged variational calculations, demonstrating that the method provides a practical and flexible route for extending DMC to new classes of vibrational problems.

Chapter 6 applied these ideas to CH_5^+ and CH_4D^+, systems whose flat potential energy surfaces and highly delocalized wave functions have long made their spectra difficult to interpret. In this work, structures sampled from the DMC ground-state probability density were combined with reduced spectral models to describe the CH stretching region. The resulting calculations reproduced the main features of the reported spectra and provided a physically transparent way to connect fluxional structures with observed spectral patterns. These results also suggested that in helium droplets the isomerization of CH_5^+ is more restricted than in the gas phase.

Taken together, the studies presented in this thesis show that DMC provides more than a means of evaluating ground-state vibrational energies. The developments introduced here extend the method to the evaluation of infrared intensities, to excited-state calculations in internal coordinates, and to the interpretation of spectra in strongly fluxional molecular ions. More broadly, this work demonstrates that DMC can serve as a flexible framework for connecting molecular structure, vibrational dynamics, and spectroscopy in systems for which anharmonicity and delocalization play important roles.

There are several directions in which this work can be extended. The approaches developed here for evaluating intensities and for performing guided DMC calculations in internal coordinates can be applied to other molecular ions and clusters that exhibit strongly coupled or large-amplitude motion. Further improvements in the treatment of excited states, particularly in the construction of nodal surfaces and in the description of couplings among multiple vibrational motions, would expand the range of spectroscopic problems accessible to DMC. In this way, the work presented in this thesis provides both a summary of the progress that has been made and a foundation for future studies of complex vibrational dynamics.

BIBLIOGRAPHY

[1] Louck, J. D.; Galbraith, H. W. *Rev. Mod. Phys.* 1976 *48*, 69–106.

[2] Ricks, A. M.; Douberly, G. E.; v.R. Schleyer, P.; Duncan, M. A. *Chem. Phys. Lett.* 2009 *480*, 17–20.

[3] McCoy, A. B.; Duncan, M. A. *J. Molec. Spect.* 2022 *389*, 111704.

[4] Jin, Z.; Braams, B. J.; Bowman, J. M. *J. Phys. Chem. A* 2006 *110*, 1569–1574.

[5] Asvany, O.; Kumar, P.; Redlich, B.; Hegeman, I.; Schlemmer, S.; Marx, D. *Science* 2005 *309*, 1219–1222.

[6] Ivanov, S. D.; Asvany, O.; Witt, A.; Hugo, E.; Mathias, G.; Redlich, B.; Marx, D.; Schlemmer, S. *Nat. Chem.* 2010 *2*, 298–302.

[7] Huang, X.; McCoy, A. B.; Bowman, J. M.; Johnson, L. M.; Savage, C.; Dong, F.; Nesbitt, D. J. *Science* 2006 *311*, 60–63.

[8] Singh, A.; Allison, S. H.; Azhagesan, A. A. A.; Verma, D.; Vilesov, A. F. *J. Phys. Chem. Lett.* 2024 *15*, 10931–10936.

[9] Finney, J. M.; DiRisio, R. J.; McCoy, A. B. *J. Phys. Chem. A* 2020 *124*, 9567–9577.

[10] Kumar P, P.; Marx, D. *Phys. Chem. Chem. Phys.* 2006 *8*, 573–586.

[11] McCoy, A. B.; Braams, B. J.; Brown, A.; Huang, X.; Jin, Z.; Bowman, J. M. *J. Phys. Chem. A* 2004 *108*, 4991–4994.

[12] Thompson, K. C.; Crittenden, D. L.; Jordan, M. J. T. *J. Am. Chem. Soc.* 2005 *127*, 4954–4958.

[13] Andrei, H.-S.; Solcà, N.; Dopfer, O. *Angew. Chem. Int. Ed.* 2008 *47*, 395–397.

[14] Olah, G. A. *Angew. Chem. Int. Ed.* 1973 *12*, 173–212.

[15] Sefcik, M. D.; Henis, J. M. S.; Gaspar, P. P. *J. Chem. Phys.* 1974 *61*, 4321–4328.

[16] Smith, R. D.; Futrell, J. H. *Chem. Phys. Lett.* 1975 *36*, 545–547.

[17] Sibert, E. L. *J. Chem. Phys.* 1988 *88*, 4378–4390.

[18] Barone, V. *J. Chem. Phys.* 2005 *122*, 014108.

[19] Bowman, J. M. *Acc. Chem. Res.* 1986 *19*, 202–208.

[20] Bowman, J. M.; Christoffel, K.; Tobin, F. *J. Phys. Chem.* 1979 *83*, 905–912.

[21] Ni, Y.; Skinner, J. L. *J. Chem. Phys.* 2015 *143* 014502.

[22] Anderson, J. B. *J. Chem. Phys.* 1975 *63*, 1499–1503.

[23] Suhm, M. A.; Watts, R. O. *Phys. Rep* 1991 *204*, 293 – 329.

[24] Barnett, R.; Reynolds, P.; W.A Lester, J. *J. Comput. Phys.* 1991 *96*, 258 – 276.

[25] Severson, M. W.; Buch, V. *J. Chem. Phys.* 1999 *111*, 10866–10875.

[26] Lee, H.-S.; Herbert, J. M.; McCoy, A. B. *J. Chem. Phys.* 1999 *110*, 5481–5484.

[27] Bacic, Z. *Comp. Phys. Comm.* 2002 *145*, 184–193.

[28] Kelleher, P. J.; Johnson, C. J.; Fournier, J. A.; Johnson, M. A.; McCoy, A. B. *J. Phys. Chem. A* 2015 *119*, 4170–4176.

[29] Jiang, H.; Xu, M.; Hutson, J. M.; Bačić, Z. *J. Chem. Phys.* 2005 *123*, 054305.

[30] DiRisio, R. J.; McCoy, A. B. "rjdirisio/pyvibdmc:1.3.9", 2024, accessed February 16, 2026.

[31] Anderson, J. B. *J. Chem. Phys.* 1976 *65*, 4121–4127.

[32] McCoy, A. B. *Int. Rev. Phys. Chem.* 2006 *25*, 77–107.

[33] Finney, J. M.; DiRisio, R. J.; McCoy, A. B. Diffusion Monte Carlo Approaches for Studying Large Amplitude Vibrational Motions in Molecules and Clusters. In *Vibrational Dynamics of Molecules*; Bowman, J. M., Ed.; World Scientific: 2022.

[34] Petit, A.; McCoy, A. B. *J. Phys. Chem. A* 2009 *113*, 12706–12714.

[35] Barone, V.; Alessandrini, S.; Biczysko, M.; Cheeseman, J. R.; Clary, D. C.; McCoy, A. B.; DiRisio, R. J.; Neese, F.; Melosso, M.; Puzzarini, C. *Nat. Rev. Methods Primers* 2021 *1*, 38.

[36] Reynolds, P. J.; Ceperley, D. M.; Alder, B. J.; Lester, W. A. *J. Chem. Phys.* 1982 *77*, 5593–5603.

[37] Halonen, L.; Child, M. *Mol. Phys.* 1982 *46*, 239–255.

[38] Buch, V. *J. Chem. Phys.* 1992 *97*, 726–729.

[39] McCoy, A. B. *Chem. Phys. Lett.* 2000 *321*, 71–77.

[40] Petit, A. S.; Ford, J. E.; McCoy, A. B. *J. Phys. Chem. A* 2014 *118*, 7206–7220.

[41] McCoy, A. B. Diffusion Monte Carlo Approaches for Studying Systems that Undergo Large Amplitude Vibrational Motions. In *Recent Advances in Quantum Monte Carlo Methods*, Vol. 3; Anderson, J. B.; Rothstein, S. M., Eds.; ACS Symposium Series 953: , 2006.

[42] Duncan, M. A. *J. Phys. Chem. A* 2012 *116*, 11477–11491.

[43] Klopper, W.; Kutzelnigg, W. *J. Phys. Chem.* 1990 *94*, 5625–5630.

[44] White, E. T.; Tang, J.; Oka, T. *Science* 1999 *284*, 135–137.

[45] Asvany, O.; Yamada, K. M. T.; Brünken, S.; Potapov, A.; Schlemmer, S. *Science* 2015 *347*, 1346–1349.

[46] Sharma, A. R.; Wu, J.; Braams, B. J.; Carter, S.; Schneider, R.; Shepler, B.; Bowman, J. M. *J. Chem. Phys.* 2006 *125*, 224306.

[47] Li, J.; Pacheco, A. B.; Raghavachari, K.; Iyengar, S. S. *Phys. Chem. Chem. Phys.* 2016 *18*, 29395–29411.

[48] Vorachek, J. H.; Meisels, G. G.; Geanangel, R. A.; Emmel, R. H. *J. Am. Chem. Soc.* 1973 *95*, 4078–4080.

[49] Sager, L. M.; Iyengar, S. S. *Phys. Chem. Chem. Phys.* 2017 *19*, 27801–27816.

[50] Lu, F.; Cheng, L.; DiRisio, R. J.; Finney, J. M.; Boyer, M. A.; Moonkaen, P.; Sun, J.; Lee, S. J.; Deustua, J. E.; Miller III, T. F.; McCoy, A. B. *J. Phys. Chem. A* 2022 *126*, 4013–4024.

[51] McCunn, L. R.; Roscioli, J. R.; Johnson, M. A.; McCoy, A. B. *J. Phys. Chem. B* 2008 *112*, 321–327.

[52] Guasco, T. L.; Johnson, M. A.; McCoy, A. B. *J. Phys. Chem. A* 2011 *115*, 5847–5858.

[53] McCoy, A. B.; Dzugan, L. C.; DiRisio, R. J.; Madison, L. R. *Faraday Discuss.* 2018 *212*, 443–466.

[54] DiRisio, R. J.; Finney, J. M.; McCoy, A. B. *WIREs Comput. Mol. Sci.* 2022 *12*, e1615.

[55] Sandler, P.; Buch, V.; Sadlej, J. *J. Chem. Phys.* 1996 *105*, 10387–10397.

[56] Lee, H.-S.; McCoy, A. B. *J. Chem. Phys.* 2002 *116*, 9677–9689.

[57] Hammer, N. I.; Diken, E. G.; Roscioli, J. R.; Johnson, M. A.; Myshakin, E. M.; Jordan, K. D.; McCoy, A. B.; Huang, X.; Bowman, J. M.; Carter, S. *J. Chem. Phys.* 2005 *122*, 244301.

[58] McCoy, A. B.; Diken, E. G.; Johnson, M. A. *J. Phys. Chem. A* 2009 *113*, 7346–7352.

[59] Lin, Z.; McCoy, A. B. *J. Phys. Chem. A* 2013 *117*, 11725–11736.

[60] Petit, A. S.; McCoy, A. B. *J. Phys. Chem. A* 2013 *117*, 7009–7018.

[61] Eckart, C. *Phys. Rev.* 1935 *47*, 552–558.

[62] Lee, H.-S.; Herbert, J. M.; McCoy, A. B. *J. Chem. Phys.* 1999 *111*, 9203–9212.

[63] Diken, E. G.; Headrick, J. M.; Roscioli, J. R.; Bopp, J. C.; Johnson, M. A.; McCoy, A. B.; Huang, X.; Carter, S.; Bowman, J. M. *J. Phys. Chem. A* 2005 *109*, 571–575.

[64] Price, E. A.; Robertson, W. H.; Diken, E. G.; Weddle, G. H.; Johnson, M. A. *Chem. Phys. Lett.* 2002 *366*, 412–416.

[65] Williams, J. E.; Buss, V.; Allen, L. C. *J. Am. Chem. Soc.* 1971 *93*, 6867–6873.

[66] Wilson, E. B.; Decius, J. C.; Cross, P. C. *Molecular Vibrations;* Dover: New York, 1955.

[67] Scott, A. P.; Radom, L. *J. Chem. Phys.* 1996 *100*, 16502–16513.

[68] Willetts, A.; Handy, N. C.; Green, W. H.; Jayatilaka, D. *J. Phys. Chem.* 1990 *94*, 5608–5616.

[69] Bowman, J. M.; Carter, S.; Huang, X. *Int. Rev. Phys. Chem.* 2003 *22*, 533–549.

[70] Christoffel, K.; Jin, Z.; Braams, B.; Bowman, J. *J. Phys. Chem. A* 2007 *111*, 6658–6664.

[71] Bowman, J. M.; Carrington, T.; Meyer, H. D. *Mol. Phys.* 2008 *106*, 2145–2182.

[72] Roy, T. K.; Gerber, R. B. *Phys. Chem. Chem. Phys.* 2013 *15*, 9468–9492.

[73] Umrigar, C. J.; Nightingale, M. P.; Runge, K. J. *J. Chem. Phys.* 1993 *99*, 2865–2890.

[74] B. L. Hammond, W. A. Lester, J.; Reynolds, P. J., Eds.; *Monte Carlo Methods in Ab Initio Quantum Chemistry;* volume 1 of *World Scientific Lecture and Course Notes in Chemistry* World Scientific Publishing Co.: Singapore, 1994.

[75] Austin, B. M.; Zubarev, D. Y.; Lester, William A., J. *Chem. Rev.* 2012 *112*, 263–288.

[76] Boyer, M. A.; Marsalek, O.; Heindel, J. P.; Markland, T. E.; McCoy, A. B.; Xantheas, S. S. *J. Phys. Chem. Lett.* 2019 *10*, 918–924.

[77] Finney, J. M.; McCoy, A. B. *J. Phys. Chem. A* 2024 *128*, 868–879.

[78] DiRisio, R. J.; Finney, J. M.; Dzugan, L. C.; Madison, L. R.; McCoy, A. B. *J. Phys. Chem. A* 2021 *125*, 7185–7197.

[79] McCoy, A. B.; Huang, X.; Carter, S.; Bowman, J. M. *J. Chem. Phys.* 2005 *123*, 064317.

[80] Lee, V. G. M.; Madison, L. R.; McCoy, A. B. *J. Phys. Chem. A* 2019 *123*, 4370–4378.

[81] Lee, V. G. M.; McCoy, A. B. *J. Phys. Chem. A* 2019 *123*, 8063–8070.

[82] Lee, V. G. M.; Vetterli, N. J.; Boyer, M. A.; McCoy, A. B. *J. Phys. Chem. A* 2020 *124*, 6903–6912.

[83] Finney, J. M.; Choi, T. H.; Huchmala, R. M.; Heindel, J. P.; Xantheas, S. S.; Jordan, K. D.; McCoy, A. B. *J. Phys. Chem. Lett.* 2023 *14*, 4666–4672.

[84] Barnett, R. N.; Reynolds, P. J.; Lester, W. A. *J. Chem. Phys.* 1992 *96*, 2141–2154.

[85] Partridge, H.; Schwenke, D. W. *J. Chem. Phys.* 1997 *106*, 4618–4639.

[86] Schwenke, D. W.; Partridge, H. *J. Chem. Phys.* 2000 *113*, 6592–6597.

[87] Huang, X. C.; Braams, B. J.; Carter, S.; Bowman, J. M. *J. Am. Chem. Soc.* 2004 *126*, 5042–5043.

[88] Huang, X.; Braams, B. J.; Bowman, J. M. *J. Chem. Phys.* 2005 *122*, 044308.

[89] Yang, Y.; Kühn, O. *Z. Phys. Chem.* 2008 *222*, 1375 – 1387.

[90] Peláez, D.; Meyer, H.-D. *Chem. Phys.* 2017 *482*, 100–105.

[91] Yu, H.-G. *J. Chem. Phys.* 2006 *125*, 204306.

[92] Vendrell, O.; Gatti, F.; Lauvergnat, D.; Meyer, H.-D. *J. Chem. Phys.* 2007 *127*, 184302.

[93] Vendrell, O.; Gatti, F.; Meyer, H.-D. *J. Chem. Phys.* 2007 *127*, 184303.

[94] Diken, E. G.; Headrick, J. M.; Roscioli, J. R.; Bopp, J. C.; Johnson, M. A.; McCoy, A. B. *J. Phys. Chem. A* 2005 *109*, 1487–1490.

[95] Johnson, C. J.; Wolk, A. B.; Fournier, J. A.; Sullivan, E. N.; Weddle, G. H.; Johnson, M. A. *J. Chem. Phys.* 2014 *140*, 221101.

[96] Huang, X.; Cho, H. M.; Carter, S.; Ojamäe, L.; Bowman, J. M.; Singer, S. J. *J. Phys. Chem. A* 2003 *107*, 7142–7151.

[97] Halonen, L.; Carrington, T. *J. Chem. Phys.* 1988 *88*, 4171–4185.

[98] DiRisio, R. J.; Lu, F.; McCoy, A. B. *J. Phys. Chem. A* 2021 *125*, 5849–5859.

[99] Robertson, W. H.; Diken, E. G.; Price, E. A.; Shin, J. W.; Johnson, M. A. *Science* 2003 *299*, 1367–1372.

[100] Colbert, D. T.; Miller, W. H. *J. Chem. Phys.* 1992 *96*, 1982–1991.

[101] Gardenier, G. H.; Johnson, M. A.; McCoy, A. B. *J. Phys. Chem. A* 2009 *113*, 4772–4779.

[102] McCoy, A. B.; Huang, X.; Carter, S.; Landeweer, M. Y.; Bowman, J. M. *J. Chem. Phys.* 2005 *122*, 061101.

[103] McCoy, A. B. *J. Phys. Chem. B* 2014 *118*, 8286–8294.

[104] Roscioli, J. R.; Diken, E. G.; Johnson, M. A.; Horvath, S.; McCoy, A. B. *J. Phys. Chem. A* 2006 *110*, 4943–4952.

[105] Rheinecker, J.; Bowman, J. M. *J. Chem. Phys.* 2006 *125*, 133206.

[106] Wang, X. G.; Carrington Jr., T. *J. Chem. Phys.* 2008 *129*, 234102.

[107] Kjaersgaard, A.; Vogt, E.; Hansen, A. S.; Kjaergaard, H. G. *J. Phys. Chem. A* 2020 *124*, 7113–7122.

[108] Vogt, E.; Bertran Valls, P.; Kjaergaard, H. G. *J. Phys. Chem. A* 2020 *124*, 932–942.

[109] Liu, Y.; Li, J.; Felker, P. M.; Bacic, Z. *Phys. Chem. Chem. Phys.* 2021 *23*, 7101–7114.

[110] Metropolis, N.; Ulam, S. *J. Am. Stat. Assoc.* 1949 *44*, 334–341.

[111] Benoit, D. M.; Clary, D. C. *J. Chem. Phys.* 2000 *113*, 5193–5202.

[112] Jacobson, G. M.; Cheng, L.; Bhethanabotla, V. C.; Sun, J.; McCoy, A. B. *J. Phys. Chem. A* 2025 *129*, 2958–2972.

[113] Moonkaen, P.; McCoy, A. B. *J. Phys. Chem. A* 2025 *129*, 2705–2717.

[114] Frederick, J. H.; Woywod, C. *J. Chem. Phys.* 1999 *111*, 7255–7271.

[115] Schreiner, P. R.; Kim, S. J.; Schaefer, III, H. F.; Schleyer, P. v. R. M. *J. Chem. Phys.* 1993 *99*, 3716–3720.

[116] Müller, H.; Kutzelnigg, W.; Noga, J.; Klopper, W. *J. Chem. Phys.* 1997 *106*, 1863–1869.

[117] Olah, G. A.; Rasul, G. *Acc. Chem. Res.* 1997 *30*, 245–250.

[118] Roberts, H.; Herbst, E.; Millar, T. J. *Mon. Not. R. Astron. Soc.* 2002 *336*, 283–290.

[119] Herbst, E. *J. Phys. Chem. A* 2005 *109*, 4017–4029.

[120] Brown, A.; Braams, B. J.; Christoffel, K.; Jin, Z.; Bowman, J. M. *J. Chem. Phys.* 2003 *119*, 8790–8793.

[121] Schmiedt, H.; Jensen, P.; Schlemmer, S. *J. Chem. Phys.* 2016 *145*, 074301.

[122] Schmiedt, H.; Jensen, P.; Schlemmer, S. *Chem. Phys. Lett.* 2017 *672*, 34 – 46.

[123] Wang, X.-G.; Carrington, T. *J. Chem. Phys.* 2016 *144*, 204304.

[124] Boo, D. W.; Lee, Y. T. *J. Chem. Phys.* 1995 *103*, 520–30.

[125] Boo, D. W.; Liu, Z. F.; Suits, A. G.; Tse, J. S.; Lee, Y. T. *Science* 1995 *269*, 57–59.

[126] Huang, X.; Johnson, L. M.; Bowman, J. M.; McCoy, A. B. *J. Am. Chem. Soc.* 2006 *128*, 3478–3479.

[127] Davies, J. A.; Yang, S.; Ellis, A. M. *Phys. Chem. Chem. Phys.* 2021 *23*, 27449–27459.

[128] Kuchenbecker, D.; Uhl, F.; Forbert, H.; Jansen, G.; Marx, D. *Phys. Chem. Chem. Phys.* 2017 *19*, 8307–8321.

[129] Uhl, F.; Marx, D. *Angew. Chem. Int. Ed* 2018 *57*, 14792–14795.

[130] Child, M. S.; Lawton, R. T. *Faraday Discuss. Chem. Soc.* 1981 *71*, 273–285.

[131] Wolke, C. T.; DeBlase, A. F.; Leavitt, C. M.; McCoy, A. B.; Johnson, M. A. *J. Phys. Chem. A* 2015 *119*, 13018–13024.

[132] Johnson, C. J.; Dzugan, L. C.; Wolk, A. B.; Leavitt, C. M.; Fournier, J. A.; McCoy, A. B.; Johnson, M. A. *J. Phys. Chem. A* 2014 *118*, 7590–7597.

[133] Hinkle, C. E.; McCoy, A. B. *J. Phys. Chem. A* 2008 *112*, 2058–2064.

[134] Fore, M. E.; McCoy, A. B. *J. Phys. Chem. A* 2019 *123*, 4623–4631.

[135] Nauta, K.; Miller, R. E. *J. Chem. Phys.* 2000 *113*, 10158–10168.

[136] Skvortsov, D.; Sliter, R.; Choi, M. Y.; Vilesov, A. F. *J. Chem. Phys.* 2008 *128*, 094308.

[137] Raston, P. L.; Liang, T.; Douberly, G. E. *J. Chem. Phys.* 2013 *138*, 174302.

[138] Johnson, L. M.; McCoy, A. B. *J. Phys. Chem. A* 2006 *110*, 8213–8220.

[139] Witt, A.; Ivanov, S. D.; Marx, D. *Phys. Rev. Lett.* 2013 *110*, 083003.